Determining the Effects of Cooling Rate on Magma Crystallisation Using a High Temperature Heating Stage

GEIFMAN, ESHBAL

Determining the Effects of Cooling Rate on Magma Crystallisation Using a High Temperature Heating Stage

Eshbal Geifman

Masters by Research in Volcanology
Durham University Department of Earth Sciences
2022

Supervised By:
Dr Madeleine Humphreys
Dr Fabian Wadsworth
Dr Ed Llewellin

Abstract

In order to understand igneous rock textures and the history of erupted products and the dynamics of lava flow emplacement, it is necessary to understand how crystals grow and what effects different cooling histories have on their growth. Previous studies on crystal growth have often assumed constant crystal growth rates and focused on crystallisation over long timescales more appropriate to igneous intrusions. This work aims to quantify and describe crystal growth rates, morphological variations and textural development of crystals growing from natural lava flow samples, primarily focussing on plagioclase feldspar. High Temperature Heating Stage experiments were carried out at temperatures and cooling rates appropriate to basaltic lava flows, in which wafers of the glassy rind from Blue Glassy Pahoehoe were melted and re-crystallised. It was possible to directly observe and record crystal growth over time at controlled cooling rates, and to extract information from the quenched products. The experiments in this study grew crystals at very low undercoolings, maintaining an interface controlled growth regime and facetted crystal morphologies. Bulk mean plagioclase growth rates of $2.5x10^{-6}$ – $3.2x10^{-5}$ mm/s were found, whilst measured time evolution of crystal growth indicated that growth rates were not constant over time, decaying as they grew. The morphology and aspect ratio of these crystals changed over time, with aspect ratio increasing as growth was significantly faster in the length direction during the observed period. The relationship between mean aspect ratio and crystallisation time proposed by Holness (2014) was experimentally verified. We also observed the 'true' crystallisation time of crystals, highlighting a need for better constraint on how crystal growth times are used to calculate growth rates. The results of this study will contribute to better future interpretations of magmatic histories and crystallisation conditions in natural basaltic lava flows, as well as refinement of Crystal Size Distribution studies. .

Table of Contents

Tables:

Figures:

Acknowledgements

Huge thanks to Madeleine Humphreys, as well as Fabian Wadsworth and Ed Llewellin for their unparalleled support through this project, for keeping me motivated and sharing their wealth of knowledge. A thank you also to Madeleine for letting me take on these exciting experiments and trusting me with the heating stage, and to all the staff working in the labs during this pandemic, who allowed this work to continue even through lockdown, and who were always there to help when I got stuck (or occasionally lost). And thanks to the other postgraduates in the department, who helped me get to grips with postgraduate life and made the last year fantastic.

I would also like to thank my friends and family who have been listening to me rant about volcanoes for the last 10 years, and who have supported me throughout.

1. Introduction

When lava is erupted and flows down the flanks of a volcano, the behaviour of that lava flow is in part controlled by the nature, proportion and distribution of the crystals growing within it (Chevrel et al., 2013; Mader et al., 2013; Cashman and Blundy, 2000). As the molten rock cools, the growing crystals are affected by the conditions they are in, such as surrounding melt chemistry and cooling rate (Loomis, 1982; Kirkpatrick, 1975). In the interpretation of natural igneous rocks cooled from lavas and magma (i.e. cooled at the surface vs sub-surface), the size and morphology of crystals, as well as crystal fraction and textures, can reveal major details about the cooling history of the rock; this in turn can be interpreted to reveal the properties of the magma and the larger processes that affected it at shallow depths within the Earth (Muncill and Lasaga, 1987; Cashman, 1993). Crystal growth from magma has a direct effect on the evolving chemistry of the magma, formation of crystal mushes and crystal settling, and potential for magmatic convection (Marsh, 1988; Langmuir 1989). All of these have a direct effect on the rheology of the magma and therefore its behaviour during storage, transport and eruption (Marsh, 1981). If the effects of, and relationships with temperatures and cooling rates on crystals are properly quantified, it becomes possible to work backwards from eruptive products to determine their cooling histories and from these, understand the past eruptive behaviour of volcanoes. We can also work forwards in modelling rheological controls on magma transport. It is important to understand these behaviours for hazard mitigation and planning, as well as for a general better scientific understanding of volcanoes.

Since crystal growth is a very important factor in understanding and interpreting volcanic rocks, the subject has been previously studied extensively. Studies on crystal growth have varied from using ‘natural laboratories’ such as Makaopuhi lava lake (Kirkpatrick 1977, Marsh and Cashman 1988), to experimental procedures used to grow crystals from synthetic melts

(e.g. Pupier, 2008; Watanabe and Kitamura, 1992; Kirkpatrick, 1977). These studies are often carried out over a large range of cooling rates, pressures and undercoolings. Crystals grown in both natural rocks and experimental samples are often characterised using crystal size distribution (CSD) studies. On the basis that crystal sizes and igneous textures are a product of crystal nucleation and growth rates, crystal size studies can be used to work out the timescales of crystallisation, or to calculate nucleation or growth rate, from a dataset of crystal sizes (Cashman, 1993). A variety of assumptions about crystal growth rates are often made in these studies, most commonly that growth rate is constant through the whole crystallisation interval (e.g. Blundy and Cashman, 2008; Hammer et al., 1999; Salisbury et al., 2008). However, recent work using calorimetry and textural analysis to define crystallisation has shown some evidence that these assumptions are likely not accurate (Applegarth et al., 2013b).

With the aim to better refine our interpretation of igneous rocks, a relationship was proposed in Holness (2014) between the 2D crystal aspect ratio of plagioclase, and the cooling time of magma, where cooling time is used in place of the cooling rate. This relationship is intriguing, since it may provide an efficient way to interpret the cooling time/rates of igneous products from the crystal aspect ratio alone. The crystals measurements used in Holness (2014) came from dolerites in intrusive igneous features cooled over long time periods (months – years). This relationship has not previously been tested for shorter timescales and faster cooling rates. In this study, I aim to:

1. Quantify and describe the effects of changing cooling rate on the growth of crystals from a basaltic melt, at a low undercooling, as relevant to ~10cm depth within a Pahoehoe lava flow and to allow for the formation of tabular crystals.
2. Test the assumption of the constancy of crystal growth rates, and to observe and measure the real-time evolution of crystal growth from melt.

3. Experimentally test and validate the relationship between aspect ratio and crystallisation time proposed in Holness (2014).

In order to achieve this, high temperature heating stage experiments were carried out using polished wafer samples of Blue Glassy Pahoehoe (BGP) basalt from Kilauea, which has a highly glassy rind suitable for experiments of this nature due to its lack of pre-existing crystals and low-viscosity melt properties. The experimental set up allowed crystallisation to be directly observed through a window in the heating stage via an optical microscope, allowing for the possibility of recording crystal growth in real-time. The temperatures and cooling rates were programmed and controlled via computer, and conditions used were reflective of modelled and measured conditions a few centimetres depth into a lava flow from the upper surface. Following the experiments, crystal size data was further collected from the quenched sample via SEM and optical microscope imaging.

This thesis outlines the previous work and background on this topic, before detailing the methodology and pre-experimental modelling done on crystal growth and cooling rates of lava flows. Following this is an in-depth characterisation of the starting material, BGP. The experimental results are then presented, with an in-depth review of each experimental output and overall results of aspect ratio, crystal shape and growth rates. These results are then interpreted and discussed in relation to previous work and current knowledge about crystal growth. The implications of these results are then explored, and the effects of these findings on future CSD studies are discussed. The main conclusions from this work are laid out in the final chapter.

2. Background

2.1 The Importance of Understanding Crystal Growth

The rheology of lava and magma is an important input into many models of volcanic eruptions, and gaining a better understanding of its evolution before and during eruption can aid future predictions on eruptive behaviour and interpretations of eruptive products. More accurate predictions will allow for improvements in hazard management and our understanding of volcanoes.

The growth of crystals has a direct and important impact on the rheology of lava. The rheology of lava is controlled primarily by its viscosity and its yield strength. Bulk rheology is controlled by several attributes of the lava including crystallinity and bubble content, while temperature and chemistry of the melt change the viscosity (Chevrel et al., 2013). Crystal growth during eruption is strongly linked to the flow rates and internal pressures in a lava flow, and thus affects the rheology of magma during eruption, which in turn has an effect on the style of eruption (Mader et al., 2013; Cashman and Blundy, 2000). Crystal growth also has an effect on the evolution of the chemistry of the melt, which is another control on lava rheology (Giordano et al., 2008).

The combination of the internal lava rheology and the cooling surface crust are key to determining the morphology of a lava flow, and the interaction and comparative yield strengths of the crust and core of a lava flow produces a variety of surface morphologies, cooling regimes and modes of flow advance (Lyman et al., 2005; Kilburn, 1993). The changing viscosity of a lava flow affects the potential to transition from pahoehoe to a'a lava, where viscosity (as well as rate of shear strain) plays an important part in controlling whether or not lava makes the transition before flow cools and stops (Peterson and Tilling, 1980). The formation of crusts on lava flows creates an insulating effect on the flowing lava, increasing its mobility. The

emplacement of a lava flow is primarily controlled by the evolution of its temperature over time, which has a strong influence on crystallisation, as well as degassing and vesiculation. These factors control the bulk viscosity of the lava flow and determine its surface morphology (Gottsmann et al., 2004)

The shape of crystals is an important control on lava rheology. Suspensions of equant crystals will have a lower viscosity than those with elongated shapes, for a given crystal fraction (Mueller et al, 2011). Crystals with a higher aspect ratio (length/width) have a greater impact on the viscosity of lava since they interact with each other more readily as they grow, so the maximum crystal fraction that can be held in suspension before crystals start jamming and thickening the melt is lower for elongated particles (Figure 1). Conversely, smaller aspect ratios result in more effective crystal packing (Liu et al., 2017). The yield strength of the particles within lava exists if the particles are in a framework in which they are in contact with each other. Particles with higher aspect ratios (i.e 10:1 or higher), particularly rod-shaped crystals such as those formed by feldspars, will experience interaction at lower crystal contents. Once subject to shearing, there is a high probability that the particles will be in contact, forming a bridging framework by only 20% concentration of crystals (Pinkerton and Stevenson, 1992). Elongate crystals therefore require a lower packing density and therefore reach a rheological transition at an earlier stage of crystallisation of a lava flow. It is therefore important to understand how the aspect ratios of tabular crystals such as plagioclase are controlled, as well as how the crystal volume fraction may develop in a cooling lava.

Crystal growth and the controls on growth rates, morphology and their interactions within a cooling lava flow are important factors to investigate in order to contribute to existing and future models, and add to our overall understanding of the behaviour of lava flows.

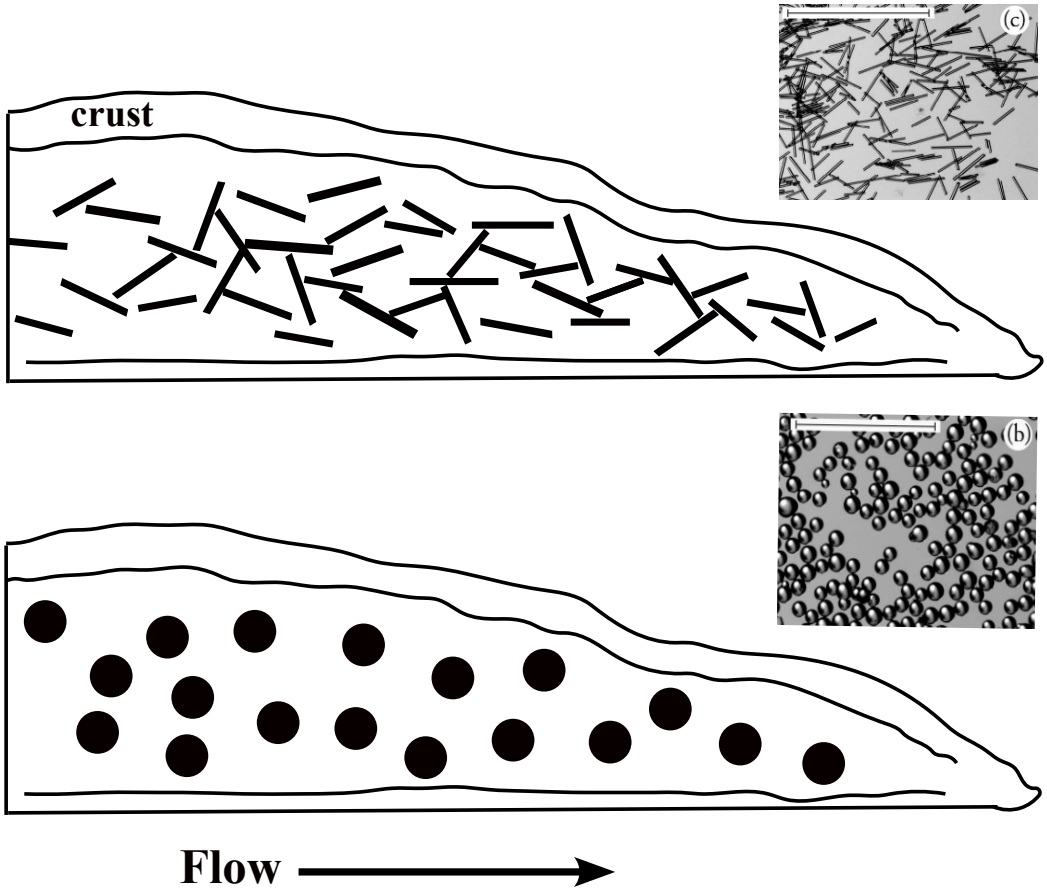

Figure 1. Comparing textures used in Mueller et al. (2011). For similar particle fractions, it can be seen that the elongated tabular crystals are more likely to jam together than the spherical beads. Yield strength within the lava flow with higher aspect ratio crystals will therefore be significantly higher, for similar crystallinities.

2.2 Crystal Growth

2.2.1 Undercooling

Undercooling a liquid involves the lowering of the temperature of a liquid below its liquidus temperature/ freezing point, without it becoming a solid. For melts, this can be achieved experimentally through cooling (Kirkpatrick, 1975), or through decompression (which increases the liquidus temperature via melt dehydration; Mollard et al., 2012), or through degassing alone. The degree of undercooling can be measured as the difference between the liquidus and the melt temperature. Undercooling can be thermal, or constitutional, where the

compositional changes modify the liquidus temperature. The undercooling is dependent on the chemical composition of the remaining melt, and as crystals start to nucleate and grow out of the melt, this composition evolves, changing with it the effective undercooling for a given temperature. Volatile concentration within the melt can also increase as volatile-free phases crystallise. Evolution of melt as crystallisation occurs at slow cooling rates allows us to find experimental conditions in which a slow cooling rate maintains a low undercooling and therefore an interface controlled growth regime. This effect is described fully in Figure 2 (adapted from Loomis, 1981).

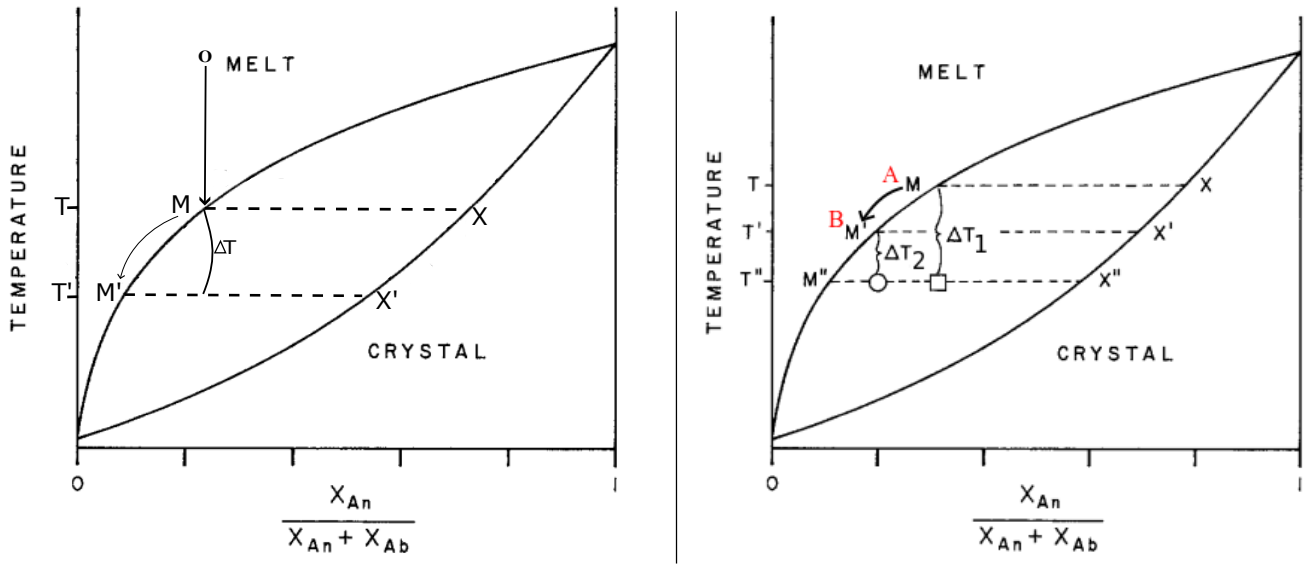

Figure 2. Adapted from Loomis (1981). Two diagrams illustrating undercooling. The X-axis represents the anorthite content in the melt/crystal compositions. For a cooling melt, upon reaching the liquidus temperature, T, represented by the upper curved line, the melt composition is M, and the first crystals to grow have composition X. If temperature is then dropped to T', the melt will experience an undercooling of ΔT.

In the diagram on the right: A) As the melt starts to crystallise, the melt composition evolves towards M', and crystal composition moves from X to X'. B) If a sample is quenched when the composition is at M', the texture would represent an effective undercooling of ΔT_2, since the liquidus has decreased.

2.2.2 Degassing Induced Crystallisation

Crystallisation from melt is not driven only by cooling. Exsolution of volatiles from a melt can trigger crystallisation by increasing the magma liquidus temperature (Applegarth et al., 2013a). Loss of volatiles (usually H_2O) from a melt causes the liquidus to increase, thereby increasing the undercooling (with respect to the anhydrous liquidus) (Sparks et al, 1978; Carmichael et al, 1974). This occurs because water molecules in solution depolymerise the melt, which disrupts crystal formation (Kohn, 2000). In nature, volatile loss is often caused by decompression during magma ascent.

Applegarth et al. (2013b) have demonstrated, using thermogravimetric analysis data and differential scanning calorimetry, that the heating and subsequent degassing of basaltic lava containing 0.39-0.81wt% volatiles resulted in an exothermic event that can be interpreted as crystallisation. Re-heating the de-gassed basalt did not result in any further crystallisation, indicating that the crystallisation that had occurred was driven by the loss of volatiles. These experiments show that significant crystallisation can occur as a result of degassing, even in basalts with low volatile contents (Applegarth et al., 2013b).

2.2.3 Nucleation

To nucleate a crystal , a driving force, i.e undercooling, must be applied in order to drive the melt out of equilibrium, and nucleate a new solid crystal. Once this driving force has been applied (often a decrease in temperature, or a chemical change), small clusters of atoms that are smaller than a critical size will cluster together until they form an object that is larger than a critical nucleus size, which can then begin growing as a crystal (Sunagawa, 2007). The critical nucleus size is reached when the volume of atoms or molecules in a cluster grows large enough to overcome a critical energy barrier (Gaides, 2017). Nucleation can occur either heterogeneously or homogenously. For homogenous growth to occur, the energy barrier and therefore the cirtical size of a nucleus is relatively large. In heterogeneous growth, the crystal begins to grow on top of an existing surface, such as the surface of another crystal or bubble. This means that less energy is required for new growth, and nucleation can occur at lower undercoolings than are required for homogenous growth (Pupier et al., 2008). In homogeneous growth, crystals appear to grow directly from the melt. In most natural systems, nucleation will begin due to heterogeneities, but in some cases where the driving force is high enough, crystals can grow spontaneously from a melt or solution.

2.2.4 Diffusion limited vs Interface Controlled Growth

There are two regimes in which crystals grow, and which of these occurs is dependent on factors such as the undercooling, chemistry and viscosity of the melt and crystals. Diffusion limited growth occurs when the continuation of growth of the crystal is limited by the speed at which atoms can diffuse through the liquid and into the depleted region around the crystal; therefore, the speed at which the crystal grows is limited by the speed that atoms can move through the liquid. This means that melt chemistry, and consequently diffusivity and viscosity, have a strong effect on the crystal growth rates. Interface controlled growth occurs when the

rate of crystal growth is controlled by the transport of materials across the crystal-liquid interface and is independent of the speed that atoms can move through the melt (Brandeis and Jaupart, 1987; Kirkpatrick, 1975). Diffusion limited growth often results in a cellular, less equilibrated morphology in crystals, whilst interface controlled growth leads to a facetted morphology (Kirkpatrick, 1975). Interface controlled growth is more likely to occur in lower degrees of undercooling and therefore is probably the rate-controlling process in the growth of most plutonic and some volcanic igneous rocks (Kirkpatrick, 1975).

One of the key controls on crystal morphology and growth rate is undercooling, where higher undercoolings can lead to a switch from interface controlled growth to diffusion limited growth regimes. Figure 3 below shows some of the different plagioclase crystal shapes that may grow during the experiments carried out in this study, moving from an interface-controlled regime growth (tabular) towards some diffusion-limited growth (skeletal) morphologies (based on previous studies such as Lofgren (1974) and Shea and Hammer (2013)).

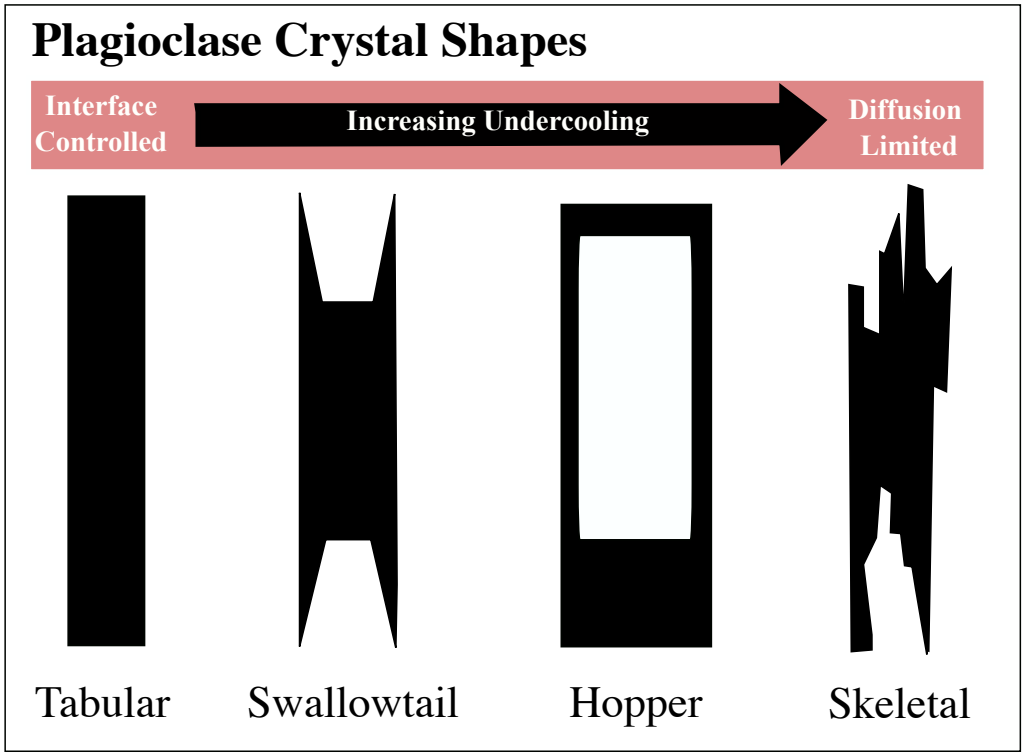

Figure 3. Silhouettes of different plagioclase crystal shapes, moving from interface controlled regime growth on the left, towards more diffusion limited growth on the right.

Lofgren (1974), found that the morphologies of plagioclase change systematically with undercooling. High undercoolings resulted in increasingly irregular morphologies such skeletal and spherulitic crystal growth, whilst small undercoolings resulted in tabular morphologies. With increasing undercooling, the distance, or wavelength, between instabilities in the crystal starts to decrease, leading first to skeletal and then to more dendritic and eventually spherulitic morphologies as undercooling increases and the growth regime shifts to being diffusion limited (Kirkpatrick, 1975).

However, these previous experimental studies were conducted over a large range of undercoolings, and the effects of smaller variations of temperature and cooling rate within low undercooling regimes are less well constrained.

2.2.5 Crystal Growth on an Atomic Scale

Crystals grow by the addition of atoms or groups of atoms onto their surface. They incorporate these atoms from the melt or solution around them. Atoms or molecules in the melt will arrive on the surface and will either return into the ambient phase or will attach themselves onto steps or kinks already formed on the surface of the crystal, where they can then be incorporated into the crystal structure (Sunagawa, 2009). Reaction-rate theory describes the rate at which atoms or molecules move from the melt to become attached to a crystal surface. According to this theory, if an atom or molecule moves from melt to crystal it must first leave its energy state in the melt, pass through an activated state, and then drop to the crystal energy state upon attachment (Turnbull and Cohen, 1960; Kirkpatrick, 1975). The growth rate of a crystal is the difference between rates of this molecular detachment from melt and the reattachment to crystals (Kirkpatrick, 1975). Crystal growth is exothermic as chemical bonds are formed as molecules or atoms attach to the crystal surface, meaning that it can be quantified using heat flow signals in calorimetric experiments (e.g. Applegarth, 2013b).

Within interface growth regimes, crystals can grow through lateral growth, where the crystal grows by the shifting of a step across the surface of the crystal. There are two mechanisms by which lateral growth can occur – surface nucleation or screw dislocation (Kirkpatrick, 1975; Calvert and Ulhmann, 1972; Hillig and Turnbull, 1956). Figure 4 below illustrates how molecules may attach themselves onto a step on the crystal surface. The rate at which a crystal grows is controlled by the conditions in which the crystal is growing. Crystal growth rates are strongly linked to cooling rates of the melt, where a faster cooling rate leads to faster growth rates (Cashman, 1993). In a comparison of both natural and experimental data carried out by Cashman (1993), it was found that plagioclase growth rates can be a predictable function of cooling rate. Plagioclase sizes in basalt may therefore be used to work backwards, using knowledge of the relationship between cooling rate and growth rate, in order to obtain a measure of their residence time in magma (Cashman, 1993). This opens up questions and possibilities regarding further honing our understanding of this relationship in order to better interpret cooling histories of volcanic rocks.

Surface, or 2-D, nucleation occurs when a one-molecule thick nucleus outcrops on the surface of a crystal and creates a step onto which more atoms can stick and grow the crystal. The layer then grows laterally, and more layers can start to grow on top of it, growing the crystal layer by layer (Kirkpatrick, 1975; Sunagawa, 2009). For surface nucleation to occur, a higher undercooling is generally required to generate the nucleus (Baronnet, 1984; Holness, 2014). In growth via the screw dislocation mechanism, a screw dislocation emerges at the surface of the crystal, creating a spiral of repeating steps (Kirkpatrick, 1975; Holness, 2014). Similarly to the surface nucleation step mechanism, atoms can only attach themselves to the edges of these layers to grow the crystal (Hillig and Turnbull, 1956). In this case, attachment can be continuous, even at low undercoolings, and can result in facetted crystals (Holness, 2014). For continuous growth to occur, atoms must be able to attach to any part of a rough surface. In this

case, growth can be uniform across the surface, and results in more atomically rough surfaces (Holness, 2014).

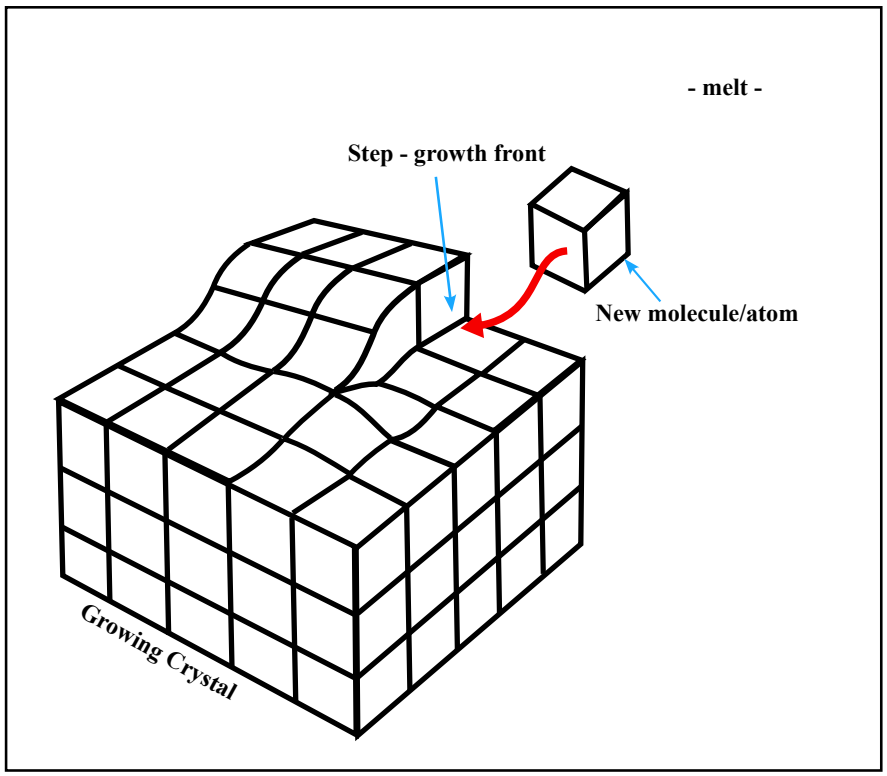

Figure 4. Diagram of a growing crystal where a screw dislocation has created a step onto which new atoms or molecules can attach and grow the crystal (adapted from Cormier et al., 2022)

2.2.5 Controls on Crystal Growth Rates

The Avrami equation (Equation 1), and relationships described in Avrami (1939, 1940, 1941), can be used to define the relationship between crystal fraction, growth rate, nucleation rate and shape over time. The Avrami equation is often plotted as the change in crystal fraction with time, and produces a sigmoidal curve:

$$\Phi = 1 - exp(-k_v I Y^3 t^4) \quad (1)$$

Where Φ is the crystal fraction, k_v is a volumetric shape factor, I is the nucleation rate, Y is the growth rate, and t is time.

Another variation of this equation can be derived in which I is replaced with N_v (number of crystals/volume) and the exponent of t becomes 3, for situations where nucleation is instantaneous (Cashman, 1993). This formula assumes that crystallisation is occurring from a one component system, that temperature is constant, and that nucleation occurs homogeneously with the nuclei randomly distributed within a space (Cashman, 1993; Zanotto, 1996). The crystals are also generally assumed to be spherical. This formula also does not account for the effects of crystal packing and impingement, creation of small pore spaces between crystals where smaller pore sizes require a higher undercooling for growth to occur within them (Holness et al., 2012), or chemical evolution of the melt within a multi-component system. Despite these assumptions, the Avrami equation can be used to create a foundation of knowledge about the crystallisation kinetics of a system; and if growth rate and nucleation rate are known, they can be used to model the evolving crystallinity of a system over time.

2.2.7 Controls on Crystal Morphology

The shape formed by a growing crystal is controlled by the rate at which its different faces grow. The smallest face on a plagioclase crystal is perpendicular to the fastest growth direction, whilst the larger faces are slower growing (Holness, 2014). This means that crystals will propagate in the direction of their longest axis more quickly than they will widen their shorter axes. For a facetted plagioclase crystal, growth is fastest along the x-axis (100), whilst growth is slowest along the y-axis (010) (Muncill and Lasaga, 1988) (Figure 5). Findings from natural rocks indicate that the different faces of plagioclase crystals appear to respond differently to changes in cooling rate, with the (001) face being less sensitive to cooling rate than the (100) face, and the (010) face having an intermediate response (Holness, 2014). This is possibly caused by differences in the structure and chemistry of the crystal surfaces (Baronnet, 1984; Holness, 2014). The ratio of growth rates of each crystal axis determines their final shapes. Cashman (1993) also found that crystal sizes decrease with decreasing cooling rate, and that crystals grown at slow cooling rates are more likely to have euhedral morphologies. Increasing undercooling and cooling rate appears to cause an increase in the difference between the growth rates along the x and y axes, creating more elongated crystal shapes (Muncil and Lasaga, 1987; Pupier et al., 2008).

Figure 2 Diagram of crystal faces

This is consistent with Holness (2014), who found that crystal aspect ratio has a strong negatively correlating relationship with the total crystallisation time (Equation 2), which may also serve as an indicator of the cooling rate of that magma. This is based on findings from a set of compositionally similar natural igneous rocks, using intrusions with a known geometry and with the application of a one-dimensional cooling model to 'calibrate' the crystal-timescale relationship.

$$\log(crystallisation\ time) = -1.79(average\ aspect\ ratio) + 6.34 \quad (2)$$

This relationship was derived from rocks in which total crystallisation time was long (years), and therefore cooling rate was slow. Holness (2014) did not examine how data for shorter cooling times fits into this equation, though it is suggested that this relationship could be applied to crystals with crystallisation times of under a year.

2.3 Crystal Size Distributions

The study of crystal size distributions (CSD) was first developed by Randolph and Larson (1971) in the context of chemical engineering and industrial use, but this theory can be directly applied to a geological context (first shown in Marsh 1988 and Cashman and Marsh (1988)). The basis of this is that the size of crystals is a product of their growth rate and their age. Lavas are quenched during nucleation and growth, and therefore studying crystal sizes can provide information about the crystallisation kinetics in lava (Marsh, 1988). In most cases of natural lava, the population density of crystals within a crystal size interval is an exponentially decreasing function of the representative sizes of that interval. Plotting this in a semi-logarithmic fashion will yield a linear trend with a negative slope (Figure 4). CSD theory can be used with these data to infer quantitative information on crystal growth rates and nucleation. Conversely, if nucleation and growth rates are known, these data can be used to understand how the CSD may evolve over time (Pupier, 2008). Analyses of CSDs are commonly used to

calculate the timescales of crystallisation, and in doing so will assume growth rates which are not yet well constrained, such as those for low undercoolings. Whilst commonly used petrological methods will yield 2D images and measurements of crystal intersections from thin sections, it is important to accurately understand how these crystals are distributed in 3D. From CSD studies has emerged a need for a better understanding of how 3D shapes of real crystals may affect the outcomes of these studies, which generally quantify distributions within a volume. Higgins (2000) developed a stereology-based method and corresponding software (CSDCorrections) in order to better constrain the distribution of crystals, taking into consideration their 3D shape, based on 2D measurements. This software takes crystal size data together with inputs of crystal axis ratio (assuming the same 3D morphology across all crystals) and overall texture to produce a 3D CSD. The methods and software from this study are generally accepted as a good representation of the true 'corrected' 3D CSD (e.g. Brugger and Hammer, 2010; Martin et al., 2006). Building on this work further, Morgan and Jerram (2006) developed a spreadsheet that takes 2D crystal size data and uses it to interpret the 3D crystal habit of the measured phase via comparison with a database of the aspect ratios of 10,000 modelled 'slices' through 703 different crystal habits, although there is an upper limit of 1:10 for the ratio of any two crystal axes. This limit could lead to some inaccuracies in the understanding of the true 3D crystal shape if natural shapes do not fall within these bounds and requires some more refinement. Nevertheless, the implementation of these 3D corrections for use of 2D data has enabled a much more accurate understanding of crystal size distributions. These techniques were employed in this study in order to better understand and interpret 2D length and width datasets.

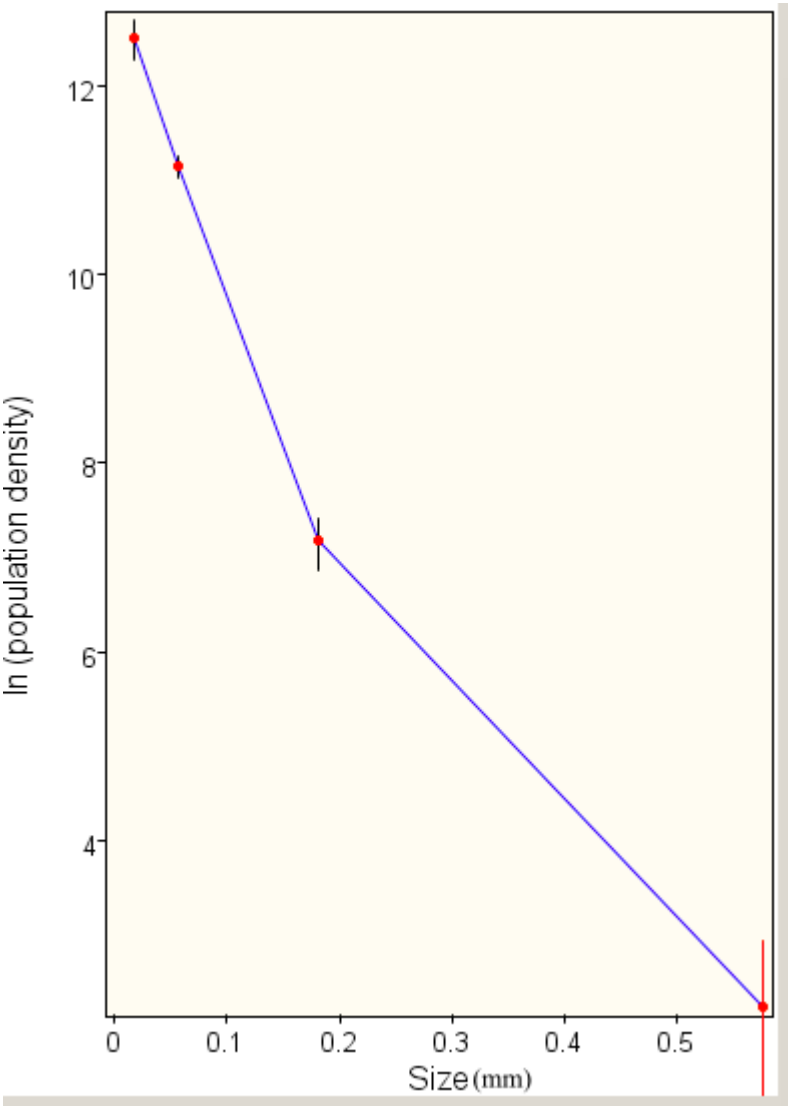

Figure 6. An example of a CSD plot output from CSDCorrections (Higgins, 2000), for plagioclase growth (size in mm) from the data in this study.

2.4 Previous Experimental Studies on Crystal Growth

The growth of plagioclase has been studied extensively over the last few decades, using experimental techniques to supplement natural observations from igneous rocks. Many studies of plagioclase growth, such as Holness (2014), Marsh and Cashman (1988) and Kirkpatrick et al., (1979) have focussed on measurements of naturally grown plagioclase in igneous rocks. Plagioclase lends itself to studies of crystal growth due to its tabular morphology and generally rectangular 2D shape, with an easily definable length and width. Makaopuhi lava lake, a prehistoric tholeiitic lava lake in Hawaii, is used as a natural laboratory used for these studies, since cooling rates and temperatures are well constrained, and growth rates of $1.7 – 11x10^{-12}$ ms^{-1} have been interpreted from drill hole samples, where thermocouple measurements were used to measure temperatures and cooling rates (Kirkpatrick, 1977). Some previous studies have made use of furnaces (e.g. Pupier et al., 2008; Kirkpatrick et al., 1979) and heating stages (e.g Applegarth et al., 2013a; Kirkpatrick et al., 1979) in order to gain information on crystallisation in a more controlled environment. Table 1 below shows a summary of several key experiments previously carried out on plagioclase growth. These have been used to inform the methodology of this investigation.

Study	Temperatures (ºC)	Cooling rate (ºC/min)	Experimental Method	Starting Material	Growth rates (m/s)
Applegarth et al. (2013a)	1190 – 1270	10 – 20, with isothermal hold	Heating stage experiments with an isothermal hold between heating and cooling.	K-trachybasalt from Mt. Etna, and BGP (Kilauea)	$1.7x10^{-9}$ – $1.8x10^{-8}$
Kirkpatrick et al. (1979)	960- 1400 (DT = 150 – 380)	Isothermal	Heating stage for low undercooling, resistance furnace quenching for high undercooling	Synthetic plagioclase from oxide powders	$8x10^{-5}$ – $3x10^{-10}$
Muncill and Lasaga, 1987	900 – 1500	Isothermal after single step drop.	Pt capsule in vertical tube furnace. Charges raised to 30C above liquidus and held for 30 mins, then lowered to a temperature below liquidus in a single step.	Synthetic Plagioclase, made from gels, with seed crystals	10^{-7} – 10^{-9}
Pupier (2008)	1190 – 1110	0.05, 0.02, 0.003	Pt wire loop in furnace	Synthetic powders, basaltic	$1.1x10^{-9}$ - $3.3x10^{-10}$
Schiavi et al., 2009	900	2.5 (heating), then isothermal	Moissanite cell, charge heated and then held at 800C for 12h and then 900C for 8h, then cooled quickly.	Synthetic high-K andesitic glass, FeO replaced with MnO	4.9 – 1.9 $x10^{-9}$
Watanabe and Kitamura (1992)	1070 – 1164	Isothermal	Fe and Pt capsules, heated on Pt wire in vacuum. Rapid temperature drop followed by isothermal hold.	Basaltic glass prepared from oxide powders	0.3 - $21x10^{-8}$

Table 1. Summary of previous experimental studies on plagioclase growth, all carried out at 1 atm.

Past experimental techniques sometimes made use of synthetic powders or gels to create a basaltic lava composition for a starting material that could then be used in experiments (e.g. Muncill and Lasaga, 1987; Pupier et al., 2008; Watanabe and Kitamura, 1992; Kirkpatrick et al., 1979). The advantage of this method is that controlling the composition allows for the creation of a material with the desired characteristics, as well as being easier to homogenise, with no possible effects of pre-existing large crystals or natural heterogeneities. However, in natural scenarios, crystals grow from a natural lava or melt, meaning that perhaps observing growth from natural materials can lead to a more realistic set of measurements and results. Experimental techniques also often make use of furnaces with the samples enclosed in an

opaque vessel (e.g. Muncill and Lasaga, 1989; Pupier et al., 2008). Using this method prevents the ability to make direct observations of the crystals during growth, and the samples must be quenched at different points in order to observe 'snapshots' of growth.

Few studies using a heating stage to directly observe growth have been carried out. Applegarth et al. (2013a) were able to use methods similar to those in this study to record the growth and shape evolution of plagioclase from natural melts in experiments involving crystallisation in response to degassing, however this study was only able to track the growth of 5 plagioclase crystals from a Kilauean basalt melt. Kirkpatrick et al. (1979) and Schiavi et al., (2009) were also able to observe some growth at low undercoolings in their experiments. However, there is a paucity of experiments with direct observations such as these, and there is a knowledge gap for studies involving direct observations of crystal growth from natural material carried out at 1atm, at low undercoolings, allowing for this thesis to fill that gap in experimental technique and to acquire new knowledge on crystal growth. This study builds on previous direct growth observations made in studies such as Applegarth et al. (2013a) by carrying out more in-depth analyses of the evolving crystal morphologies in both 2- and 3-D, and expanding datasets on changing growth rates of plagioclase within a basaltic Kilauean lava. The following chapter will detail how this investigation approached building on past experimental work and the procedure used.

3. Methodology

3.1 Experimental Approach

The principal objective of this study was to observe and measure the growth of crystals growing at low undercoolings. A mix of modelling techniques was implemented in order to (a) identify the temperature conditions that would be best for the heating stage experiments, (b) to predict the relative abundance and composition of each phase as a function of temperature, and (c) to identify reasonable cooling rates as a starting point for the experiments. Objectives (a) and (b) were addressed by modelling growth conditions in RhyoliteMELTS (Gualda et al., 2012; Ghiorso and Gualda, 2015); while (c) was carried out using existing field data, supported by mathematical models, to determine cooling rates and conditions that would be viable in experiments, while remaining valid for natural lava flows.

3.1.1 Starting material

Natural Blue Glassy Pahoehoe (BGP) from Kilauea was used as a starting material in the heating stage experiments since its basaltic composition means that it would create a low-viscosity melt. Blue Glassy Pahoehoe is interpreted to be strongly degassed with very low residual volatile contents, based on its glassy, vesicle-poor nature and lack of fluorine (Oze & Winter 2005; Swanson 1973), and a volatile-poor composition was also demonstrated by the small quantity and quick dissipation of bubbles seen only at the start of each experimental run. Using a nearly anhydrous or low-volatile melt ensured that crystallisation was dominated by cooling, as opposed to degassing. This allowed for diffusion to occur more easily across crystal boundaries than it would in a high viscosity environment, keeping experiments within a reasonable time frame (within the limit of the few hours in which the cooling system remains

efficient). It is naturally glassy with few phenocrysts, so a nearly crystal-free melt could be generated without prolonged heating. Having pre-existing crystals present could result in them exerting an influence on local chemistry and acting as sites of heterogeneous nucleation (as seen in the Etna sample experiments of Applegarth et al., 2013a). Using this material means that results from the experiments could also be directly compared to the natural BGP samples. The BGP itself is characterised in further detail in chapter 4.

3.1.2 RhyoliteMELTS Thermodynamic Modelling

RhyoliteMELTS (Gualda et al., 2012; Ghiorso and Gualda, 2015) was used to predict the liquidus temperature, mineral compositions, phase proportions, and the order and quantity of mineral crystallisation from melt through equilibrium modelling and calculations. The starting composition for MELTS calculations was that measured by Llewellin (personal communication), as the same samples were used in these experiments (presented in detail in Table 9, Chapter 4). An H_2O content of 0 was used.

MELTS simulations were run at a range of oxygen fugacities, from ΔFMQ+3 to ΔFMQ-2 to investigate the effects on liquidus temperature of changing how oxidising the conditions are. The experimental fO_2 is unconstrained – this modelling allowed us to assess liquidus temperature more accurately by comparing the observed phase assemblage with those predicted by MELTS at different fO_2. The heating stage experiments were run in a controlled gas atmosphere (N_2) to try to reduce oxidation. Kilauean basalt has been shown to have a fugacity between the FMQ and NNO buffers (Mucek et al., 2012). The liquidus temperature of the whole system was calculated to be 1179 – 1313 °C for this composition, for different oxygen fugacities (Table 2). All MELTS simulations were started at 1250°C and the temperature was dropped in steps of 5°C for each run, to a final temperature of 900°C. All runs were carried out with the "fractional crystallisation" option active.

fO_2	Minerals (in crystallisation order, with saturation T)	Liquidus T °C	Phase proportions at 1140°C			
			Olivine	Plagioclase	Clinopyroxene	Spinel
FMQ -2	Olivine (1195°C), Plagioclase (1170°C), Clinopyroxene (1165°C)	1195.9	5.5%	13.9%	12.2%	-
FMQ -1	Olivine (1190°C), Plagioclase (1170°C), Clinopyroxene (1165°C)	1191.4	4.6%	14.0%	13.5%	-
FMQ +1	Clinopyroxene (1175°C), Plagioclase (1170°C)	1179.7	-	14.2%	17.3%	-
FMQ +3	Spinel (1210°C), Clinopyroxene (1185°C), Plagioclase (1175°C), Olivine (1165°C), rhm oxides (1115°C)	1312.7	1.3%	11.9%	21.8%	9%

Table 2. Minerals crystallised from BGP composition at different fO2 conditions, as predicted by Rhyolite MELTS (Gualda et al., 2012).

The different minerals predicted to crystallise out of a BGP melt for different fO_2 conditions, as predicted by MELTS, as well as the system liquidus temperature and the phase proportions at 1140°C, which was the lowest experimental quench temperature are described in Table 2. This temperature is still higher than 1123°C, the eruptive temperature of the BGP (Oze and Winter, 2005). Plagioclase was predicted to crystallise out under all tested fO_2 conditions. With increasing fO_2, there is a change from olivine crystallising out first, to clinopyroxene growing first. At high fO_2, there is likely sufficient ferric iron in the liquid to stabilize spinel, allowing it to readily crystallise (Hill and Roeder, 1974). Only the highest ΔFMQ values predicted crystallisation of oxides before 1140°C. The liquidus temperatures change with fO_2 values, increasing as fO_2 increases. Hill and Roeder use experimental results on the equilibrium crystallisation of basaltic melt to show that higher fO2 values can increase the temperature at which phases begin to crystallise, and propose that the temperature at which plagioclase and

clinopyroxene crystallise increases with oxygen fugacity due to early crystallisation of spinel, which increases the contents of Al_2O_3, SiO_2, CaO and Na_2O in the melt.

The evolving mineral and melt compositions predicted from MELTS are shown in Table 3 and 4, which show the compositions of the first and last plagioclase crystals to form within planned experimental conditions, and these will later be compared to EDS compositional data from natural BGP samples, and to the results of experimental runs. Changes in fO_2 conditions did not appear to greatly alter the composition of the first plagioclase crystals, but the final crystals become increasingly less anorthitic at higher fO_2 conditions.

fO_2	SiO_2	Al_2O_3	CaO	Na_2O	K_2O	X_{An}	X_{Ab}
FMQ -2	50.1	32.0	14.7	3.18	0.062	0.72	0.28
FMQ -1	50.1	32.0	14.7	3.18	0.063	0.72	0.28
FMQ +1	50.2	31.9	14.6	3.22	0.068	0.71	0.28
FMQ +3	50.2	31.9	14.6	0.28	0.061	0.71	0.29

Table 3. Composition of first plagioclase feldspar crystals to crystallise out from BGP in MELTS simulations for different fO2 conditions.

fO_2	SiO_2	Al_2O_3	CaO	Na_2O	K_2O	X_{An}	X_{Ab}
FMQ -2	52.2	30.5	13.0	4.12	0.105	0.63	0.36
FMQ -1	52.3	30.5	12.9	4.16	0.109	0.63	0.37
FMQ +1	52.5	30.4	12.8	4.23	0.122	0.62	0.37
FMQ +3	53.0	30.0	12.4	4.50	0.095	0.60	0.39

Table 4. Composition of plagioclase feldspar crystals which crystallise out at 1140ºC from BGP in MELTS simulations for different fO2 conditions.

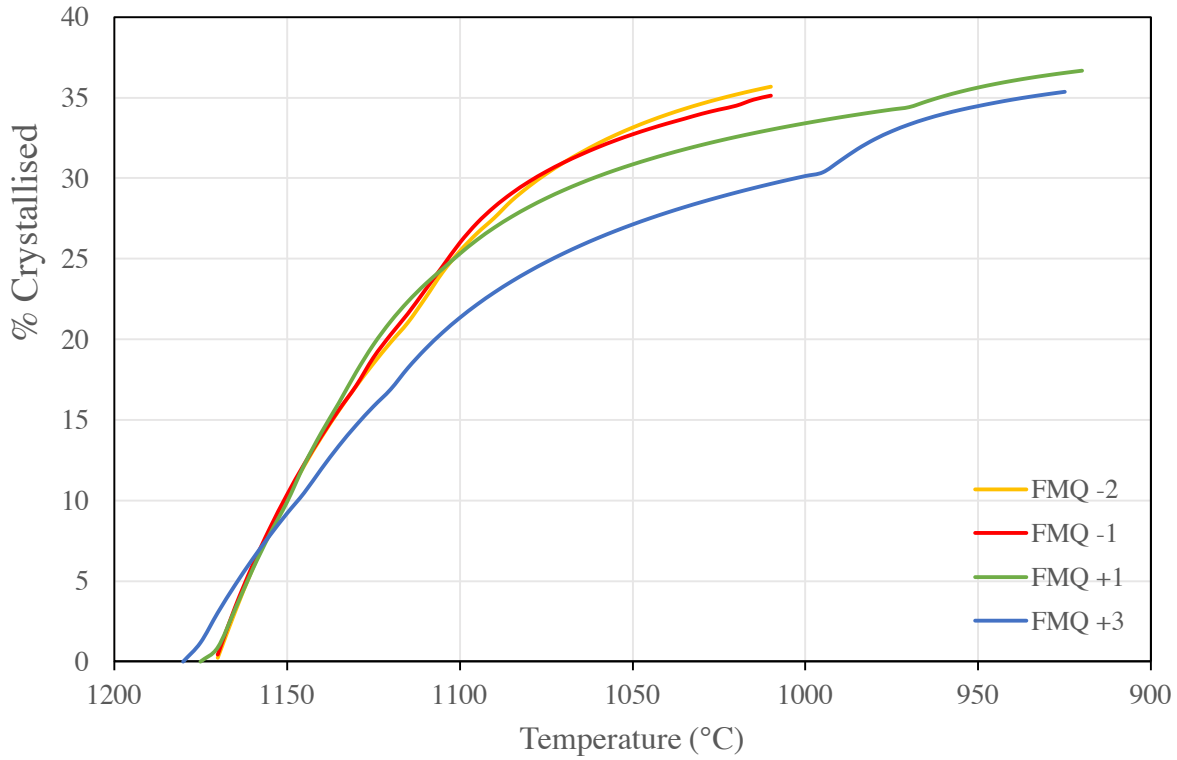

Figure 7. Plot of cumulative plagioclase mass growing from BGP melt, with decreasing temperature, for different fO2 conditions, from MELTS outputs.

Figure 7 shows the mass of plagioclase crystallising from melt as a function of temperature, in each of the MELTS runs described above. The highest temperature with plagioclase crystallisation is at 1170°C in all cases except at FMQ of +3, where it begins at 1175°C. These temperatures were used as a guide for the liquidus temperature for plagioclase crystallisation in experimental runs. In all cases in these simulations, the increase in mass started to level off at around 1000°C, as other phases started to grow. Figures 8a and b show the total growth for the different phases predicted to grow from a BGP melt at very reducing (FMQ-1) (Figure 6a) and relatively oxidising (FMQ+3) (Figure 8b) conditions. In both cases here, changes in growth of all phases with temperature starts to level off around 1050°C.

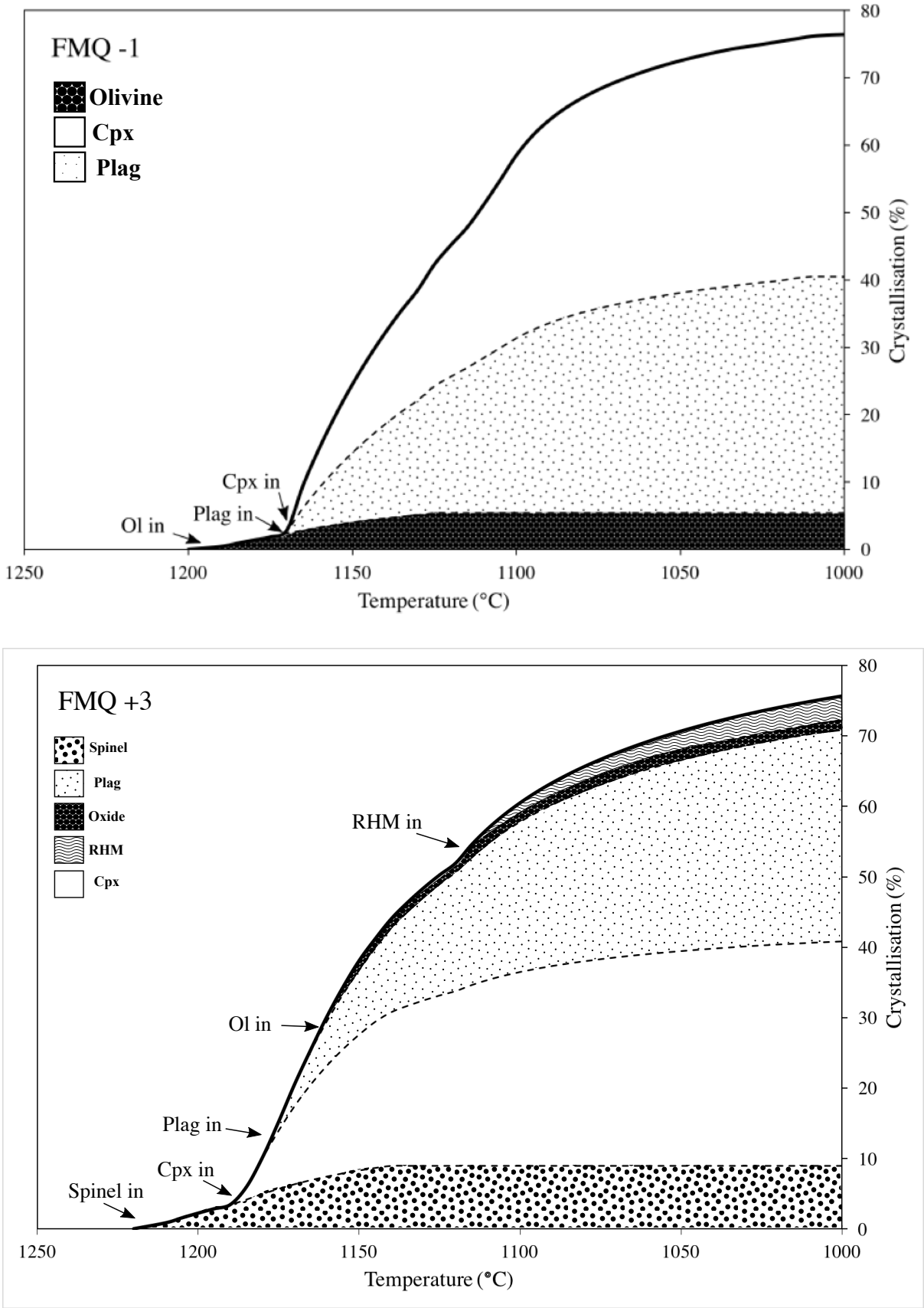

Figure 8a-b. Plot of phase growth with temperature from MELTS, from BGP melt for two contrasting fugacities (FMQ -1 (a) and +3(b)),

In addition to directly modelling the composition of BGP, MELTS was used to model crystallisation from melt of other basalts used in comparable studies. Compositions used in Pupier et al. (2008), Watanabe and Kitamura (1992), and Kirkpatrick (1977) were all used. Pupier et al. (2008) and Watanabe and Kitamura (1992) both use tholeiitic composition basalts in high temperature experiments, and the plagioclase crystals were then measured, and crystal size distributions and morphologies were investigated. This is directly relevant to this study since BGP has a composition typical of Hawaiian tholeiites (Oze and Winter, 2005). Kirkpatrick (1977) uses data from Makaopuhi lava lake in Hawai'i, which is an important and well-studied lava lake, especially in terms of plagioclase size and shape. These factors and similarities make these studies' compositions relevant to model for these experiments. The MELTS results can also be compared to their experimental results where possible. The compositions reported in these studies were input directly into MELTS, which was used to calculate liquidus temperatures and crystallisation of plagioclase as a function of temperature (Figure 9 and Table 5).

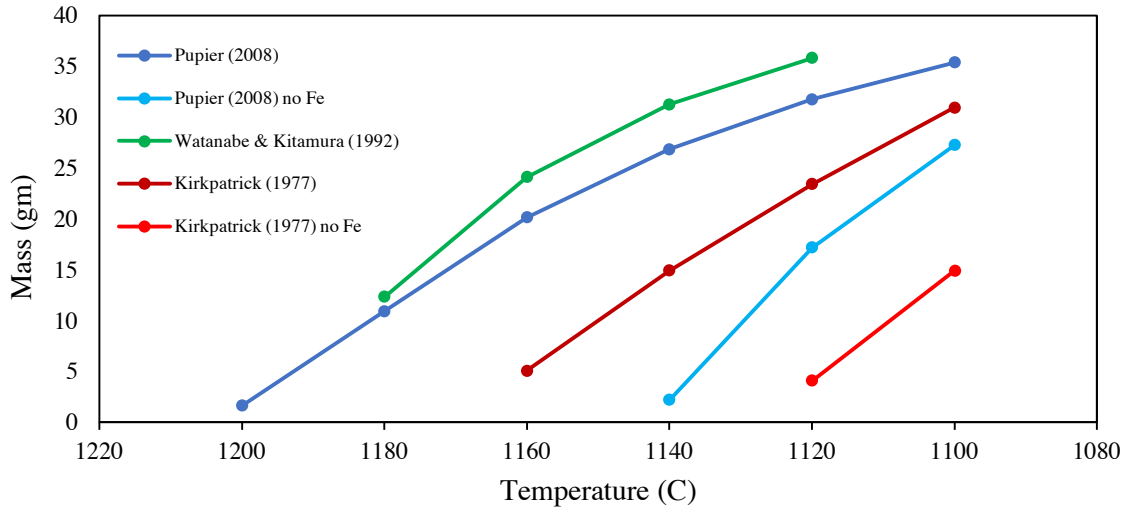

Figure 9. Plot showing increase of plagioclase mass as temperature is dropped, from Rhyolite MELTS simulations of different basalt compositions taken from the literature.

Composition	Description	Liquidus (C)
Pupier et al. (2008)	Ferrobasaltic dyke composition, assoc. with Skaergaard intrusion. (SC1). Synthetic glass powder.	1204.57
Pupier (2008) no Fe	Basaltic dyke composition, assoc. with Skaergaard intrusion. (SC1). Synthetic glass powder	1188.48
Watanabe and Kitamura (1992)	Tholeiitic basalt, glass. Synthetic glass powder	1195.12
Kirkpatrick (1977)	Makaopuhi sample M-1. Tholeiite	1205.35
Kirkpatrick (1977) no Fe	Makaopuhi sample M-1. Tholeiite.	1215.7

Table 5. Different compositions used in MELTS simulations with their origins and the calculated liquidus temperatures.

To summarise, the MELTS modelling shows that in general, plagioclase should begin crystallising from a BGP melt at 1170-1175 ºC, and clinopyroxene ± olivine ± oxides might also be expected to grow in the experiments. In light of these results, all experimental runs were planned to begin above 1175ºC, and to drop to that temperature and below it to induce new plagioclase growth. The actual eruptive temperature of BGP flows has been recorded at 1122.8°C using a K-type thermocouple inserted ~4cm into advancing lava flow fronts (Oze and Winter, 2005), which is a temperature ~52ºC below the plagioclase liquidus taken from MELTS modelling done for this study. From interpretations of the lower temperatures, higher density and lower F content, is thought that the plagioclase that is found in BGP on Kilauea was grown prior to extrusion, during a period of stagnation which allowed the lava to de-gas and cool (Oze and Winter, 2005), and therefore is likely to have grown at a higher temperature than the measured extrusion temperature. In order to generate melt and crystal growth in these experiments, the initial temperature was raised higher than the eruptive temperature, but cooling rates used would be appropriate to deeper within a cooling lava flow.

3.1.4 Cooling Rates in Natural Lavas

The cooling rate of natural pahoehoe lava flows was investigated in order to better understand the conditions for crystal growth within the top few cm of an active BGP flow and to help find appropriate cooling rates to be used in experimental runs. A priority for these experiments was to keep temperature conditions such that new plagioclase crystals would grow at a low undercooling, within an interface controlled regime, in order to grow crystals with regular morphologies (i.e. not diffusion limited growth where irregular morphologies break down measurements of aspect ratio). It was also important to keep growth within the interface controlled regime in order to make this work comparable to other studies, such as Holness (2014). Moreover, it was considered of interest to see how the experimental cooling rates compared to a natural cooling rate of a pahoehoe flow, which can help to bring insights into the ways that these results can be directly applied to understanding natural lava flows.

Kezsthelyi and Denlinger (1996) created a model for the initial cooling of pahoehoe flow lobes (BGP occurs as lava tube breakouts which advance as lobes). These lobes begin to form a glassy skin as they flow. Figure 10 shows the difference in flow lobes with flow speed, and the interaction of these lobes with the lava crust.

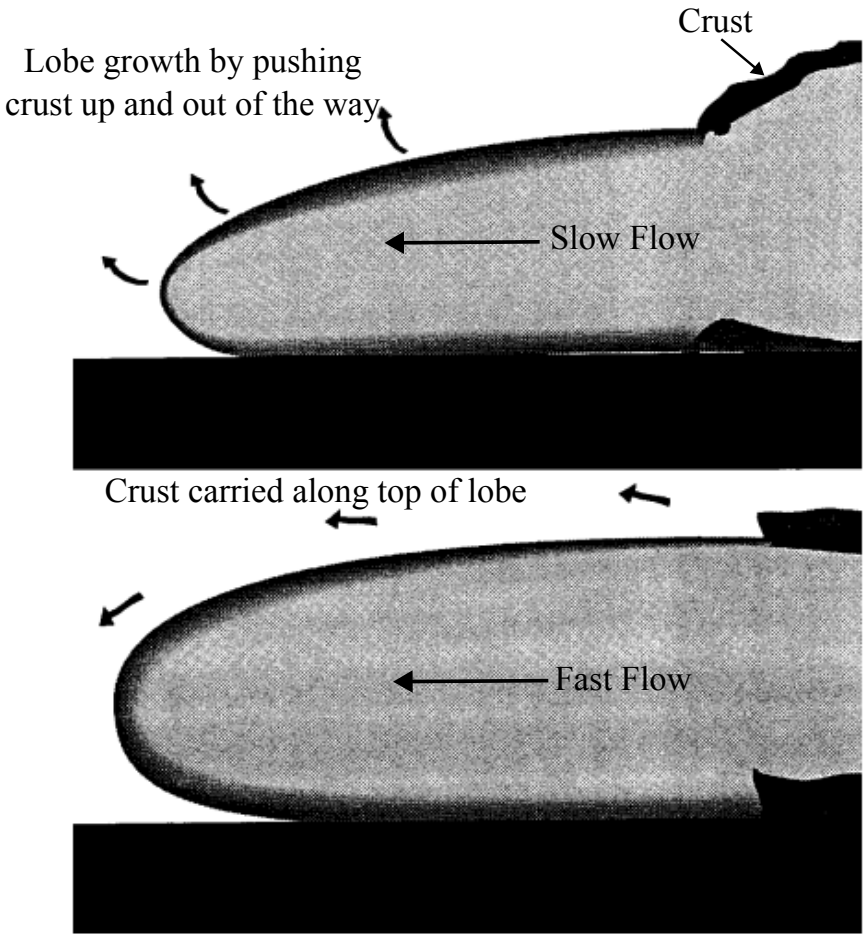

Figure 3.. Differences in pahoehoe lava flow lobes. Adapted from Keszthelyi and Denlinger (1995)

This model considered a number of different aspects that are potentially important to the cooling rate of a lava flow. These include conduction, atmospheric cooling, latent heat of crystallisation and radiative cooling, as well as the effect of vesicles. Radiation across vesicles can transport significant heat at high temperatures, and porosity lowers the bulk thermal conductivity of lava. However, these experiments aimed to produce little to no vesiculation in the lava via use of an anhydrous starting material. Their model results in the following mathematical problem, which they solve numerically and exhaustively:

$$\rho Cp(\partial T/\partial t) = \partial/\partial z\,(k_{eff}\,\partial T/\partial z) + \rho L\,\partial X_{cryst}/\partial t \quad (3)$$

$$q_{top} = q_{rad} + q_{conv} = k_{eff}\,(z = 0, t)\,\frac{\partial T}{\partial z}\,|_{z=0} \quad (4)$$

$$\frac{\partial T}{\partial z}\ (z = Z, t) = 0 \quad (5)$$

$$T(z, t = 0), T_o \quad (6)$$

where ρ is density, Cp is specific heat capacity, T is temperature, t is time, k is the effective thermal diffusivity, L is latent heat of crystallisation, $\partial X_{cryst}/\partial t$ is the rate of crystallisation with time, and z is depth. q_{rad} is the radiative heat loss, q_{top} is the surface heat flux and q_{conv} is the atmospheric convective heat flux – each of these can be calculated with equations described in Kezsthely and Denlinger (1996). This model resulted in plots which closely fit field data, including those of Hon et al. (1993), as shown in (Keszthely and Denlinger, 1996) (Figure 11). In the case of BGP, latent heat of crystallisation was ruled out as a major influence on crystallisation kinetics since field data showed no reheating of the lava after eruption (Oze and Winter, 2005; Keszthelyi, 1995).

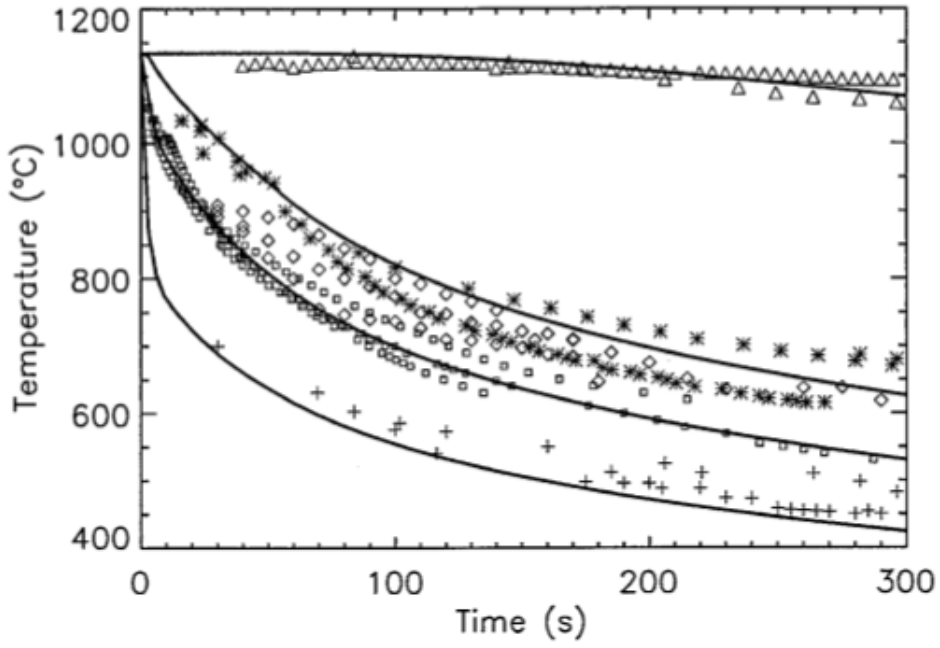

Figure 11. Taken from Figure 6 in Keszthelyi and Denlinger (1996). This figure shows a comparison between field data and the modelled cooling rates. The triangular points at the top of the figure represent temperature measurements taken at 2cm depth into the lava flow by Hon et al, in 1993. The rest of the plots represent very shallow (2-4mm) depths, or surface temperatures. The solid lines are the modelled temperatures.

When examining field data on cooling rates of pahoehoe lava, it was observed by Keszthelyi and Denlinger that the cooling rate would fit reasonably well to a purely conduction based thermal model, without the additional parameters. Radiative heat loss diminishes in importance to cooling rate as a crust forms on the progressing flow (see figure 10). Equation 7 was derived by producing a scaling analysis of Fourier's law (which describes thermal conduction), that simplifies the law into a calculation for cooling rate:

$$q = \Delta T \times D/(2 \times L^2) \quad (7)$$

where q is the cooling rate, ΔT is the temperature difference, D is thermal diffusivity, and L is the depth into the lava flow.

Temperature data taken directly from a 25cm thick cooling toe of a Kilauean Pahoehoe flow during May 1990, measured using a thermocouple and published by Hon et al. (1993), were used as a real-world analogue to help establish a reasonable cooling rate to use in the experimental runs. It is likely that the lobes sampled by Hon et al. (1993) were similar to those that produced the BGP samples used in this experiment.

Figures 12 and 13 show the field data from Hon et al. (1993), compared with the scaling analysis results. The plots of field data in Figure 8 and 9 both have a high R^2 value, with points that all lie in an almost straight line. This suggests that cooling rate was almost constant over the time period. The average measured cooling rate for the pahoehoe at 2cm depth was 13.63°C/min (1108-960ºC). The plot in Figure 13, for deeper measurements into the lava flow of 10cm, has fewer data points but maintains a high R^2 value and gives a much slower cooling rate of 0.8°C/min (1138 – 1028ºC). Using equation 7, with an approximate basalt thermal diffusivity of $1*10^{-6}$ m^2s^{-1} (Hanley et al., 1978), gave a cooling rate of 11.25 °C/min for the pahoehoe at 2cm depth, and 0.34ºC/min at 10cm depth. The measured cooling rates are similar to those calculated from the scaling analysis, possibly suggesting that at these depths into a lava flow of 25cm thickness, conduction is the most significant factor controlling lava cooling

rate. The bigger difference at 10cm depth may be due to the paucity of data points at this depth, or other heating effects such as latent heat of crystallisation.

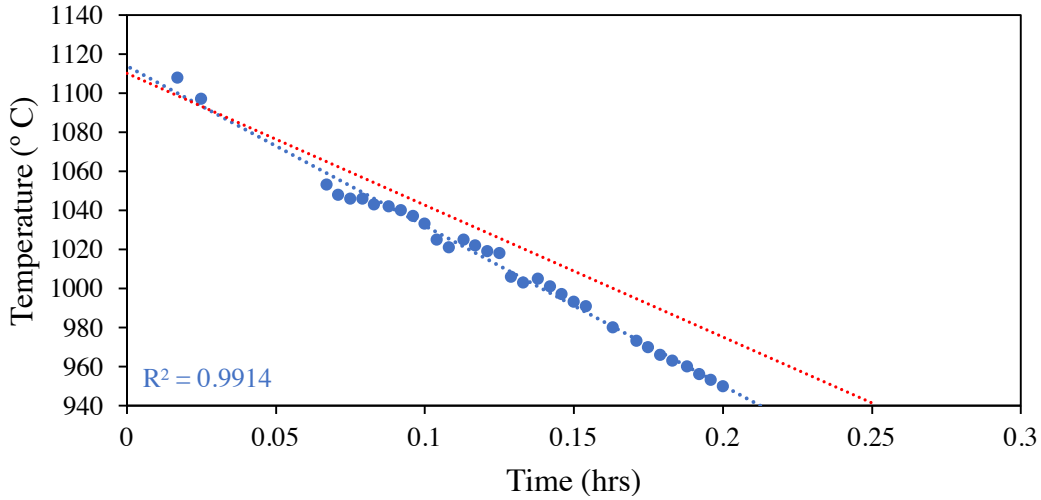

Figure 12. Plot showing cooling of a lava flow over time, from data provided in Hon et al. (1993 (blue)). These data were collected 2cm deep into a pahoehoe flow of ~25 cm thickness. The red line was derived from the scaling analysis described above.

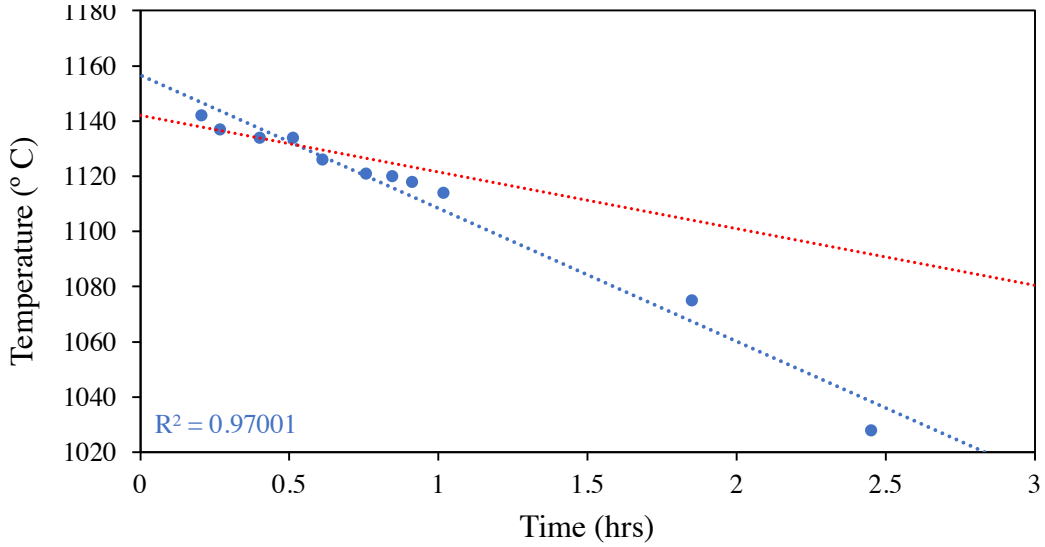

Figure 13. Plot showing cooling of a lava flow over time, from data provided in Hon et al. (1993 (blue)). These data were collected 10cm deep into a pahoehoe flow of ~25 cm thickness. The red line was derived from the scaling analysis described above.

These cooling rate values are also in line with the additional field data collected by L. Keszthelyi (presented in Oze and Winter, 2005), where the cooling rate ~4cm into a dense pahoehoe flow was measured as 9ºC/min. Work on lunar basalts finds that the critical cooling rate resulting in no crystallisation varies from 1 – 100°C/s, with most results above 8°C/s

(Uhlmann et al., 1979). These values are significantly faster than any of the measured or calculated cooling rates for BGP. Furthermore, Applegarth et al (2013b) also show that % crystallisation increases exponentially with decreasing cooling rate via measurements of enthalpy of differential scanning calorimetry results.

For these experiments, a cooling rate of 13°C/min or similar, as would apply to the top couple of centimetres of BGP, would result in a potential for insufficient data collection. For example, at 13°C/min, dropping to an undercooling of 40°C (i.e. 1140°C), would take 3 minutes. If such conditions were used in the experimental runs, this duration would make it difficult to find the optimal locations within the experimental sample for recording crystal growth, and to capture useful images. It is also possible that very few crystals would form. After 3 minutes, this cooling rate would drop to an undercooling below 40°C, which would begin to result in more skeletal and eventually dendritic plagioclase forms (Lofgren, 1974), which are difficult to measure and constrain. The natural cooling rate of the lava flows at this depth is therefore too fast for use in these experiments. The slower cooling rates of <1°C/min, as seen in the deeper regions of these lava flows, are therefore probably more appropriate for these experiments. In light of this, the cooling rates chosen for the first experiments were around 1°C/min, in order to allow time for the crystals to grow to a reasonable, measurable size and for data collection to be maximised. The cooling rates used in these experiments are representative of what would be expected at a depth of 10cm into a BGP lava flow.

3.2 Heating Stage Experiments

3.2.1 Preparing the Wafers

The first step in the experimental methods used in this investigation was to create the wafers of lava that would be used in the heating stage experiments. To create the wafers of blue glassy pahoehoe, a piece of the exterior of the sample was broken into 2-4 mm wide chips using a hammer. From these, the glassiest pieces were chosen by eye to be thinned down into wafers. The thinning down process involved setting the rock chip onto a slide using Crystalbond and a hotplate heated to 150°C, then progressively grinding and thinning the wafer down using SiC polishing papers with progressive smoothness. The wafers were polished on both sides. The first wafers used were thinned to 80 μm, but wafers for later experiments were thinned to 40-60 μm in an attempt to reduce oxide growth and obscuration of the sample. The thickness of the wafer was measured using a digital calliper, with a resolution of +/- 10μm to ensure the desired thickness had been reached during polishing. The slide was then reheated on the hot plate to melt the Crystalbond, and the thinned wafer was removed and cleaned with acetone to dissolve any remaining Crystalbond. The wafer was then air dried and placed inside a gelatine capsule for storage until use in a heating stage experiment. The dimensions of the wafers used in each experiment are described in Table 6.

Sample	Length (mm)	Width (mm)	Thickness (μm)
1	1.5	1.0	80
2	3.3	1.3	60
3	1.7	1.5	50
4	1.55	1.4	60
5	3.3	2.5	40
6	3.3	2.4	40
7	4.3	3.7	40

Table 6. BGP sample dimensions used in each run

3.2.2 Heating Stage

The heating stage experiments were conducted using a Linkam TS1400XY high temperature stage, which was attached to a microscope fitted with a camera and a x10 long working distance objective lens. The heating stage and camera were controlled by Linksys32 (Linkam Scientific) temperature control and video capture software. The heating stage has a maximum temperature of 1400ºC and a maximum cooling/heating rate of 200ºC/min, with maximum fluctuations of 0.1°C.

Setting up the Heating Stage

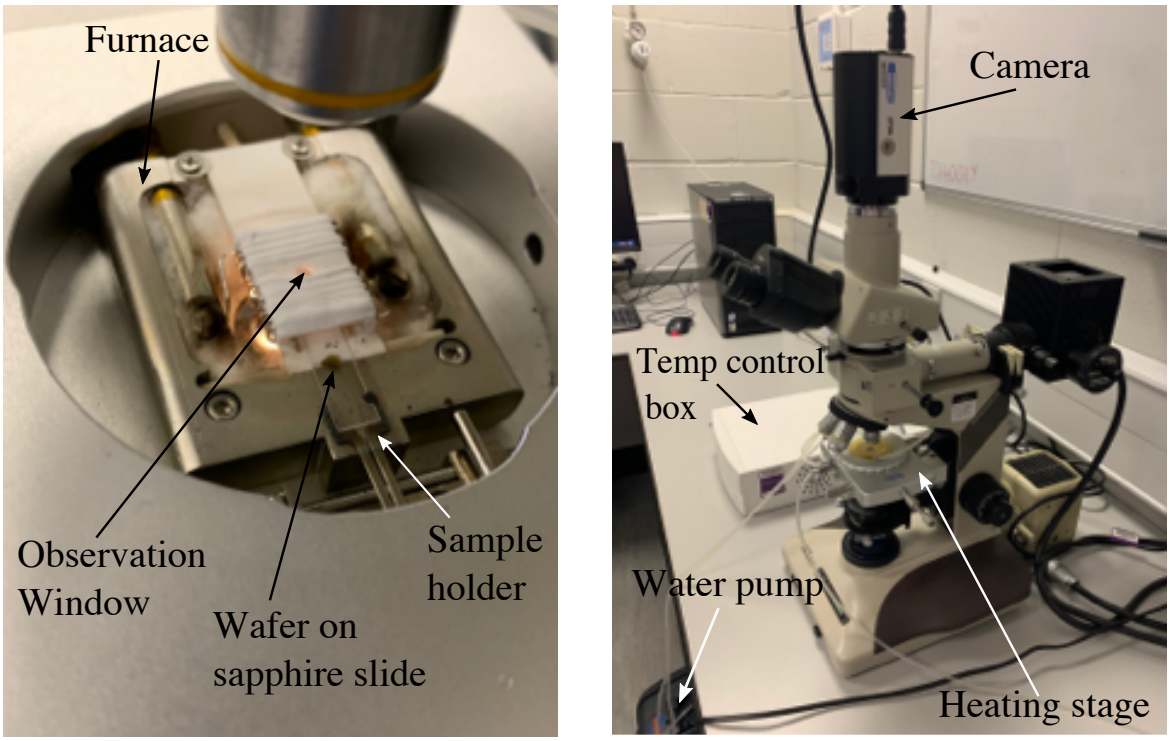

Figure 14. Experimental set up of heating stage, used in all experiments.

The heating stage is set up as shown in Figure 14. This was kept the same in all experiments. Nitrogen gas flowed at 40cc/min into the central open chamber, and over the sample and furnace, throughout the experiment, with an outlet on the opposite side of the chamber. Before the hot stage began heating, the chamber was flushed with nitrogen for at least 10 minutes, to minimise the amount of oxygen remaining in the atmosphere around the sample and limit

oxidation on the surface of the sample. In maintaining the same atmosphere in every experiment, we keep the fo_2 consistent across every run.

The body of the heating stage was cooled by cold water that was pumped through a series of tubes and internal channels in the stage. Observation windows at the top of the furnace and within the lid allowed the sample to be viewed via the microscope and attached camera. The heating stage was connected to a controller, which was connected to a computer, allowing the experiment to be controlled by the computer. The sample was placed onto a sapphire slide, which had a notch in it that allowed it to be gripped by a sample holder in the stage (Figure 14). The sample holder was manipulable in both the X and Y directions, allowing for the sample to be moved around to locate the best sites at which to obtain useful data. The sample was moved into and out of the furnace by this arm in the X – direction. The arm holding the slide had a quick release mechanism that allowed the wafer to be removed from the furnace and quenched immediately at room temperature after each experimental temperature profile was completed, thereby preserving the textures created in the experiment.

Camera

The camera used was a QICAM Fast1394 FireWire digital CCD camera. The camera was connected to the computer via FireWire and image capture was controlled by the Linksys32 software. A live image was available through the whole experiment to enable the clearest images of the crystals within the samples to be taken, and constant observations to be made in real time. Photographs were captured manually throughout each run at points of interest, whilst a set of images was also captured at a steady rate. The image capture delay was set within the software. The delay was set to take one photograph every 30 seconds during initial heating, and then at every 5-10 seconds during the run. In order to keep the total volume of data reasonable for longer experiments, we increased the gap between photographs to 10 seconds.

A final step was added at the end of the run that maintained the final temperature, but only has photographs taken every 3 minutes. This was to prevent the heating stage from immediately cooling to room temperature after the run ended and allowed sufficient time for quenching the sample. An example of a temperature profile showing the data taken is shown in Figure 15.

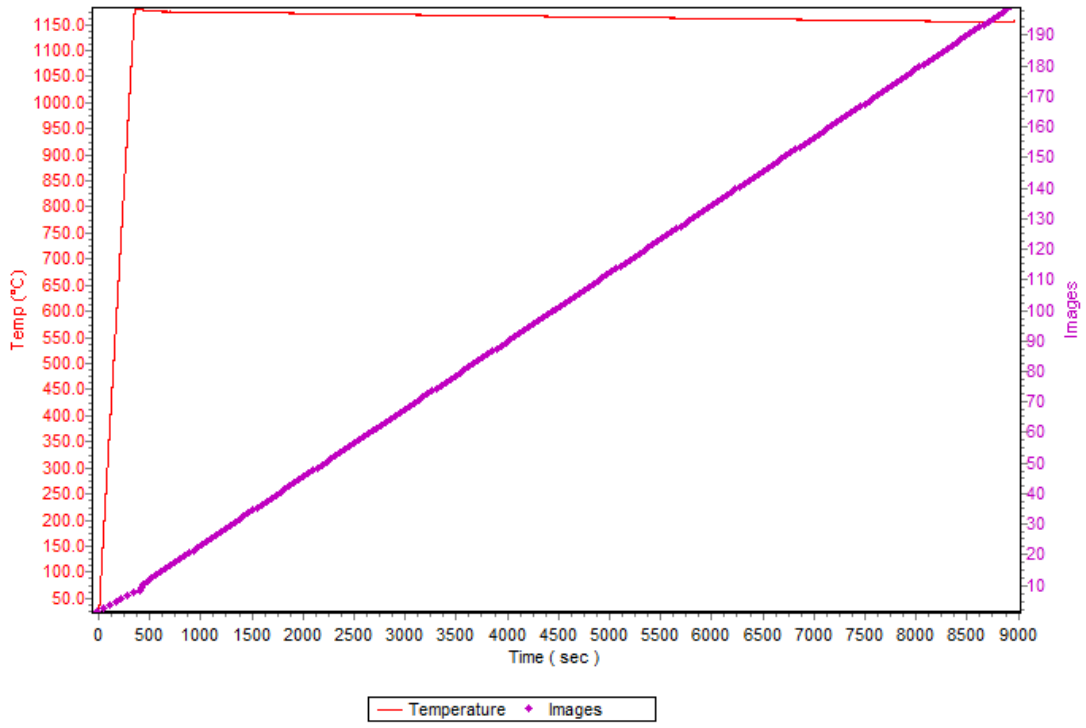

Figure 15. The temperature-time profile for experiment 6. The purple points here show the images that were taken during the experiment. The remaining T-t profiles can be found in the appendix.

3.2.3 Temperature Conditions used in Heating Stage Experiments

Temperature profiles used in the experiments were controlled by Linksys32 on the computer. The input of these was the temperature (ºC), how long the sample was held there for (s), rate of temperature change (ºC/s). These are described in detail in Table 7. Full details, including the experimental temperature-time ramps are available in the appendix.

Run	Max T (ºC)	Time held at Max T (s)	Quench T (ºC)	Number of steps	Mean Cooling Rate (ºC/min)	Cooling style	Notes
1	1225	400	1150	5	1.7	Step	This run was used to establish the behaviour of the BGP sample during the experiments, but useful data was gathered regardless.
2	1180	180	1150	3	0.63	Step	Held at 1180ºC for only 3 minutes before dropping straight to 1160ºC.
3	1180	600	1150	2	1	Step	Held at 1180ºC for 10 minutes instead of 3, since growth was observed at sample edges.
4	1180	180	1140	3	1.4	Step	Dropped straight to 1160ºC after 3 minutes at 1180ºC due to extensive oxide growth on surface.
5	1180	60	1140	1	1	Ramp	Vertical ridge develops on sample at 1150ºC, obscuring a lot of it.
6	1180	60	1155	2	0.1	Ramp	Dropped to 1175ºC after 1 min at 1180ºC, then on ramp to 1155ºC. Quenched immediately upon reaching 1155ºC.
7	1180	60	1150	1	0.5	Ramp	Held for 2 mins at 1150 ºC before quenching.

Table 7. Experimental conditions implemented in runs 1 -7. The mean cooling rate is known to within 0.025ºC/min.

In some cases, temperature had to be dropped earlier than planned to try and avoid over oxidation of the surface leading to too much of the sample becoming obscured. A couple of the samples were not immediately quenched, and were held at their final temperature for a few minutes in order to obtain final observations and images of the sample before removal.

The temperature profiles and software were set up in such a way that enabled the temperature to be changed immediately at any time, allowing for responses to be made to observed changes. The temperature was brought up to just above the liquidus (to 1180ºC) in all but the first experiment, where it was taken to 1225ºC. Runs 5, 6 and 7 used a constant cooling ramp, rather than steps. This allowed for a direct comparison between experiments with similar/the same average cooling rates where one was carried out in steps and the other with a constant cooling rate, but both reaching the same degree of undercooling. It is unlikely that there was any temperature gradient across the furnace or within the sample, in either the horizontal or vertical direction.

3.2.4 Surface Oxidation

During all of the experimental runs, a layer of oxide formed on the surface of the sample, and oxides growing within the body of the sample darkened it. The oxides obscured crystal growth in the areas where they covered the sample surface. A similar effect was described in Applegarth et al. (2013a). In order to attempt to reduce this, the length of time allowed for nitrogen to flow into the chamber before the start of each run was increased. This did not show any significant reduction in oxidation. Additionally, wafers were thinned further from 80 to 40μm, to try to reduce darkening and oxidation. Surface oxidation continued to occur, but the thinner samples were lighter in their central regions than previous runs.

Once vesiculation had significantly reduced, if oxides were beginning to form in a way that significantly obscured and darkened the sample, the temperature was dropped before the pre-set time in order to attempt to record plagioclase growth with minimal obscurity by oxide crystals. Decisions were made during each run about when to drop the temperature further based on ongoing observations and in reaction to events such as increased oxide growth or if

no change in crystal growth was observed after a hold of a few minutes at that temperature to attempt to stimulate and observe growth. After each run, the results and conditions that the experiment were carried out in were reviewed, and the observations made in previous experiments were used to plan the next, taking into consideration how many plagioclase crystals were able to be observed and the level of oxide obscurity at each stage of cooling.

3.3 Data Collection and Analysis

3.3.1 Photomicrographs

Photomicrographs were taken of the wafer pre-run, and of the cooled sample after each run. These were taken using a Zeiss Axioscope microscope, which allowed the image to be viewed through a monitor, allowing for the best possible images to be taken. Photomicrographs were taken at 4x, 10x, 20x and 50x magnification. Photographs were taken across the whole sample. These images were used to record as many individual crystals for measurement and analysis as possible, and to image the textures and spatial variations within the cooled run samples. The samples were polished for SEM analysis after initial post-quench optical imaging. The newly polished samples were also imaged in the microscope, in order to get new images without the obscuring oxide layer that had formed on the surface of most samples. Polishing also reduced difficulty in focussing images caused by the doming of the sample. A catalogue of these photomicrographs, as well as maps of each sample with the imaged areas marked on can be found in the supplementary materials.

3.3.2 SEM analysis

Each of the samples were prepared for use in a Scanning Electron Microscope (SEM) after each of the experiments. This preparation involved polishing the sample in a Buehler Micropolish 0.3μm Al_2O_3 slurry. The samples were then coated in carbon to make them conductive, and were imaged using a Zeiss Evo SEM. Both secondary electron (SE) and backscatter electron (BSE) images were taken of the samples, with a focus on BSE images in order to clearly define different minerals.

A thin section of a sample of BGP was made and also imaged using the SEM in this way to analyse the crystal textures through the original natural sample in order to fully characterise the top few centimetres of the BGP.

Fully quantitative Energy dispersive X-ray Spectroscopy (EDS) analyses were performed on a representative selection of crystals from each phase found in a sample of the experimental runs. Runs with contrasting cooling rates and quench temperatures were chosen as representatives. The same analysis was then carried out on a thin section of the BGP for comparison.

3.3.3 2D Measurements

Crystal size measurements from the images described above were made using ImageJ (Schneider et al., 2012). Crystal sizes were measured using the line tool, using a scale appropriate to that image's magnification. The longest axis was measured as the crystal length, with the width as the axis horizontally perpendicular to that i.e. the shortest axis of the 2D crystal image; this was applied to all crystals including those which appeared as irregular shapes due to how they were intersected by the sample surface (illustrated in Figure 16).

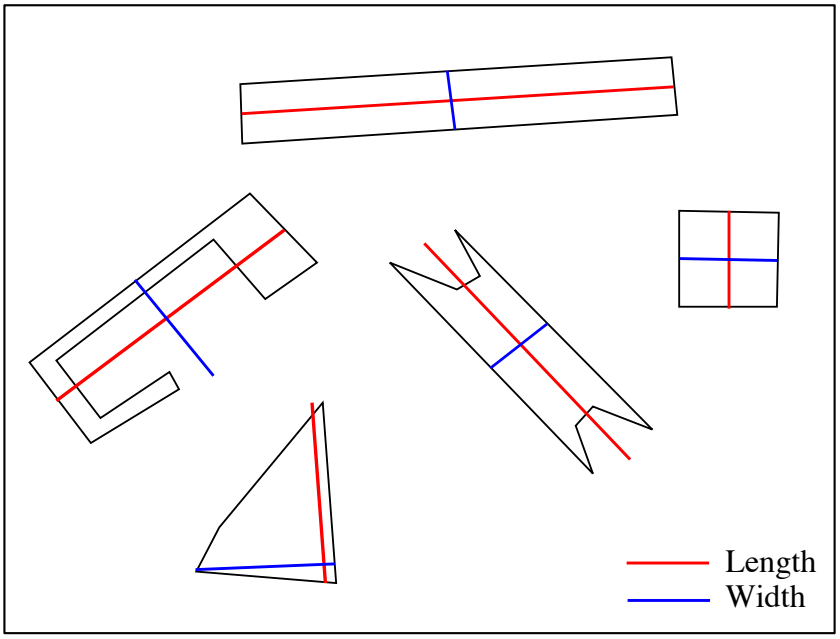

Figure 16. Illustration of how lengths and widths for different 2D plagioclase crystal shapes were measured.

Only the most in-focus crystals were measured in each photomicrograph, to ensure that what was being measured was a true crystal size, and care was taken not to measure the same crystal multiple times, since there was crossover in the area covered by different images. Crystals that were cut off by the edge of the image, or were too out of focus, or heavily obscured by oxide growth, were not measured in order to avoid incorrect measurements. A minimum of 200 crystals were measured for each sample, to ensure a large representative population.

Measured Quantity	Method
Crystal Length and Width	ImageJ line tool
Crystallinity	ImageJ threshold/ particle analysis
Oxide Halo diameter	ImageJ line tool
Crystal Number Density	Image J for area/ manual counting

Table 8. Summary of measurements made from images taken during and after experiments.

The measurements were then processed in Microsoft Excel (2017) where a variety of data analysis methods were carried out. The length and width measurements described above were used to calculate crystal aspect ratio as the length divided by the width. Analytical methods included plotting of histograms for length, width and aspect ratio data, finding modal and mean values for size and aspect ratio, and where possible plotting of growth over time.

3.4 Synthetic Powder Experiment

A single trial experiment for use of a synthetic glass powder in a heating stage experiment was done in order to test the effects of using an iron free composition, and to attempt to grow plagioclase crystals in an oxide-free environment. For this, 10mg of Fe-free, rhyodacite glass powder was mixed with <1 wt% plagioclase seeds (produced by crushing and grinding a plagioclase crystal under ethanol) and was placed onto a sapphire slide in a 4.3mm x 4.9mm pile. The powder was heated to 1300°C and held for 20 minutes until the glass had completely melted into a colourless melt containing plagioclase seeds. The sample temperature was then dropped to 1100°C for 15 minutes, where some growth of plagioclase was observed; and then to 1175°C for 25 minutes where slow growth continued, then to 1160°C for 10 minutes. Plagioclase growth in this experiment had a spinifex texture (Figure 17) and new growth was entirely heterogeneous, nucleating from the plagioclase seeds. It was decided that analysing

this texture and growth style was not relevant to this study since it is not representative of natural growth, so this experiment style was not continued or analysed further.

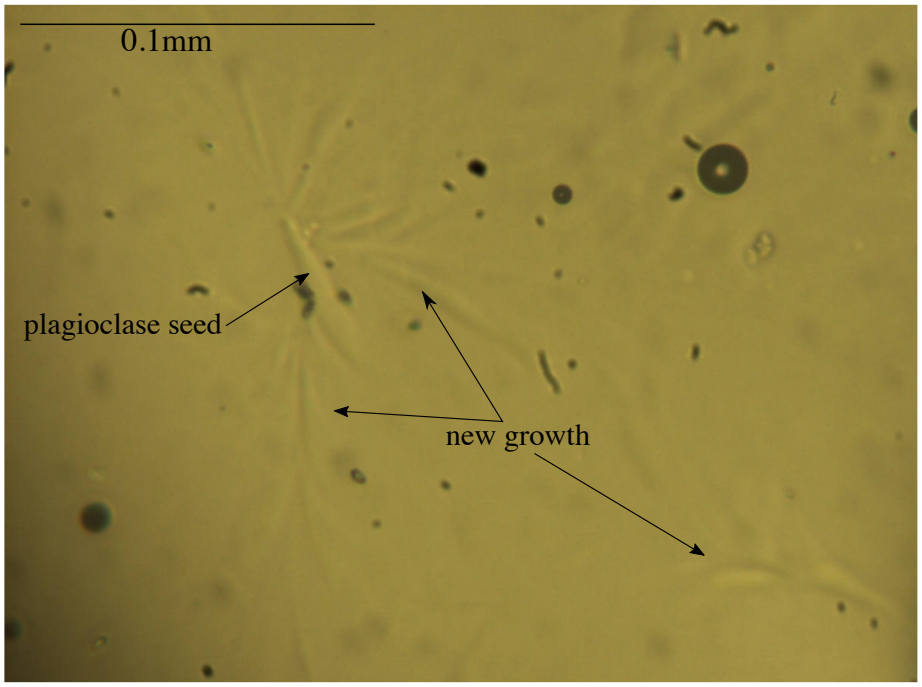

Figure 17. Photomicrograph from the test run experiment using synthetic powders rather than BGP glass. New growth around plagioclase seeds shows spinifex textures, and is not a good analogue of natural growth in basaltic lava flows.

3.5 Sources of Error

The uncertainty in direct measurements of crystal dimensions using ImageJ is likely to be only a couple of pixels, since that is an approximate human error made when measuring on a computer screen. This pixel error was calculated via repeated independent measurements of the same crystals. This translates to an uncertainty of 1μm for optical photomicrographs, and 0.6-1.5μm for SEM images (dependent on the magnification of the image), for both length and width measurements. This meant that length measurements had a smaller % uncertainty compared to widths. The uncertainty in aspect ratio was measured by calculating the difference between the measured aspect ratio and the largest and smallest possible aspect ratios, based on the errors in length and width measurements. Measurements taken from SEM images often had

a smaller uncertainty since many images were taken at higher levels of magnification. Furthermore, larger crystals were easier to measure as they were better delineated in images, so there was some skew towards those, particularly in microscope photos taken during early stages of heating stage experiments where the majority of crystals were small ($L < 10$ μm).

The furnace had a temperature uncertainty of ±1 °C, and was calibrated using pure gold metal.

Other sources of potential error and skewing of the data that may have arisen, were the spatial differences across the sample causing a bias of measurement. Where the sample was glassier, it was significantly easier to clearly see individual crystals using an optical microscope. The more oxides there was on any sample, the more they obscured crystals and prevented accurate measurements. Additionally, since the samples varied in quality i.e. how much they were obscured by early growth of oxides, this meant that the experiments that resulted in the least oxide growth were able to produce the most data on plagioclase crystal size and growth. There was also error associated by the fact that in samples 6 and 7, where groups of crystals were measured in one area over time, it was not exactly the same group of crystals each time, only the same area in the sample. Only where individual crystals were tracked was there certainty that it was the exact same crystals.

There may have been some uncertainty in the total time of crystallisation used in calculations for experiments where it was not possible to directly observe the same group of crystals over time, and where quenched product measurements were used for an average growth rate. This error occurred due to the fact that in some cases it was not clear exactly when crystals stopped growing – usually this was due to oxide cover making crystals difficult to observe in the later stages of several experiments. There is unlikely to have been any significant uncertainty in the measurement of time for the heating stage controls and image capturing software. However, it was impossible, with the resolution of the camera used to track the exact timing of the onset of

crystallisation. There is approximately 1 minute after the onset of cooling in each experiment during which crystallisation begins, but crystals are not yet large enough to be visible. This translates to an average uncertainty of the cooling rate of 0.025ºC/min. The uncertainty in growth time was also used to calculate uncertainties for growth rates of crystals in each experiment.

4. Blue Glassy Pahoehoe

Dense Blue Glassy Pahoehoe (BGP), also known as P-type (pipe-vesicle bearing) pahoehoe is an extrusive igneous rock that forms from pahoehoe flows that occur in the lower Kalapana flow field on Kilauea in Hawai'i down to the coastal plains. Samples from this lava flow were collected in 2016 and used to make the wafers for the experiments carried out in this study. BGP is an ideal material for these experiments as it has an upper layer which is comprised of natural and unaltered glass with low volatile content, which is useful for these experiments since it provides a natural starting material that requires minimal preparation and does not contain many large crystals or bubbles that may affect nucleation. BGP also has a basaltic composition (shown in Table 9), which creates a desirable low-viscosity melt. This is ideal for growing crystals within a reasonably short time frame. This chapter will detail and characterise the BGP basalt, which is used as the starting material for all experimental runs in this study.

	SiO_2	TiO_2	Al_2O_3	MgO	MnO	Fe_2O_3	CaO	Na_2O	K_2O	P_2O_5	Total
Oze and Winters (2005)	51.7	2.62	13.4	6.18	0.17	11.9	11.1	2.38	0.45	-	100
Llewellin	50.1	2.78	13.38	8.10	0.159	12.25	11.52	2.29	0.521	0.266	101.4

Table 9. Major element composition of BGP reported by Oze and Winters (2005) (from microprobe glass analyses), and Llewellin (EDX, Personal communications).

4.1 Sample Geological Context

The majority of lava erupted from the Pu'u 'O'o - Kupaianaha Vents on the Kilauea volcano between 1986-2002 were pahoehoe lavas (Oze and Winter, 2005). Lavas flowed down the massive slump scarp of Pulama Pali, where they reached the ocean and formed a "lava delta" flow field. The lavas were both surface and tube-fed (Oze and Winter, 2005). Dense Blue Glassy Pahoehoe, along with the more abundant spongy pahoehoe can be found on the Kalapana lava delta, as well as the coastal plain (Hon et al., 1994). The sample used to prepare the wafers used in these experiments was collected on 29/08/2016 from a tumulus overflow from lava emplaced in approx. 1998, on the coastal plain below Pulama Pali, near Kamokuna (19.322ºN, 155.0458ºW), on Big Island, Hawai'i.

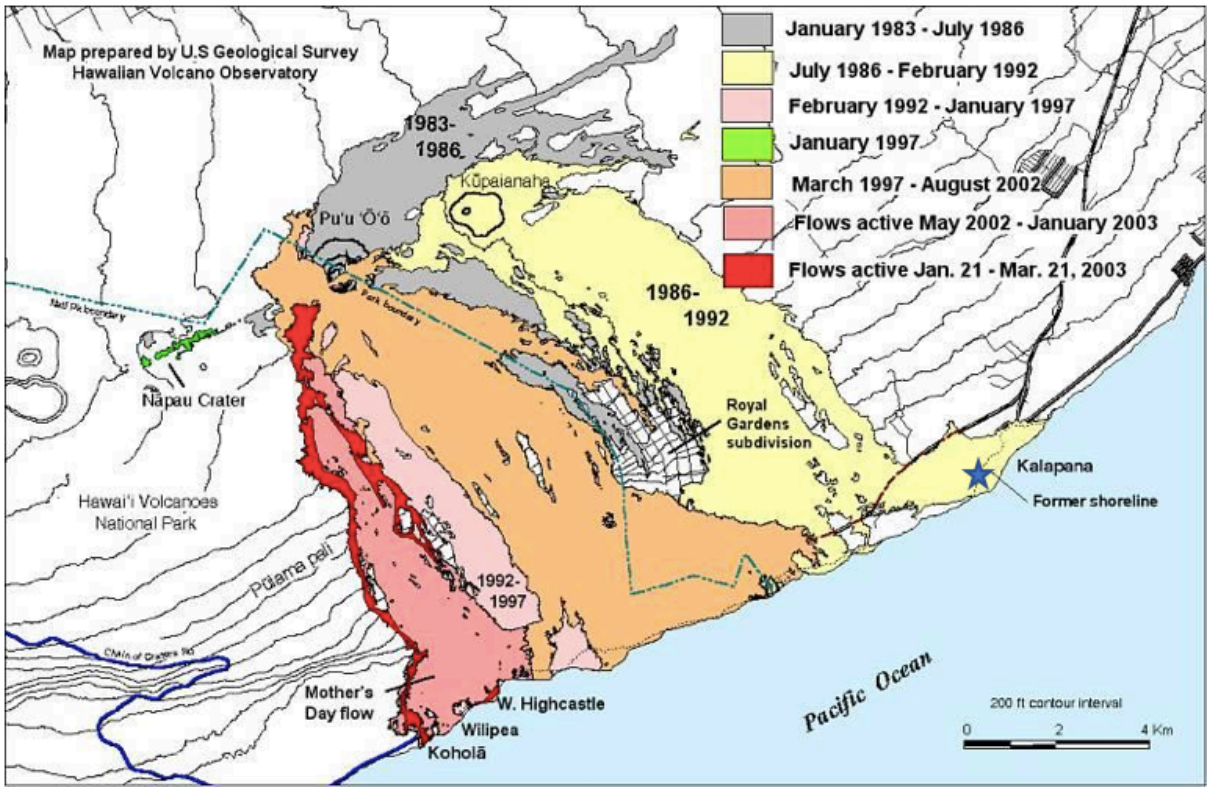

Figure 18. Map of lava flows erupted from 1983- present activity of Pu'u O'o and Kupaianaka, on Kilauea, USGS. Blue star near Kalapana denotes sample location.

4.2 Formation of Blue Glassy Pahoehoe

BGP is commonly found on flatter ground (with slopes of <4º), such as coastal plains, rift zone crests and around a summit caldera, where pressurised features such as tumuli are widespread and where expansion clefts grow, allowing lava moving below the surface to degas without significant cooling (Oze and Winters, 2005; Wilmoth and Walker, 1993). Wilmoth and Walker (1993) put forward the theory that the lower vesicularity in the outer zone of the lava compared with the inner selvage is due to surface tension effects causing gas to move inwards, rather than outwards. It is also proposed that the pipe vesicles act as conduits for the gas loss from the lower selvage of the lava flow, which has a low vesicularity. Hon et al. (1994) suggest that the BGP may represent pressurised lava that contains more volatiles than the spongy pahoehoe, thus explaining the increased vesicularity in the interior of the lobes, as well as their formation at high pressure zones. Furthermore, it is suggested that the dense rind that forms on the lava resists inflation, increasing the pressure within the lobes, and causing bubbles to dissolve back into the melt. This, however, may not completely explain how the dense outer rind remains almost entirely un-vesiculated after extrusion. Figure 19 below, illustrates the key differences between spongy and dense blue glassy pahoehoe.

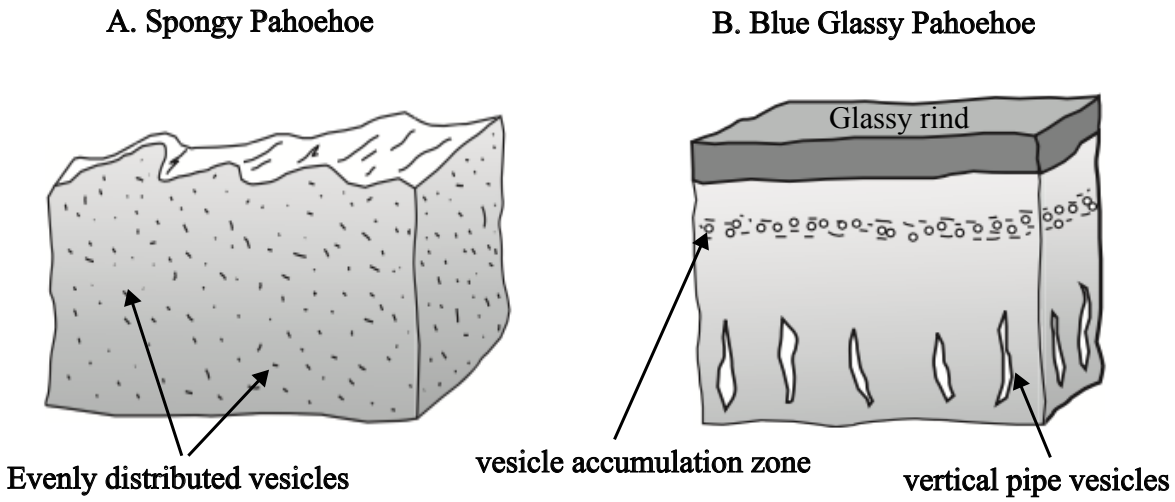

Figure 19. Cross sectional diagrams of spongy and blue glassy pahoehoe, adapted from Oze and Winter (2005)

It is worth noting that the interior of the flow lobes was not cooled at the same time as the outer zone, since the interior is filled with lava that continued to flow through the lobe as the lava flow progressed. It has been proposed that, prior to extrusion, the lava was able to pick up crystals of plagioclase, olivine and augite that had grown in the lava tube prior to extrusion (Oze and Winters, 2005). This may account for some larger plagioclase crystals seen in the lava, and for the presence of equilibrium plagioclase shapes in the top 2-3cm centimetres of the rock, where the high cooling rate would lead to the growth of more skeletal and swallowtail crystal forms (Lofgren, 1974). It is possible that the dendritic and swallowtail growth seen off the corners of some pre-existing crystals may be due to the sudden increase in cooling rate experienced by these inherited crystals (see Figure 22C).

4.3 Field Characteristics

There are two main types of pahoehoe that are erupted from Hawaiian volcanoes. The first is P-type (BGP), and the second is the S-type (spongy) (Oze and Winter, 2005). The spongy pahoehoe is often described as golden and is significantly more vesiculated than the BGP. The diagnostic characteristics of BGP are its silvery-blue surface colour (although this fades over time), its high density and low vesicularity, and outer glassy rind. This lava usually breaks out of pressurized uplifts, such as tumuli, in well-developed flow fields. The lava flows are often thin and highly mobile, and advance as a series of narrow ‘toes’ (Llewellin, personal communication; Oze and Winters, 2005). Field observations note that as the lava flows, it quickly develops a 1-2mm thick visco-elastic skin, which inflates as lava passes through the extending toes (Hon et al., 1994). The lava erupts at 1123ºC (Oze and Winters, 2005), which is a cooler eruption temperature than that of the spongy pahoehoe (1136ºC). Figure 20 below shows a photograph of a hand sample of BGP. Some of the lustrous blue sheen is still visible

on the ropey surface; alongside this is a still image from a video of an incandescent BGP lava flow.

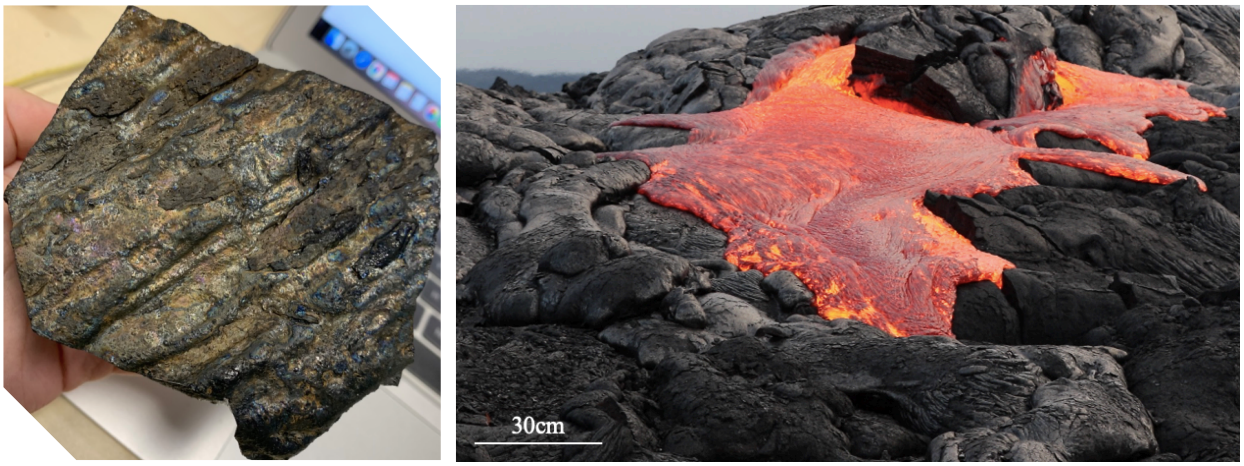

Figure 20, Hand sample of Blue Glassy Pahoehoe (left), and a photograph of a dense blue glassy pahoehoe lava flow (Warren Fintz, Personal Communications, 2016).

There are several theories pertaining to the origin of the blue surface colour this lava takes on once cooled. Wilmoth and Walker (1993) suggest that this colour may come from a thin oxidised coating on the lava that causes light interference, and that this same coat is spalled off of S-type pahoehoe. Following some X-ray photoelectron spectroscopy, Oze and Winters (2005) found that the surface of the BGP had a higher concentration of iron, magnesium and oxygen than golden, spongy pahoehoe. They surmise that the blue colouring could come from light scattering caused by a coating of Fe-Mg oxides. Since the colour of this lava eventually fades to grey, it is possible that there is more, older BGP that has not yet been identified as such, but can be identified once the interior of the lava flow is examined.

4.4 Petrology

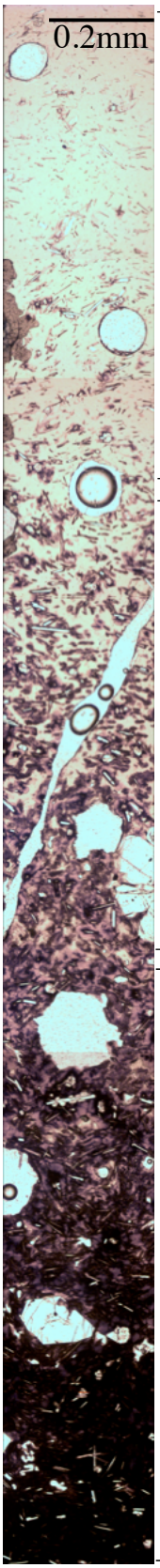

Figure 21. BGP thin section

Blue Glassy Pahoehoe displays three distinct layers once cooled. The figure on the left (Figure 21) shows a slice of a thin section from the BGP used in this study, from an outer, glassy layer down to a crystalline interior a few centimetres deep within the flow. The outermost upper layer is a highly glassy zone which is normally <1cm thick, containing only a few scattered phenocrysts (0-13% total crystallinity) – mainly olivine and plagioclase (Figure 22A and B). These crystals are generally euhedral and are likely to have grown in the lava flow interior (Llewellin, Private Communications), or during storage. Some olivine crystals towards the top 2cm of the sample display dendritic growth emanating from their corners, as well as acting as points for heterogeneous nucleation of plagioclase and augite crystals (Figure 22C). Many of the olivine crystals are rounded and have embayments, indicating resorption. Below this is a 1-3mm thick transition zone with an increasing crystallinity, rising to ~50% total crystallinity. In this zone, the 'pillowy blobs' (as described in Oze and Winters (2005)) of augite are seen (Figure 22D and E). These forms increase in quantity and size with depth into the BGP sample, until they dominate the texture of the rock. The 'blobs', when viewed in the SEM at a high magnification, are seen to be dendritic growths of augite crystals with intermingled plagioclase that spread outwards from their nucleation points on pre-existing plagioclase and olivine crystals, indicating a heterogeneous nucleation (Figure 22). These dendritic forms are likely to be growing outwards from the crystal to more efficiently reach less depleted zones,

within a diffusion limited growth regime (Oze and Winter, 2005). Below that is a layer further into the interior of the flow that is significantly more crystalline (over 70% total crystallinity), containing primarily augite, plagioclase and olivine (Figure 22F). The entire sample generally has a low vesicularity, with a few isolated round vesicles. Vesicularity increases with depth, where there are very few bubbles towards the glassy rind, but more and larger vesicles are seen in the crystalline zone of the lava. Vesicles in the crystalline central zone of the lava flow coalesce to form pipe bubbles (Wilmoth and Walker, 1993; Oze and Winters, 2005). Even in these more vesicular regions vesicularity is lower than for more common spongy pahoehoe. The mineral assemblage does not change throughout the whole rock.

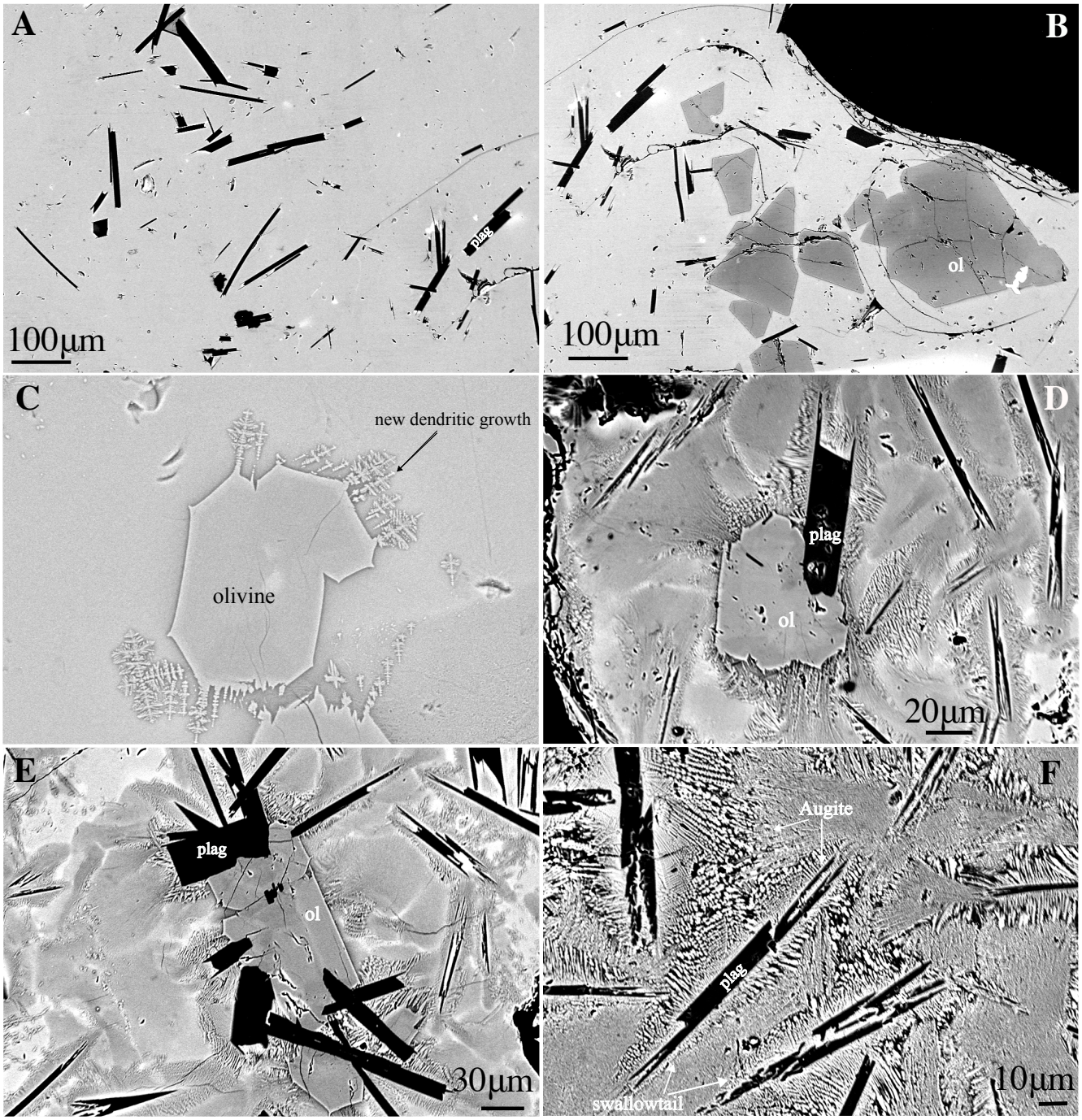

Figure 22. A-F, Backscatter electron SEM images of the BGP sample thin section. A and B are taken from the glassy zone towards the top of the sample, where the augite blobs are not present. B shows rounded and embayed olivine crystals. C shows dendritic growth from the corners of an olivine crystal just above the transition zone, with smaller purely dendritic growths nearby. D and E are taken from the transition zone, and F is taken from the lower, more crystalline interior. These show the plagioclase, augite and olivine textures common towards the lower, crystalline zone. In F, the swallowtail morphologies of the plagioclase crystals are seen, as is the dendritic augite growth around the plagioclase crystals. A-C are located towards the top of the transition zone, whilst D-F are located in the lower transition zone and crystalline interior of the sample.

4.5 Plagioclase in BGP

Many of the plagioclase crystals in BGP have swallowtail morphologies (Figure 22F). Some crystals appear to have grown as tabular, with some skeletal and swallowtail-like growth protruding from the crystal corners (Figure 22D and E). These growths occur in the corners since that is where there is a larger volume of melt in contact with the crystal to draw components from (Oze and Winter, 2005). Figure 22F shows plagioclase crystals which have grown with an increasingly skeletal swallowtail morphology. It is likely that the more diffusion-limited growth seen in the BGP can be attributed to new growth of plagioclase, whilst the more tabular morphologies of the phenocrysts are likely grown prior to eruption. Plagioclase, as with the other phases, becomes more abundant with depth into the sample. A selection of representative images taken from a thin section of the upper ~3cm of a BGP sample were used to analyse plagioclase size and shape. Figures 23A-C show histograms for aspect ratio, length and width data for 200 plagioclase crystals. Of the crystals measured from SEM data, the mean length and width was 0.075 ±0.014 mm and 0.008±0.002 mm, respectively. The modal length and widths were 0.06±0.014 mm and 0.006±0.002 mm, respectively. The modal aspect ratio was 9, with a clear peak, as seen in the graph below.

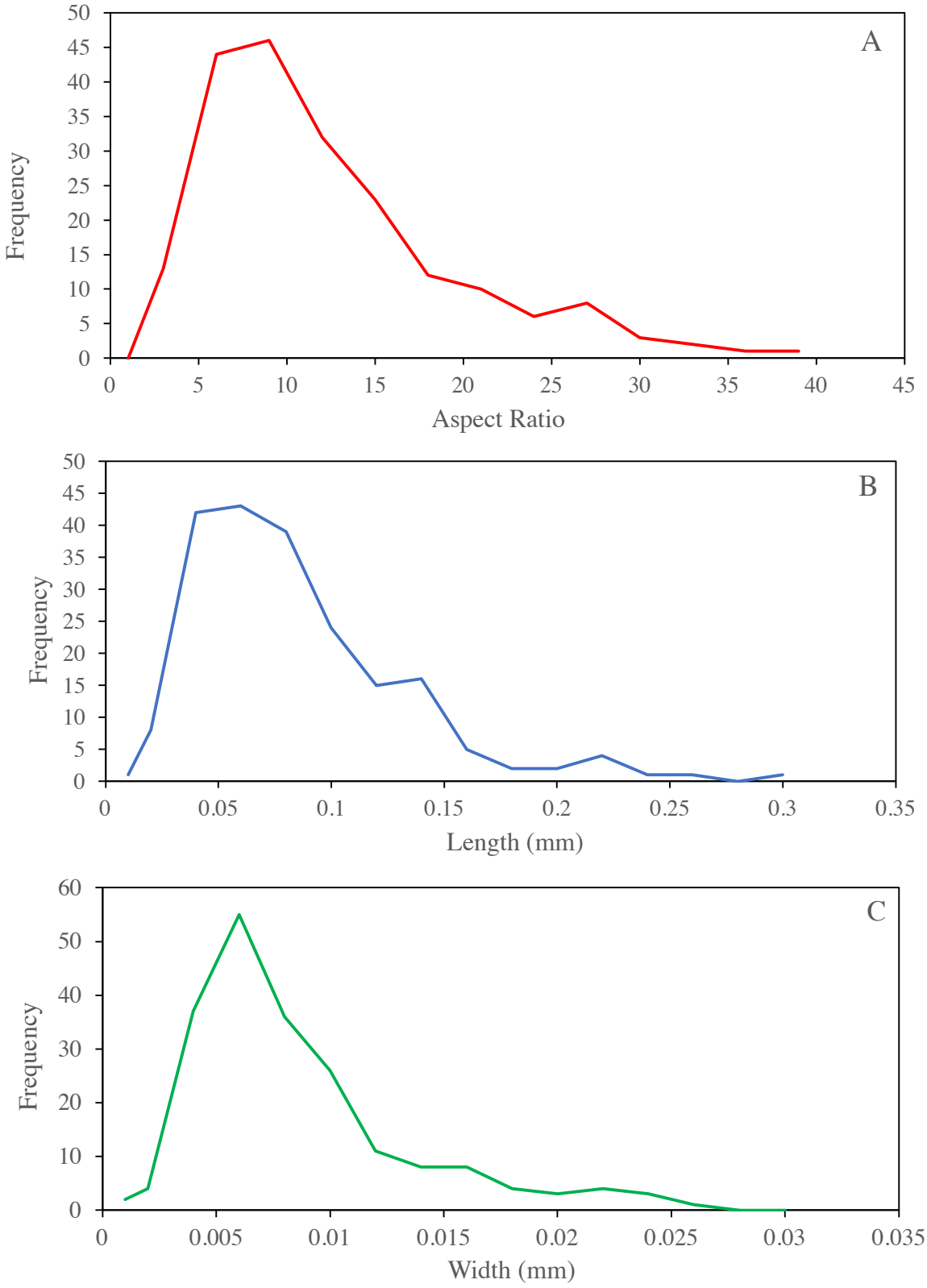

Figure 23. A-C, Frequency plots of plagioclase crystal aspect ratio (A), length(B) and width(C) from the BGP sample. Uncertainty in the length and width measurements is 1.1 μm, whilst average uncertainty in the aspect ratio measurements is 1.7.

4.6 EDS Analysis

EDS analysis was carried out on the BGP sample, on 12 plagioclase crystals and 11 zones of glass in the sample. Semi-quantitative analyses were run on selected areas using an accelerating voltage of 15 kV, live acquisition time of 30 seconds, and energy range 0-10 keV. The EDS detector was routinely calibrated using a Cobalt metal standard. The results for plagioclase crystals, and the glass in the glassy region at the top of the sample (which was the part of the sample used to make wafers for experiments) are displayed in Tables 10 and 11. The X_{An} of plagioclase varied from 49 – 65, and averaged at 60.2 for the crystals measured (n = 12, Table 10 below). The majority of crystals were anorthitic, with the exception of one crystal that had a more albitic measured composition (An_{49}).

Plagioclase	SiO_2	Al_2O_3	CaO	Na_2O	Total	X_{An}
Average (n=12)	53.9	29	12.5	4.6	100	60
Range	50.2-55.5	28.1 - 32.2	11.1 - 13.4	4.0 - 6.1	-	49 - 65

Table 10. EDS analysis results for BGP plagioclase crystals towards the top of the sample.

Glass	SiO2	TiO_2	Al_2O_3	Fe_2O_3	MgO	CaO	Na_2O	Total
Average (n=11)	56.2	1.8	14.9	6.9	7.2	9.8	3.1	99.9
Range	55.3 - 57.8	1.5 - 2.0	14.6 - 15.5	5.4 - 8.0	6.9 - 7.6	8.9 - 10.3	2.8 - 3.6	-

Table 11. EDS analysis results for BGP glass towards the top of the sample.

The BGP has an overall composition typical of a Hawaiian tholeiites, and there is no major distinguishing difference between BGP and other Kilauean basalts (Oze and Winters, 2005). Using the BGP as a starting material, which has been fully characterised using a similar methodology as was applied to the experimental samples, was useful since we were able to predict the behaviour of the melt during experiments (see Chapter 3) and also to make comparisons between the chemistry, crystal growth and textures seen in the natural lava flows with the samples produced from experimental runs (Chapter 6).

5. Experimental Results

5.1 General Experimental Observations

Each of the experiments followed a similar sequence of events that was consistent across each run. Samples were blackened on their surfaces during heating, at around 850°C, before eventually melting and coalescing into a domed droplet shape at 1150-1180°C. Whilst being held at the highest temperature of each run, the sample bubbled as any volatiles that were in the glass were released. Most samples were clear of bubbles after 3-5 minutes held at 1180°C. The first observed crystallising phase started to appear during cooling between 1180°C and 1160°C, with slight variation across different runs. Oxide growth began at 1180-1170°C in all experiments and obscured much of the main body of the sample, becoming a more significant issue as the sample was cooled to 1160°C. Growth of oxides darkened the sample and obscured growing plagioclase crystals. In most cases, the plagioclase crystals were easiest to observe nearer to the edges of the sample. This is because the edges of the droplet of melt were the thinnest areas and therefore the clearest. There was also generally less surface oxidation near the edges of the sample (Figure 24), although the very edges also had a thin line of oxides around them. In later experimental runs, this effect was taken advantage of and imaging was focussed on the areas closer to the edges of the sample, allowing better observation of growth. Upon reaching 1160°C during cooling in all runs, the majority of the sample had become covered with a surface layer of oxides which obscured much of the sample. The samples were rapidly quenched by withdrawing the sample from the furnace, to room temperature at the end of each run, and became further blackened by oxides at the surface upon this final cooling. Overviews of the full samples and a video of run 6 are available in the supplementary material. Figure 25 at the end of this section has low-resolution versions of all sample maps.

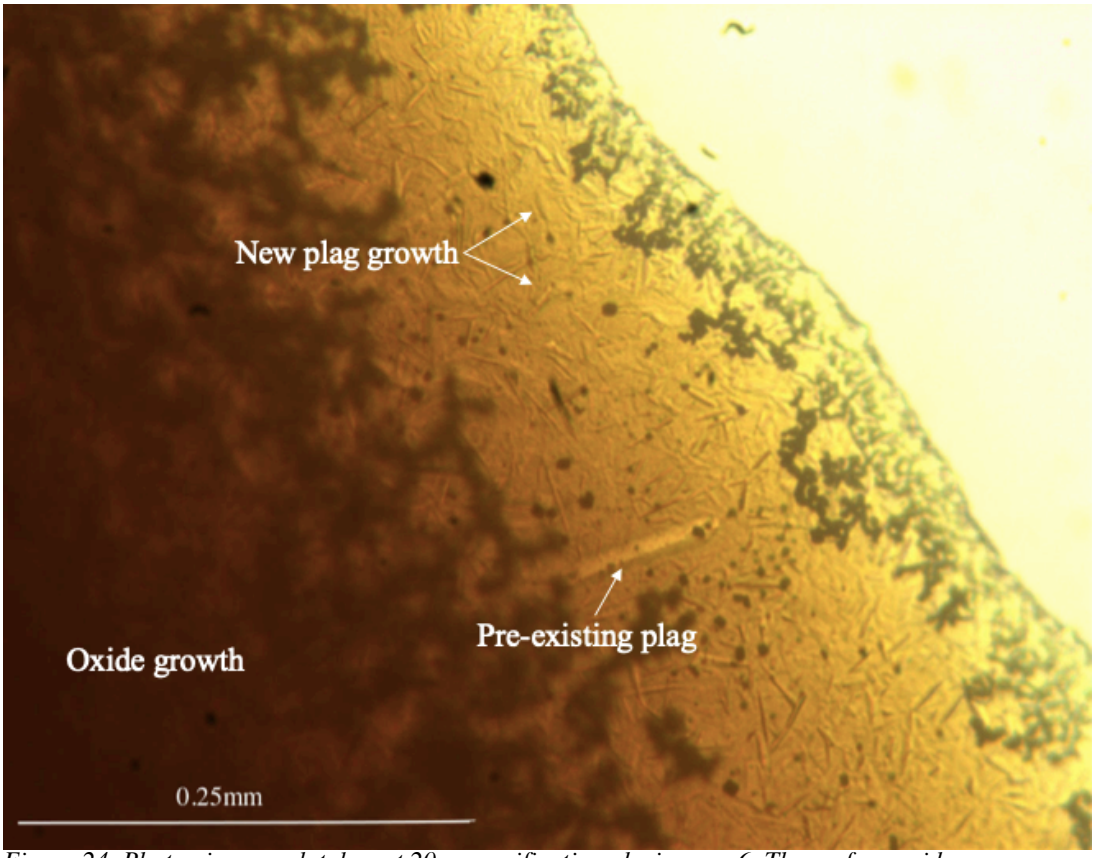

Figure 24. Photomicrograph taken at 20x magnification, during run 6. The surface oxide cover can be seen, as well as that of the edges, but there was a window of low oxide cover, allowing growing crystals to be observed.

Table 12 below summarises the general observations made that were consistent across all experimental runs.

Temperature (°C)	**Observations**
850 – 950 (during heating)	Blackening of sample until very dark and opaque.
1150-1180 (during heating)	Sample melts enough to form into a droplet and clarifies as opaque oxides melt
1180 (holding at temperature)	Minor bubbling and outgassing of sample. Bubbling generally abated after 3-5 minutes at this temperature.
1170 – 1160 (during cooling)	Apparent start of new plagioclase crystallisation.
1160 (during cooling)	Significant growth of oxide crystals, often obscuring much of the sample.

Table 12. Experimental run observations that were consistent across all runs.

All experimental runs resulted in the growth of new plagioclase crystals from melt, as well as oxides, and clinopyroxene in runs 1, 2, 5, 6, and 7. Surprisingly, experiments 3 and 4 did not result in clinopyroxene growth. Table 13 and 14 outlines the observed new growth phases for

each run. These phases were confirmed using SEM imaging. The Blue Glassy Pahoehoe starting material contains sparse larger crystals so all prepared wafers had one or two larger pre-existing crystals, often plagioclase and olivine (seen in sample maps in supplementary materials). These crystals partially melted back into the melt during heating and there was some visible new growth of these crystals during cooling, though it was difficult to measure since these crystals were often in the more obscured, central parts of the sample.

During all experiments, in the early stages of melting while the sample was mostly molten (around 1180-1165ºC), the crystals shifted around slightly (<1mm travelled), and some surface oxides were observed to shift across the surface. Once samples had reached 1150°C there was very little movement within the sample, with movement only seen in the oxides on the surface.

Run	**Phases grown**
1	Oxides, Plagioclase, Clinopyroxene
2	Oxides, Plagioclase, Clinopyroxene
3	Oxides, Plagioclase
4	Oxides, Plagioclase
5	Oxides, Plagioclase, Clinopyroxene
6	Oxides, Plagioclase, Clinopyroxene
7	Oxides, Plagioclase, Clinopyroxene.

Table 13. Minerals grown from each experiment, in order of nucleation.

Sample	**Average Cooling Rate (ºC/min)**	**Phases Crystallised (%)**			**Mean Plag Length (mm)**	**Mean Plag Width (mm)**
		Plag	Cpx	Oxides		
1	1.7	14	1	0.9	0.05	0.004
2	0.63	2 - 7	0.001	0.1	0.02	0.004
3	1	6.7	0	1.5	0.03	0.002
4	1.4	6.6	0	1	0.03	0.003
5	1	13.9	11.8	1.8	0.02	0.003
6	0.1	7.3	0.3	0.8	0.02	0.003
7	0.5	12.2	1.6	1.3	0.01	0.002

Table 14. Summary of crystallised phases. The uncertainty in measurements of % crystallinity is 0.5%

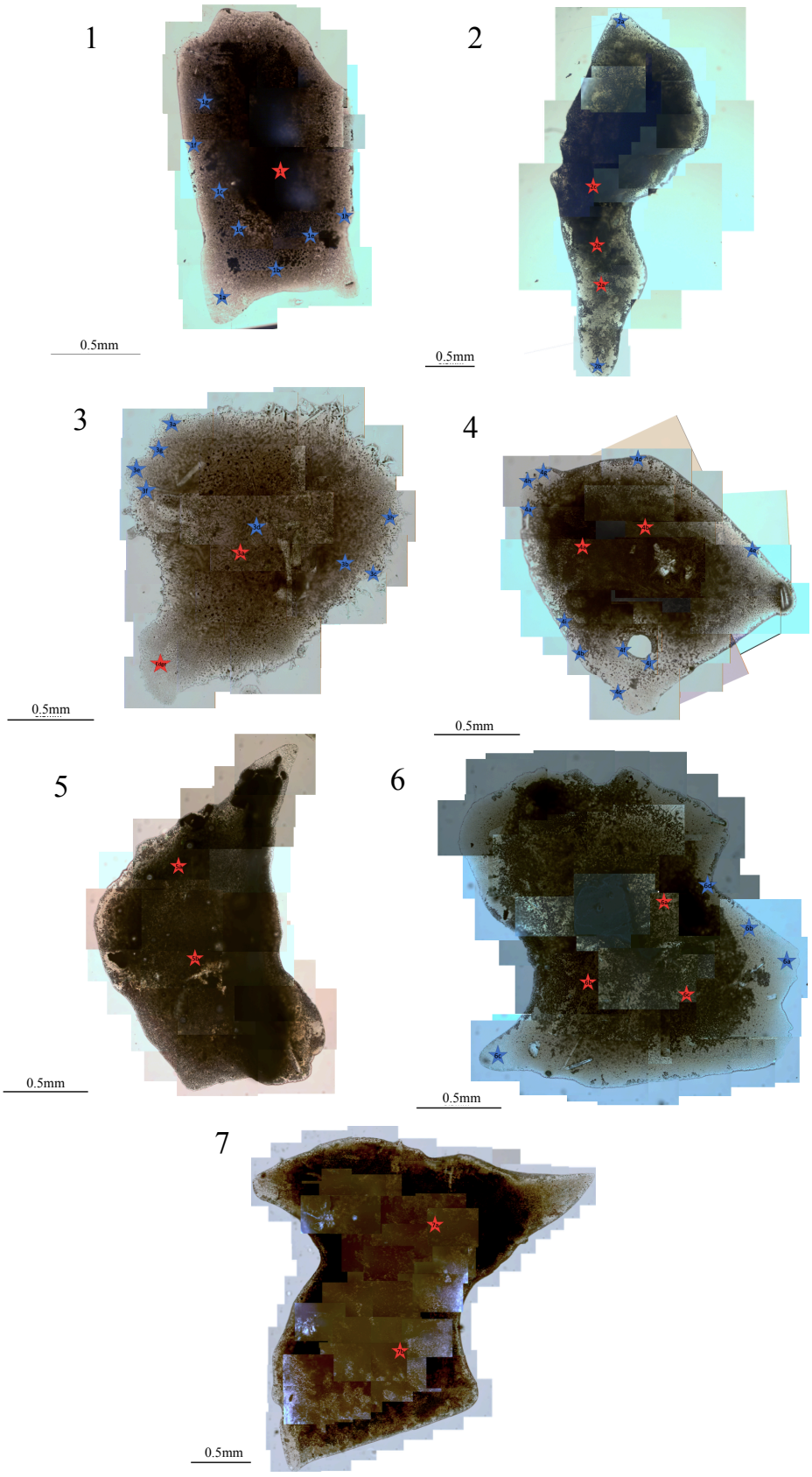

Figure 25. Low-res versions of the sample maps. Blue stars indicate centres of SEM imaging, and red stars indicate centres of optical microscope imaging

Halos

During a few of the experiments (runs 2, 3, 5 and 6) a phenomenon was observed during early stages of the run, where an ordering of the crystals was observed with halos of space forming around large, central oxide crystals. Smaller oxides were organised in a regularly spaced ordering around these 'halos'. There was evidence of these halos in the quenched sample from run 5 seen in an optical microscope and in SEM images taken after the run (Figure 26a-d). In some parts of the samples, the areas of haloed oxides lost the haloing effect and the spaces became filled with small oxide crystals. Even though they were only observed directly in 3 of the experiments, it is possible that this halo effect occurred in every run.

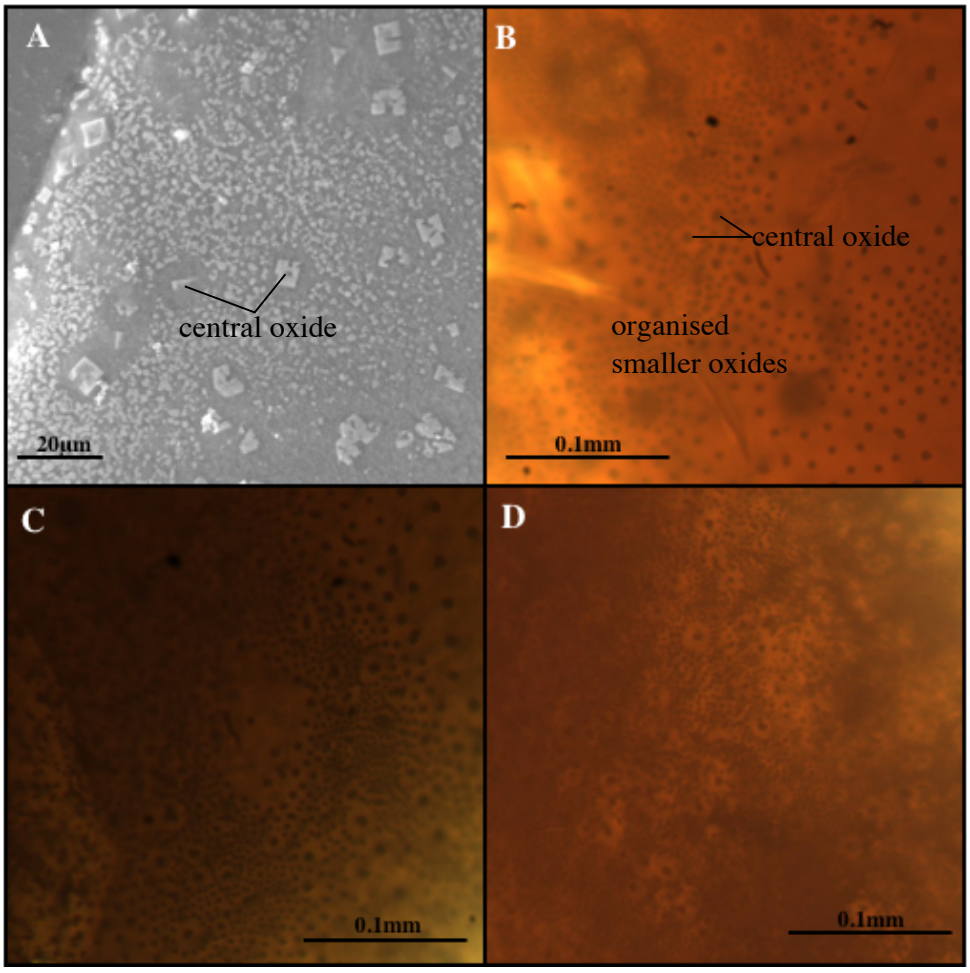

Figure 26A is a secondary electron SEM image of oxide halos preserved after quenching, on sample 5's surface, close to the edge of the sample. B, C, D are images from the heating stage microscope during experimental runs of halos forming on the sample surface during runs 3,6 and 2.

These halos moved across the sample and changing of the focal depth of the microscope objective allowed the rest of the sample to be seen below them. The halos were not visible in the polished sections of sample, so must have formed on the surface of the sample only. This phenomenon was not consistent across the whole sample, and often was only seen in one or two zones (which were around 0.1-0.3 mm across). Once the halos formed around the oxides, they were sustained as the central oxide crystal shifted across the sample surface. Crystals were not observed moving in or out of the core of a halo. The halos were not all perfect circles, and in some cases two halos combined to form an 8-shape.

The halos' widths were measured using ImageJ from photomicrographs taken during the second experimental run and were seen to change over time.

Figure 27 shows measurements for halos occurring in a specific 2x2mm area of the sample from run 2, where halos were first observed; these measurements were taken over a 6-minute period where the halos were the focus of the imaging. The images used for measurement were taken at 9, 11 and 15 minutes from onset of cooling below 1180°C. During this time, at first the halo diameters maintained the same modal size but the spread of sizes started to increase. The halos then decreased in size, as seen by the frequency plot shifting to the smaller sizes. This is consistent with observations made during the experiment - halos, during this period of observation, appeared to grow a little and then shrink over time. The size of the central oxide crystal did not change over the few minutes that they were observed (within error). The halos were not observed for extended periods of time since they were not the focus of these experiments.

In addition to this, during the experiments, it was possible to observe the motion of crystals in and through the sample. It appeared that while the crystals were held at 1180-1160°C there was visible upwelling and down-welling of oxides in some areas of the sample, which could be indicative of tiny convection currents in the sample. This convection may have been caused by

surface tension effects similar to those possibly causing the halos. As this was only a surface effect and not spread across the whole sample, it is unlikely that this had an effect on the growth of crystals within the interior of the sample, or in areas with low oxide growth. It is possible that the cause of these halos forming was related to the Marangoni effect, where surface tension differences can cause particles to move outwards from a central point (Maillard et al., 2000).

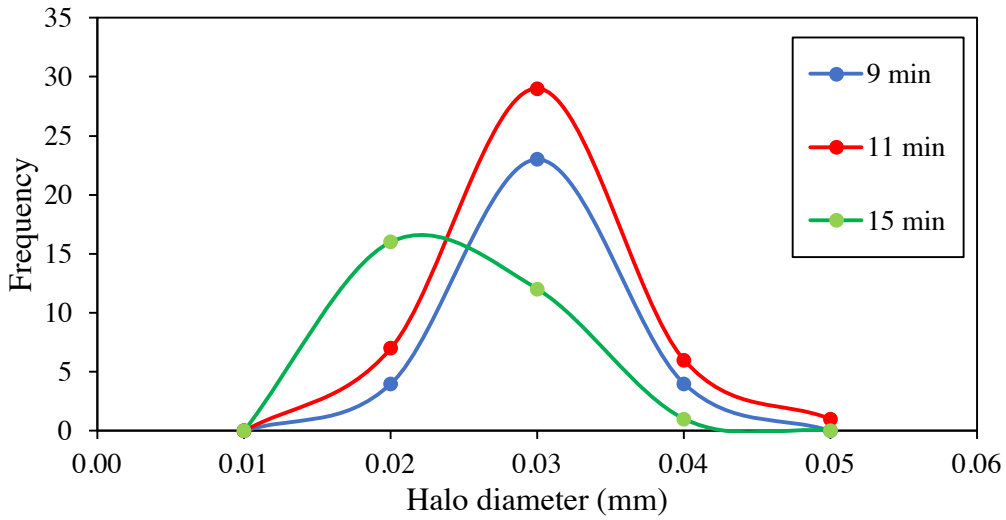

Figure 27. Frequency diagram of halo diameters, indicating that they decreased over time. The uncertainty on an individual measurement was 1 μm.

5.2 Crystal Morphology

5.2.1 Description of Phases - Overview

Overall textures

Most of the total sample volume transitioned to glass when quenched, with crystals suspended within it. The spatial distribution of crystals was relatively even throughout the samples. In the quenched samples, plagioclase crystals were often impinged on one another (shown in figures below). Where there was a large pre-existing crystal (usually plagioclase, clinopyroxene or olivine), there was growth of new crystals around the edges of that crystal. The polished samples had a thickness of 80-110μm, crystal lengths never significantly exceeded this size. It seems unlikely that proximity to the surface has substantially influenced crystal growth.

Plagioclase Feldspar

Plagioclase crystals varied in morphology from elongated acicular crystals to shorter tabular forms. Acicular crystals are defined here as very elongated (2D aspect ratio higher than 10), needle- like crystals, whilst tabular crystals are defined as rectangular (in 2D) shaped crystals with smaller aspect ratios. In experiments 1, 2, 3 and 6 hopper and swallowtail morphologies were seen, though the majority of crystals were tabular to acicular. There is a general trend of more disequilibrium morphologies such as skeletal and swallowtail crystals forming in experimental runs that had a higher cooling rate, compared to the runs with slower cooling rates, as previously demonstrated by Lofgren (1974). However, a few swallowtails were still observed in sample 6, which had the slowest cooling rate. The measureable newly grown plagioclase crystals varied from 5 – 100μm in length and 1 – 50μm in width (to 1 sf).

Plagioclase crystals appeared to most commonly nucleate homogenously from the melt, but in some cases, there was evidence of heterogeneous nucleation on top of a pre-existing larger crystal (e.g. run 6). Growth of some plagioclase crystals was inhibited by their impingement onto neighbouring crystals. In some optical microscope photographs it was also possible to see a platy texture of plagioclase, where the crystals were oriented in such a way that their largest flat sides were parallel to the flat surface of the sample (Figure 28). Plagioclase made up 6 – 15± 3% of the whole quenched product volume from experiments. Figure 29 shows representative examples of plagioclase textures that were observed from these samples.

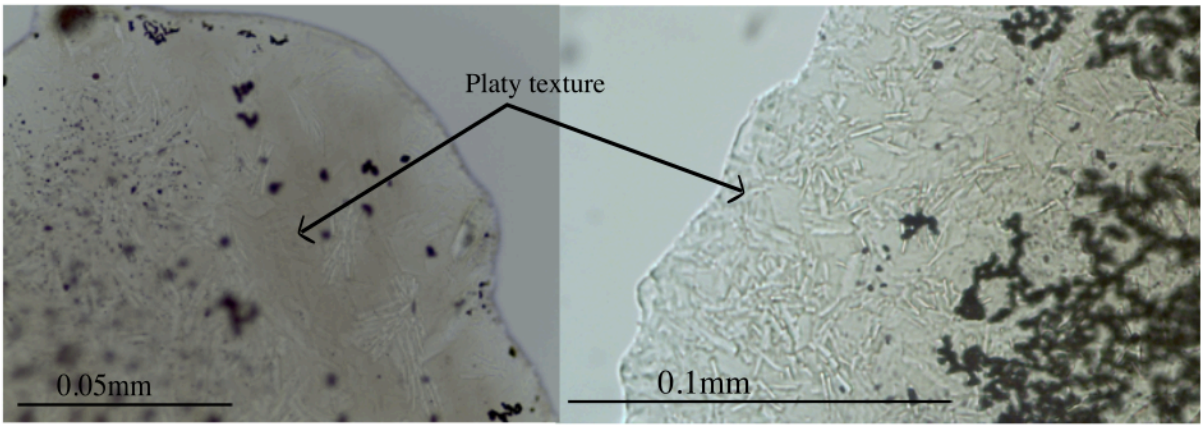

Figure 28. Photomicrographs showing the platy texture of plagioclase seen in the sample from run 4.

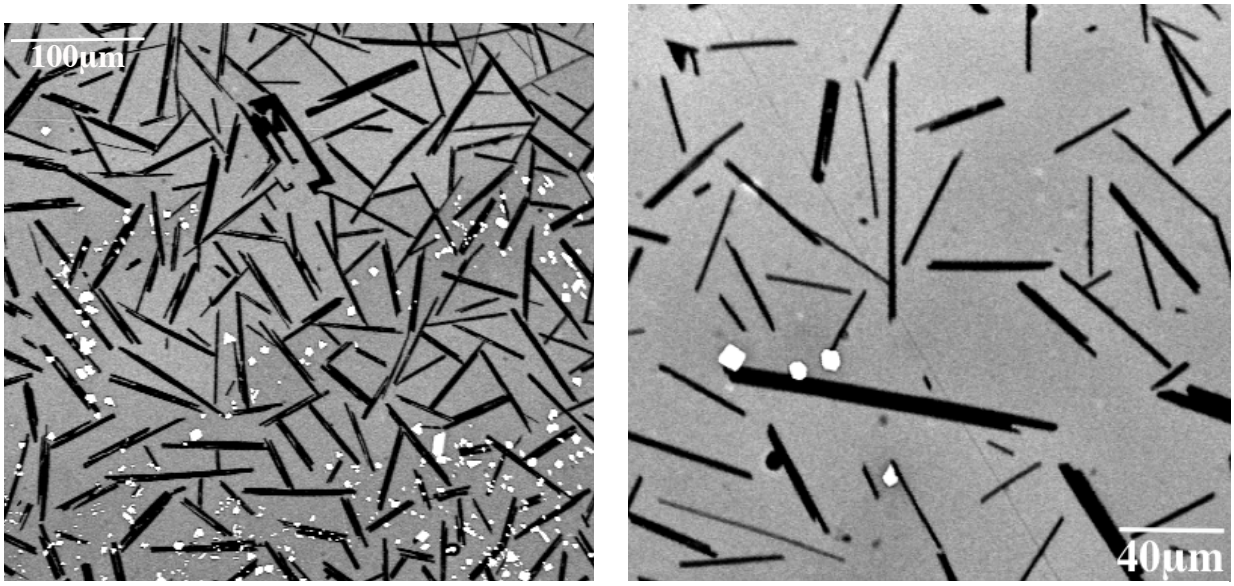

Figure 29. SEM images showing representative examples of plagioclase textures seen in experiments. Sample 1 (left) shows some hopper and swallowtail morphologies amongst more tabular crystals, and sample 3 shows more tabular, acicular crystals. Both samples show some impingement of crystals.

Clinopyroxene

Growth of new clinopyroxene crystals occurred in 5 out of the 7 experiments (see Table 13). The occurrence of this growth was not well recorded during experiments. The clinopyroxene crystals commonly show sector zoning in all samples (Figure 30a). In several of the samples, the clinopyroxene grew with a dendritic or skeletal morphology (Figure 30b). This is a similar morphology to that seen in decompression experiments in hydrous basalt of Masotta et al. (2020) and Pontesilli et al. (2019). It also appeared that the clinopyroxene crystals commonly nucleated on the plagioclase crystals that had newly grown from the melt. The concentration of clinopyroxene growth seemed to vary across the sample in all cases where it had grown. There are zones in these samples that vary from having no clinopyroxene to being almost entirely comprised of it.

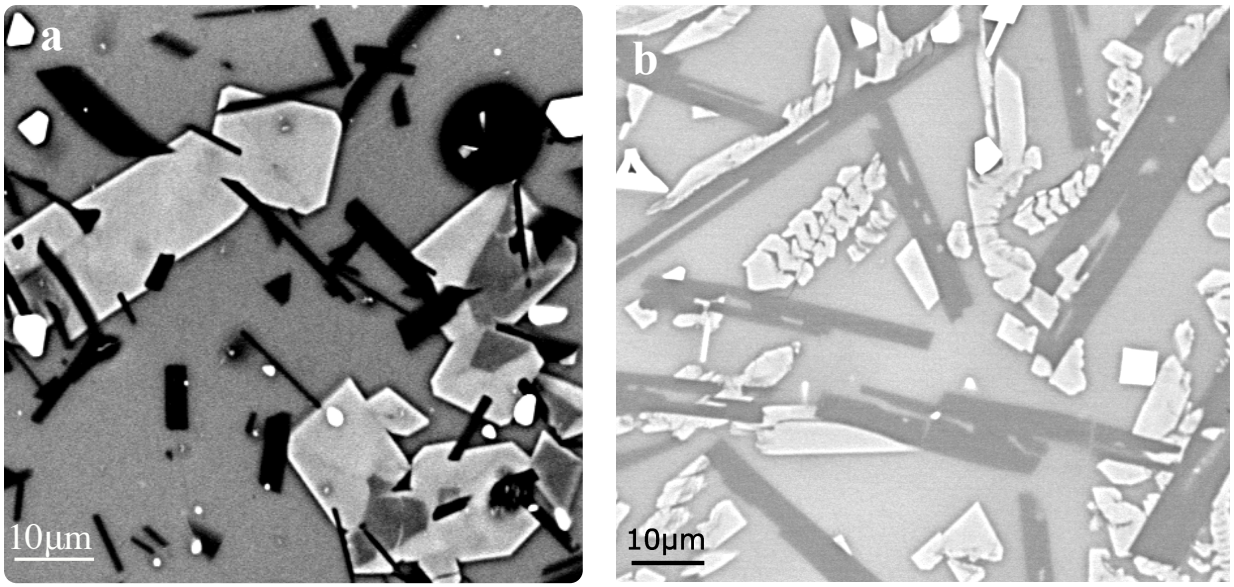

Figure 30 a-b. Photomicrographs showing examples of representative clinopyroxene textures, from sample 7 (left, more euhedral and zoned) and sample 1 (right, skeletal/dendritic, with clinopyroxene growing heterogeneously off plagioclase crystals.).

Oxides

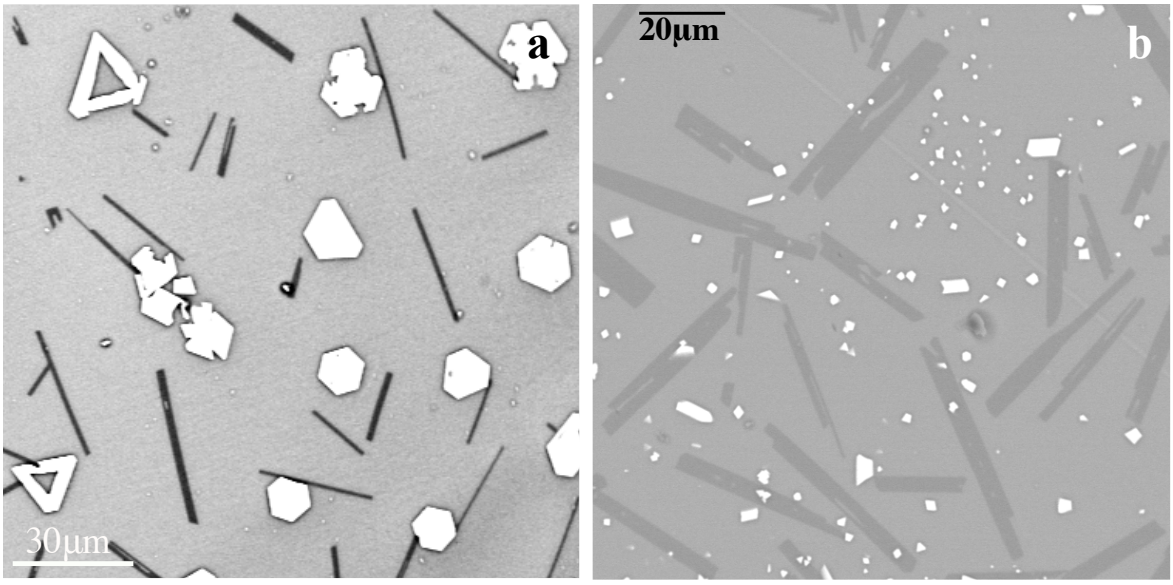

Figure 31. SEM images showing the different oxide (white) morphologies observed in experiment 3 (a) and 1 (b). In experiment 3, all oxides grew with skeletal morphologies, and were generally restricted to growing near the surface of the sample, while in run 1 the oxides grew throughout the sample and had a more euhedral shape.

The oxide crystals in each sample had similar chemical compositions and are therefore speculated to have been a single oxide phase. The oxide crystal morphology varied from skeletal to more euhedral shapes (Figure 31a-b). Experiment 3 exhibited oxide crystals with a dendritic structure (Figure 31a). Larger oxide crystals appeared to grow only at the surface of each sample, but in some cases, such as run 1, 5 and 6, smaller oxide crystals had grown throughout the sample.

Olivine

All olivine in the samples existed as a pre-existing crystal, and there was no new growth of olivine during experiments. The olivine crystals partially melted during heating and acted as a surface for heterogeneous growth. Whilst no new olivine grew, the olivine crystals did act as points on which new plagioclase and clinopyroxene nucleated (Figure 32).

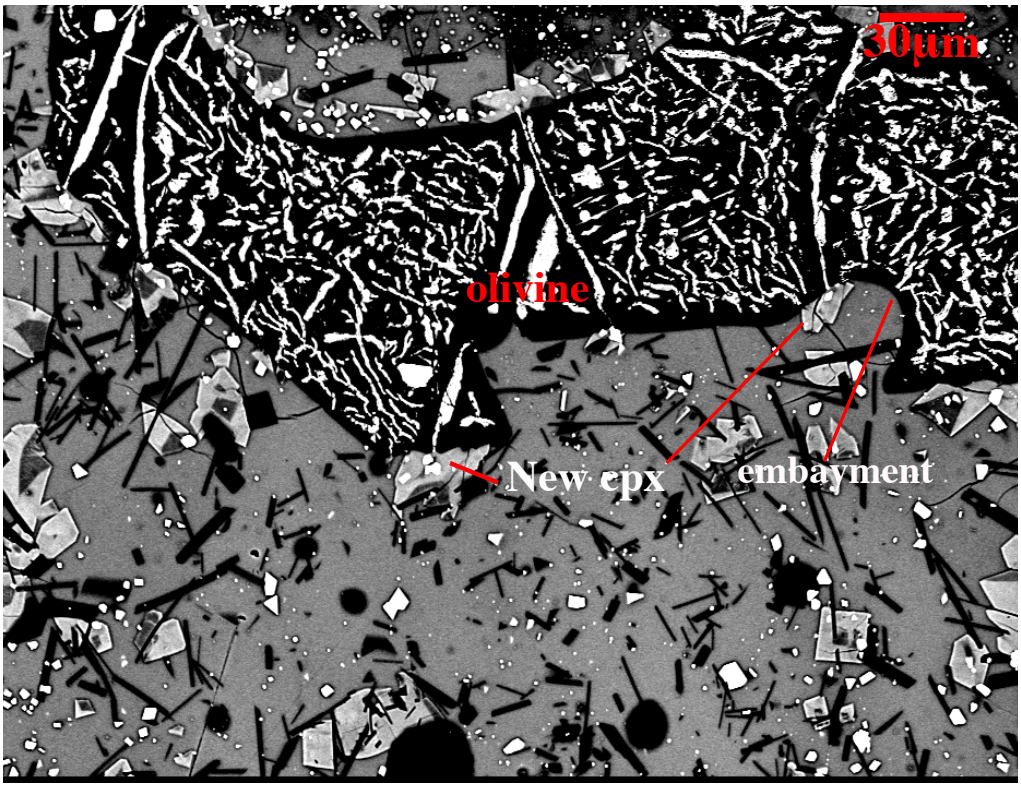

Figure 32. SEM image of sample 7, where a large olivine crystal that had been in the sample before melting shows evidence of partial melting.

5.3 Characterisation of Quenched Samples

Data on the crystal measurements taken for each of these samples, as well as all relevant images are provided in the supplementary material. Each subsection below reports the phases and textures observed for each sample, with crystallinity given in brackets.

Run 1

Cooling Rate: 1.7 °C/min (average)

Phases observed: Plagioclase (14%), Clinopyroxene (1.0%), Oxides (0.9**%)**

Description: Long, acicular plagioclase crystals were the predominant phase in this sample. Near the centre of the sample there were larger crystals, with more swallowtail and skeletal morphologies; the length and width of the plagioclase crystals decreased further away from the central larger crystal zones. This texture is shown in Figure 33, and is depicted graphically in Figures 34a-c. While it is clear that crystal length and width increased with distance from the edge, the aspect ratios of the crystals did not differ significantly with the size change, though there was a slight increase in the modal aspect ratio for the mid-size crystals. Overall, the plagioclase in this sample had a modal aspect ratio of 10 (with a standard deviation of 7.6), and an average length and width of 0.05 and 0.004mm (with standard deviation of 0.02 and 0.002). Most of the plagioclase crystals are in contact with at least one other crystal in 2D, suggesting a mostly or fully impinged framework of crystals in 3D.

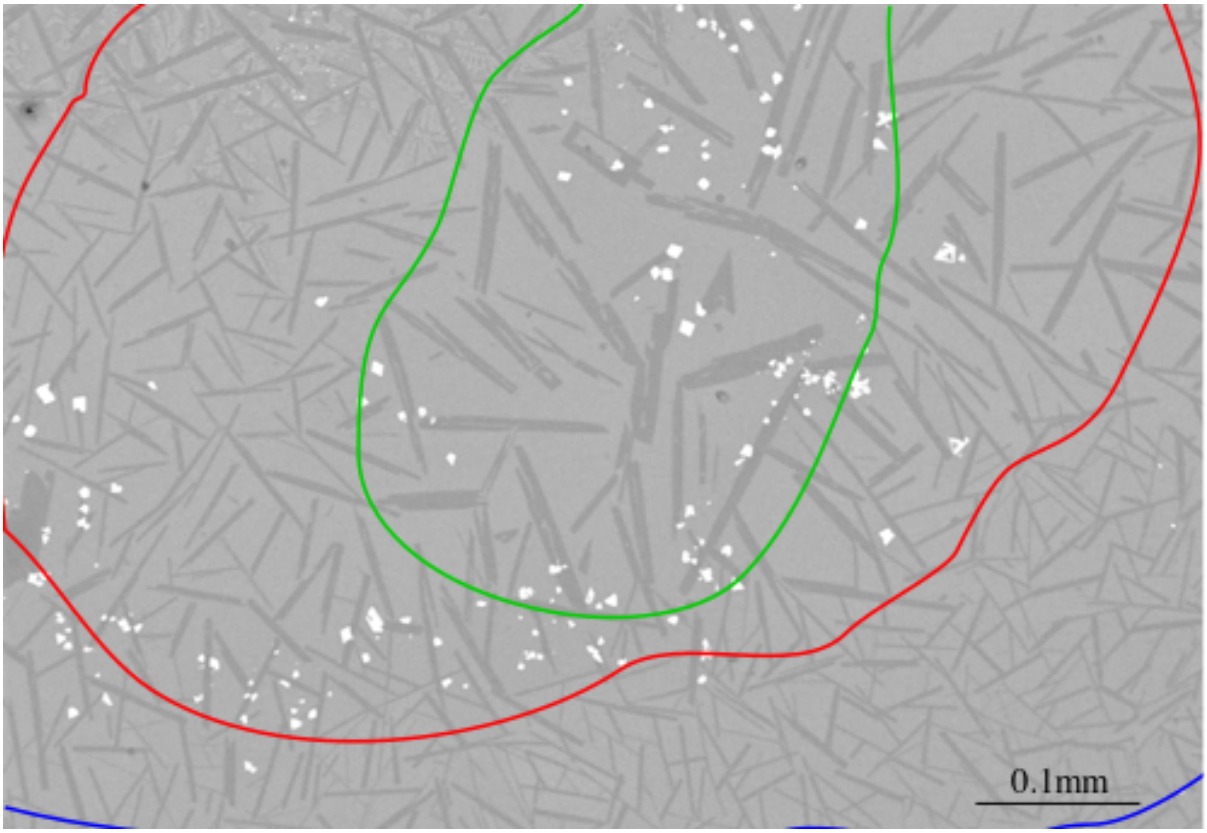

Figure 33. Backscattered electron image showing the general texture of the quenched sample after the first experimental run, with the zones used in figure 33 drawn on to outline the 3 different crystal size categories. It is possible that this variation was caused by sample thickness.

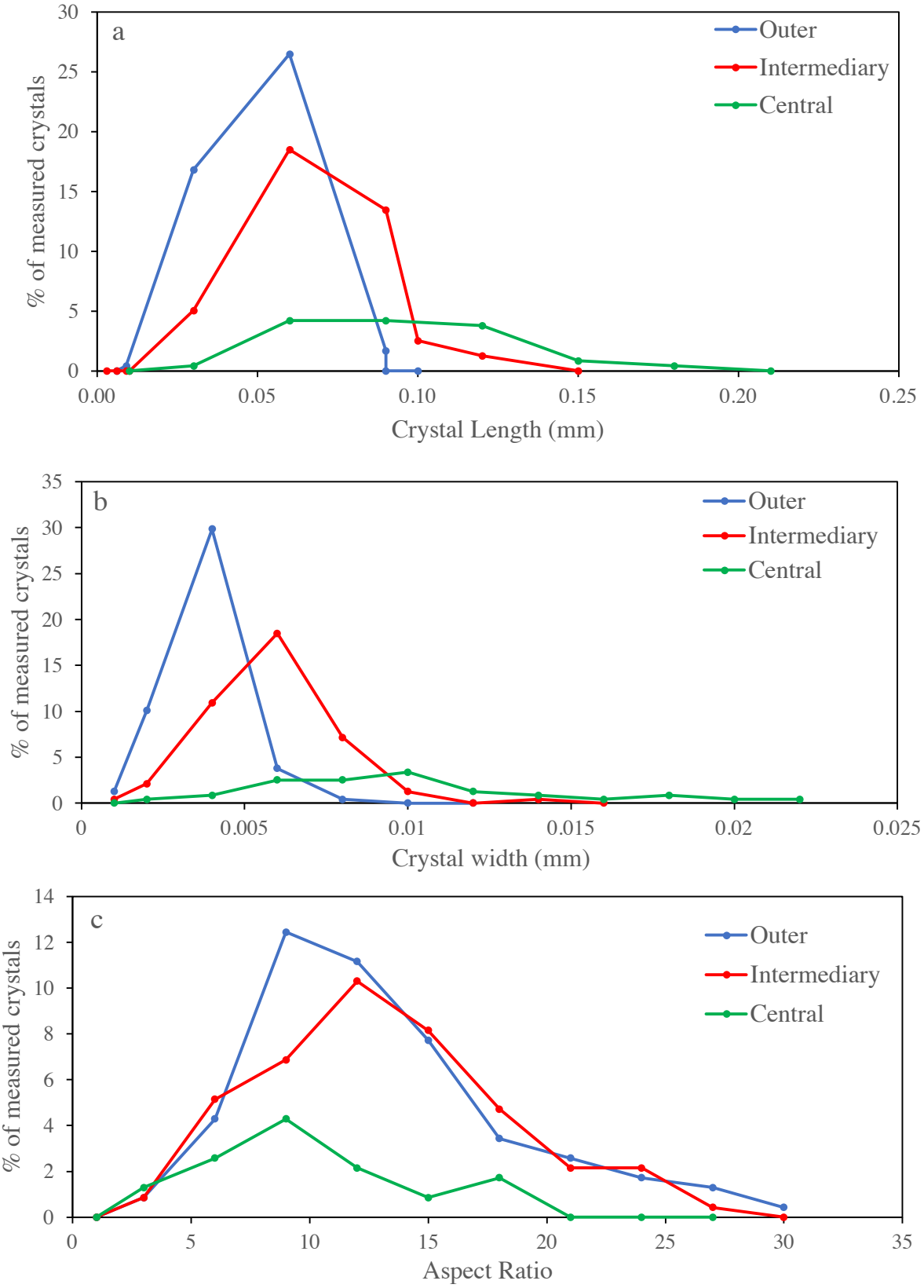

Figure 34a-c. Plots of the % of crystals a) length, b) width, c) aspect ratios; for three different concentric zones within the sample, showing how these measured quantities change with distance from the edge of the sample. The uncertainty on the length and width measurements is 1 μm, while the uncertainty in the aspect ratio measurements is 4.5.

There were patches of feather-like skeletal and dendritic clinopyroxenes that appeared to have heterogeneously nucleated onto the new plagioclase crystals (Figure 35). The growth of skeletal clinopyroxene crystals was concentrated in one area towards the centre of the sample. There were some cubic and skeletal oxide crystals scattered around the sample. A layer of oxides covered around 70% of the sample surface before polishing.

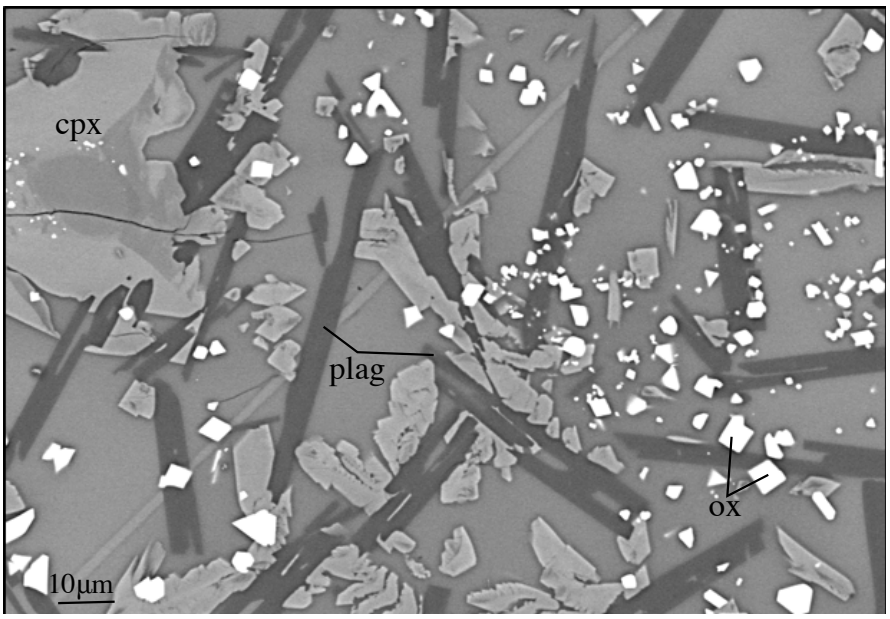

Figure 35. Backscattered electron image of clinopyroxene crystals with skeletal morphologies from the first run. Image taken in ~0.3mm wide zone in which cpx grew near centre of sample.

Run 2

Cooling Rate: 0.63 ºC/min (average)

Phases observed: Plagioclase (2-7%), Oxides (0.01%), Clinopyroxene (<0.01%)

Description: This sample formed an irregular serpentine shape upon melting, rather than a simple dome (see Figure 25). This shape may have affected the distribution of crystals by limiting their width and condensing growth into a smaller area. As the amount of plagioclase growth was so variable across the sample, a range has been given for the crystallinity. Most of the sample cooled into glass. The surface of the sample was almost entirely covered with a layer of oxides before polishing (as seen in Figure 32). The widest area of the sample had some larger (0.04-0.06mm) acicular plagioclase crystals growing from melt, with a few hopper and

swallowtail shapes. There were 5 small, skeletal clinopyroxene crystals, most seemingly unattached to any plagioclase. In the thinner 'tail' of the sample, the plagioclase crystals appeared more tabular in shape. These more tabular crystals were also visible in optical microscope images (Figure 35). The two populations of crystals are shown in Figure 37, and are plotted in Figure 38a-c. Overall, the modal 2D aspect ratio of plagioclase in this sample was 9.0, with a mean of 7.4 and standard deviation of 3.6. The mean length and width of plagioclase crystals was 0.021mm and 0.0036mm respectively, with standard deviations of 0.018 mm and 0.003 mm. There was one large pre-existing olivine crystal in the sample, around which oxides had covered the edges, as well as some heterogeneous clinopyroxene growth.

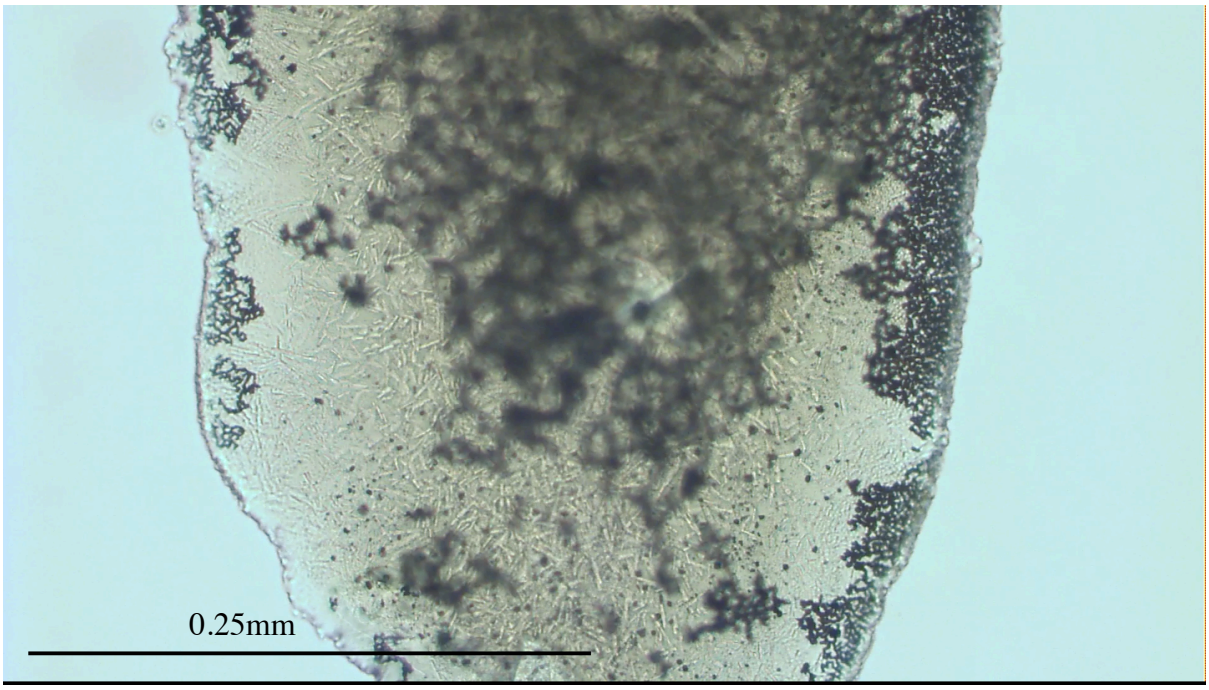

Figure 36. Photomicrograph of the 'tail' of the sample, showing a large number of tabular plagioclase crystals within. The out of focus zone on the left as it is a thicker pat of the sample. Taken after quenching.

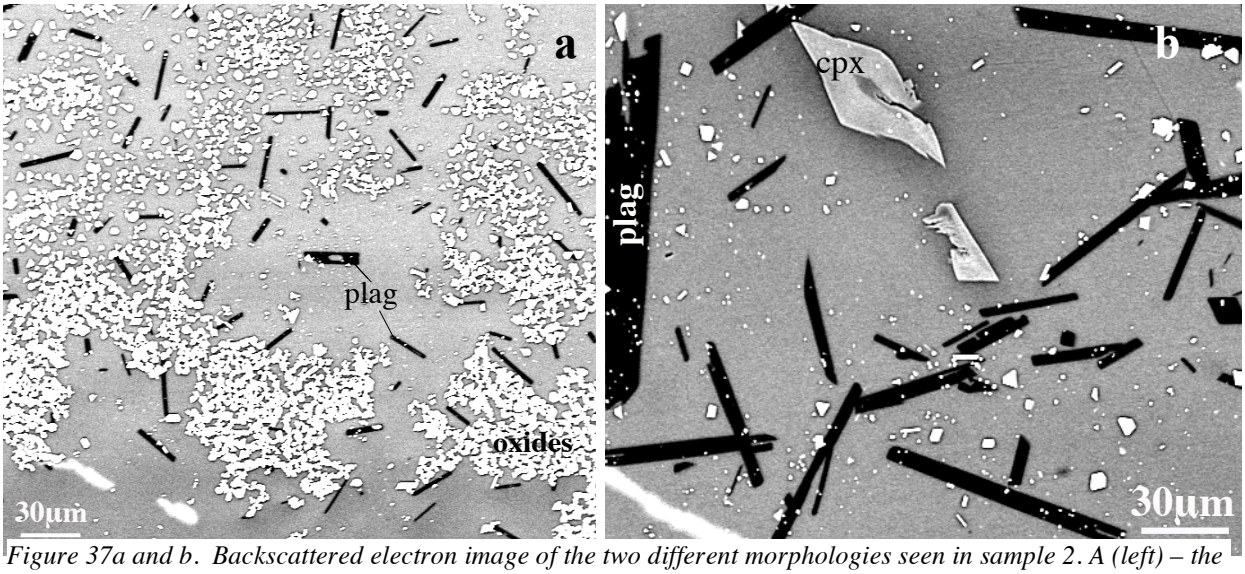

Figure 37a and b. Backscattered electron image of the two different morphologies seen in sample 2. A (left) – the smaller, more tabular crystals; B(right) – the larger crystals with swallowtail shapes; Cpx growing on a plagioclase crystal at top of image.

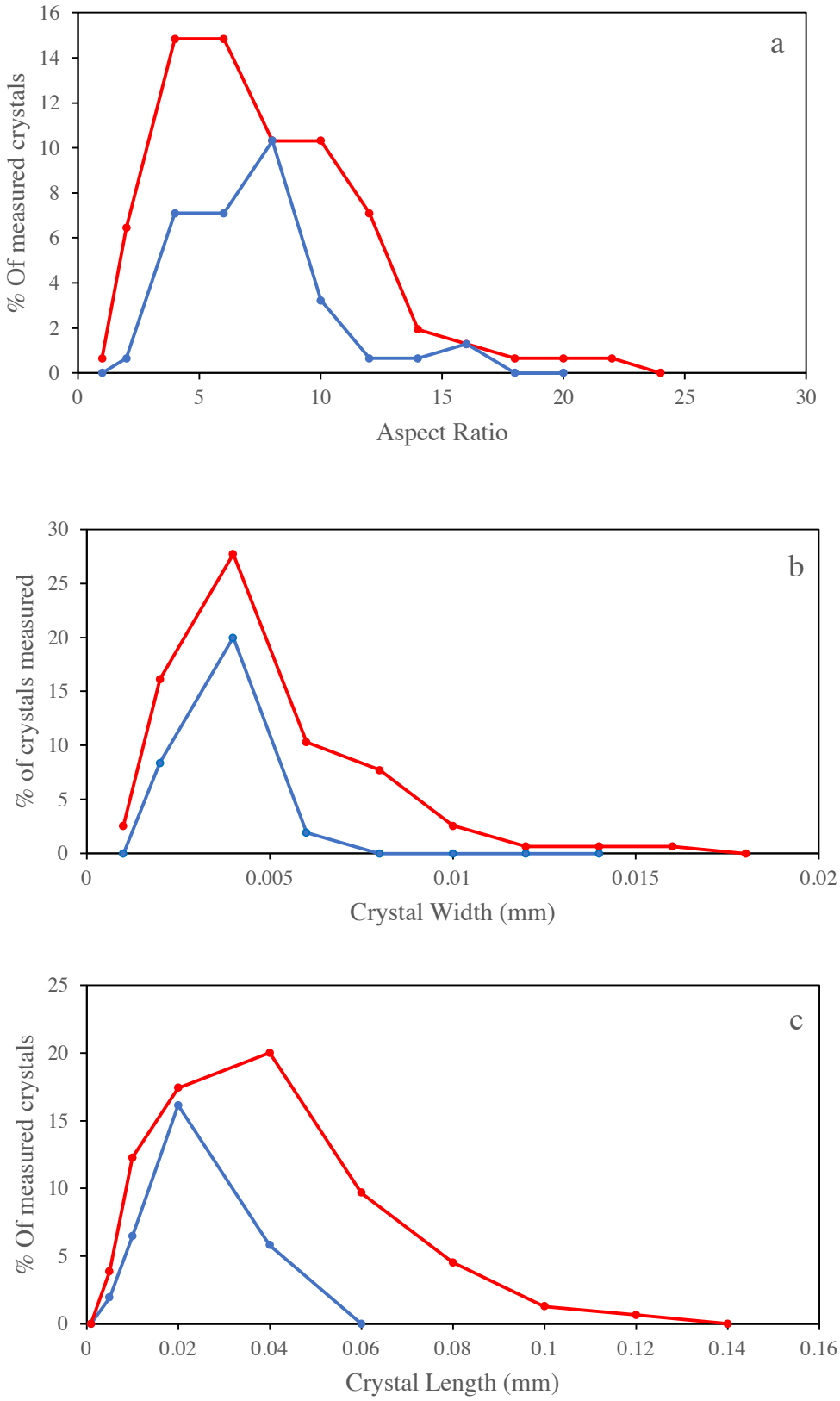

Figure 38a – c. Plots showing the differences between the larger (red) and smaller (blue) populations of plagioclase crystals. The uncertainty in the length and width measurements is 1 μm, whilst the uncertainty in the aspect ratios is 2.

Run 3

Cooling Rate: 1°C/min (average)

Phases observed: Plagioclase (6.7%), Oxides (1.5%)

Description: During the third experimental run, crystals were observed to grow outwards from the limits of the sample, and crystal growth created a variety of feather-like growth patterns at the edge of the sample (Figure 39). Figure 39 shows some examples of the different crystal morphologies seen on the edges of this sample, displaying dendritic growth and intergrowth of phases. Regular plagioclase growth also occurred near to the edges and in the rest of the sample. These irregular morphologies may have been a consequence of a reaction of the sample with the sapphire slide, though these morphologies were not observed in any other run.

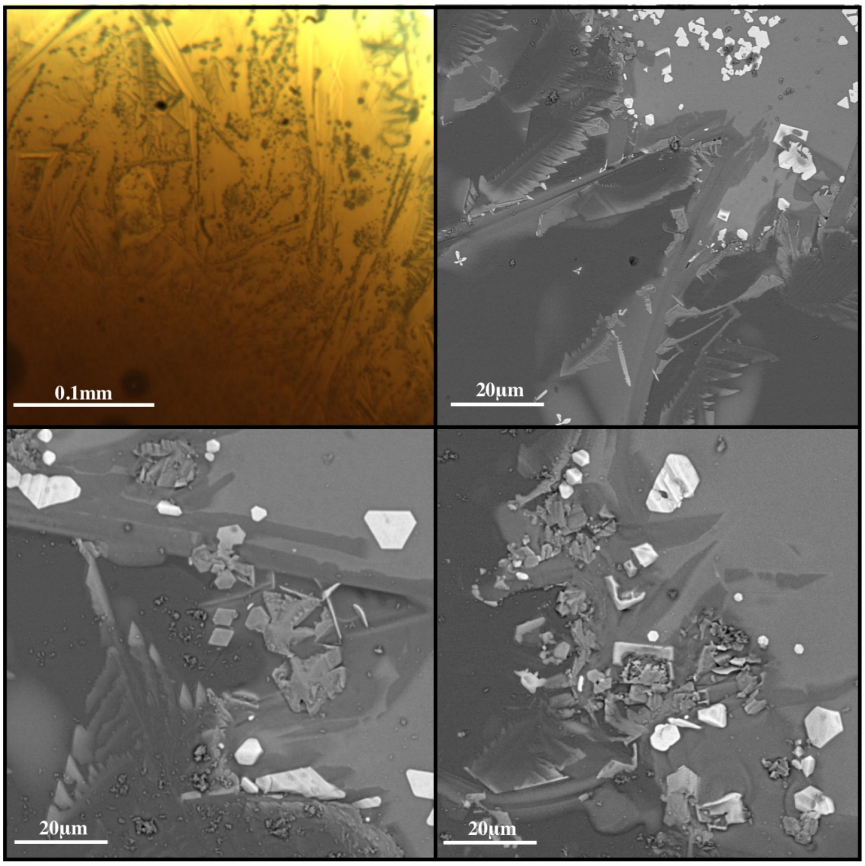

Figure 39. Top left is an image from run 3 taken while held at 1160C; the other three images are backscattered electron images taken of the edges of the sample after quenching.

Clumps of more tabular plagioclase crystals also grew in some patches at the edge. These edge crystals were measured, and were found to have an average length about half that of the rest of the sample's plagioclase and an average aspect ratio of 4.9, compared to 8.7 for the rest of the sample. This type of growth was also seen in the sample from run 6. The general internal texture of the sample included acicular-tabular plagioclase crystals, with some skeletal oxide crystals distributed throughout. There was a difference in the crystal morphologies with depth into the sample (changes occur over distances of <1mm). There were more swallowtail crystals growing towards the surface of the sample, and more tabular morphologies growing nearer to the base, but on measuring the dimensions of these crystals as discrete groups with depth into the sample, it was observed that their average aspect ratio did not vary significantly with depth, although the crystals nearer to the top of the sample were 0.01mm longer on average.

Many of the oxides in this sample had a hopper morphology (Figure 40). This sample also exhibited a pattern of decreasing crystal size with distance from the centre of the sample, similar to Run 1. No new clinopyroxene crystals were observed to grow during this experiment.

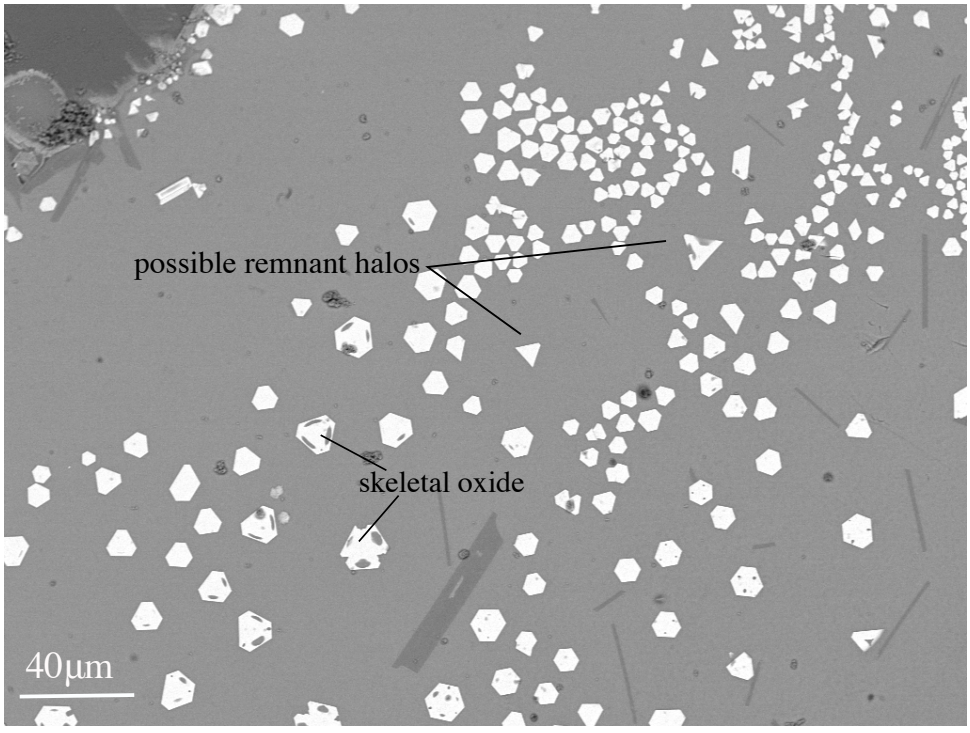

Figure 40. Skeletal oxide crystals from run 3. The organisation of the crystals here suggests they may have formed as part of the halo structures.

Run 4

Cooling Rate: 1.4 °C/min (Average)

Phases observed: Plagioclase (6.6%), Oxides (1.0%)

Description: Long tabular – acicular plagioclase crystals took up most of the new growth in this sample, with a few swallowtail ended crystals, but with most plagioclase having grown with a facetted morphology. Although it is less pronounced than in other samples, there was a general trend of plagioclase crystals appearing to become smaller with distance from the centre of the sample. There was a large cluster of plagioclase and olivine crystals in the wafer used in this experiment, around which only a few small plagioclase crystals had grown, leaving a pronounced gap (Figure 41). Oxides had also grown around the perimeter of the pre-existing crystals. Most of the plagioclase crystals in this sample appeared to show little impingement. Optical microscope images revealed that in one area of the sample, towards the edge, several clusters of small plagioclase crystals formed amongst a platy texture of the same phase (Figure 42). The crystals in these clusters had similar aspect ratios to the non-clustered plagioclase. A large hole formed in one corner of the sample during melting; it is possible that this was caused by a small amount of contamination by remaining crystal bond. No new clinopyroxene grew during this experiment.

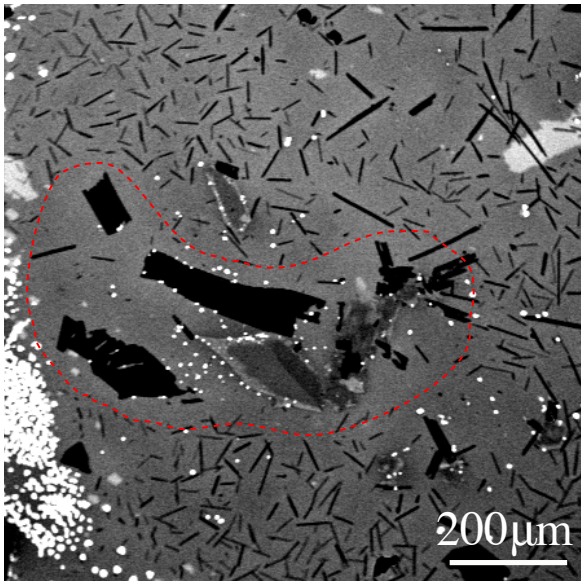

Figure 41. Image of sample 4 taken at low magnification, showing the general texture of the sample and the gap around the large pre-existing crystals (denoted by the red dashed line). A layer of oxide crystals can also be seen around this cluster, growing close to/on the larger crystals

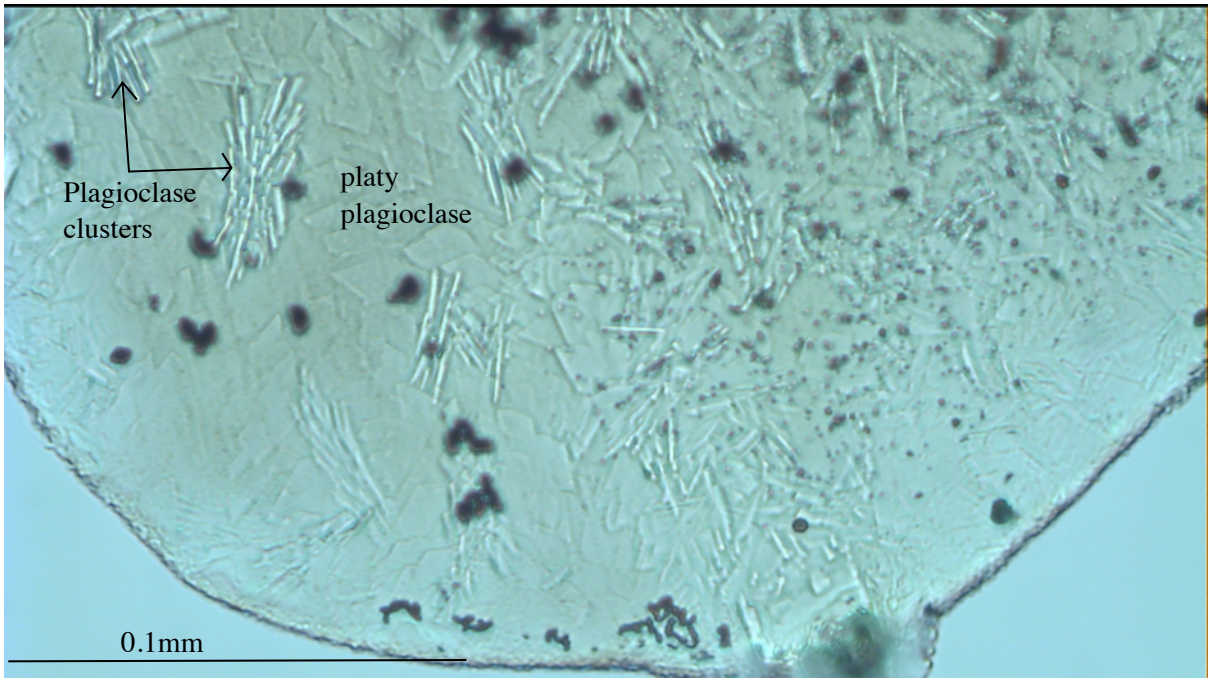

Figure 42. Clusters of plagioclase crystals amongst a platy texture near the edge of the sample. 20x magnification microscope image. The dark spots are oxide crystals on the surface.

Run 5

Cooling Rate: 1°C/min (steady)

Phases observed: Plagioclase (13.9%), Clinopyroxene (11.8%), Oxides (1.8%)

Description: This sample had a greater total crystallinity and had significantly more clinopyroxene crystals throughout, compared to previous runs. The clinopyroxene crystals were often sector zoned. There were both skeletal and regular clinopyroxene morphologies here. The plagioclase was evenly distributed throughout the sample, with no discernible pattern in size across the sample. All observed plagioclase crystals had a tabular morphology. There were patches in the sample where clumps of skeletal clinopyroxene filled the gaps between plagioclase crystals that had grown. This was not consistent through the whole sample and graded to individual, more equilibrium shapes of clinopyroxene crystals (Figure 43). Crystal number density was lower in the centre of the sample than at the edges. Small cubic oxide crystals were interspersed through the sample. The sample was almost entirely coated in a layer

of oxides before polishing, with some areas near the edge of the sample maintaining the halo structures that formed during the experiment (Figure 44).

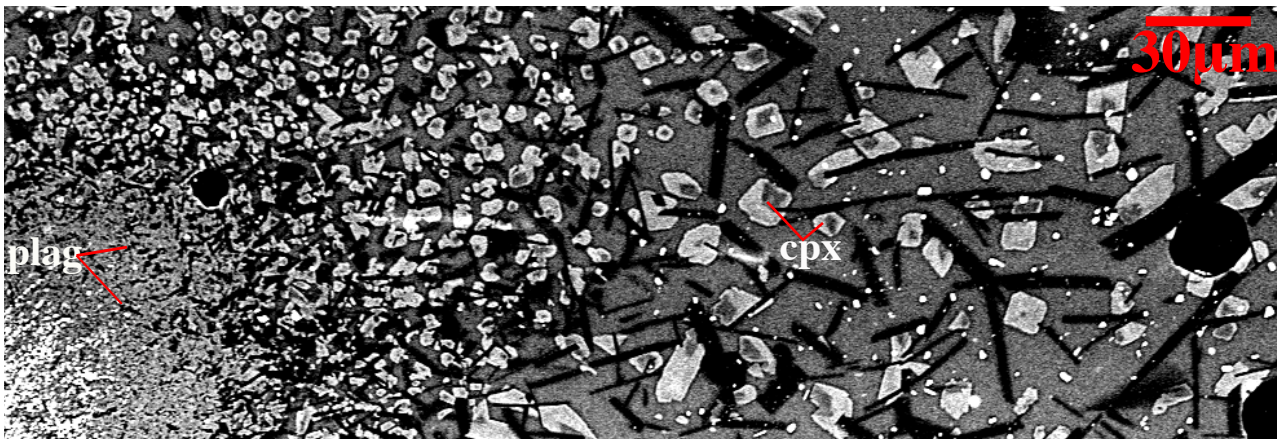

Figure 43. Section of sample 5, showing the gradient of different clinopyroxene morphologies and textures. The left side of the image is closest to the edge, and shows the clumps of skeletal clinopyroxene that filled space between plagioclase crystals, which then grades into more euhedral individual clinopyroxene crystals which display sector zoning and increase in size and spacing towards the centre of the sample (right side)

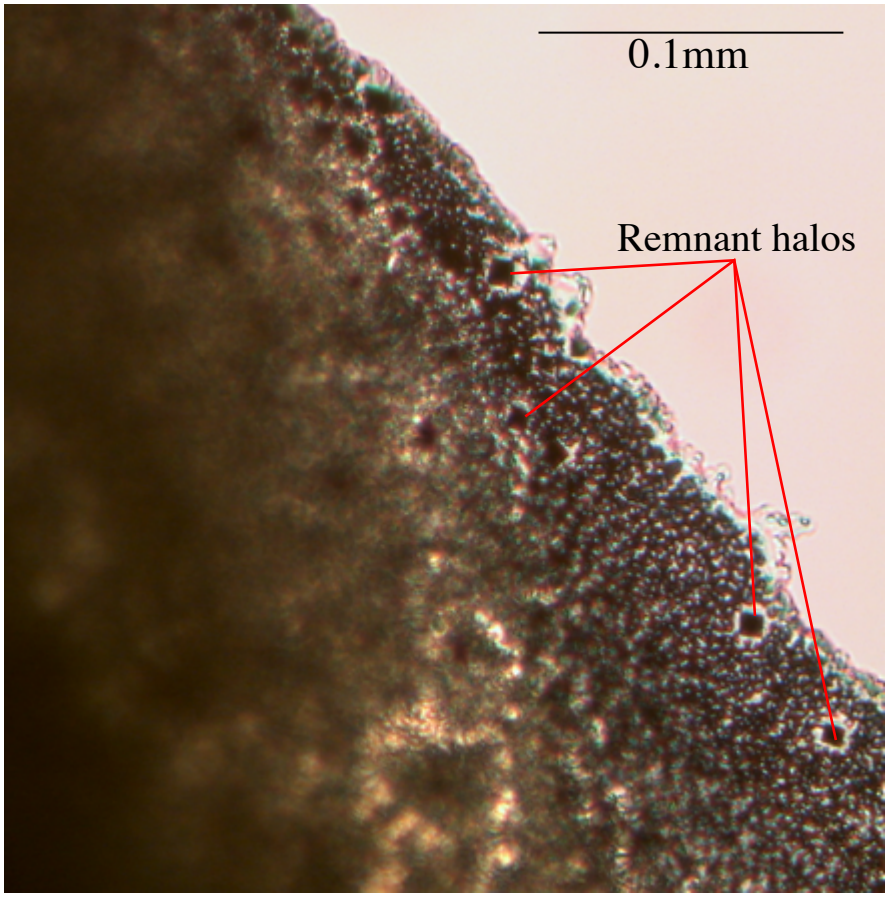

Figure 44. Optical microscope image showing the remains of the halo formations on the surface of the sample after quenching, with single large crystals in their centres, all of which have a square morphology in 2D.

Run 6

Cooling Rate: 0.1 °C/min (Steady)

Phases observed: Plagioclase (7.3%), Clinopyroxene (0.3%), Oxides (0.8%)

Description: The majority of plagioclase crystals in this sample were primarily tabular in shape, with a few larger swallow-tailed crystals. The modal aspect ratio for plagioclase crystals in this sample was 6, with no significant change in aspect ratio across the sample. Some small clinopyroxene crystals with distinct sector zoning appear to have nucleated on and near plagioclase crystals in some parts of the sample. Clinopyroxene had also grown on the edges of a large, pre-existing olivine crystal that was present in the sample (Figure 45). The clinopyroxene here tended to have a skeletal morphology. The quantity of clinopyroxene in this sample is notably significantly less than that of runs 5 and 7. Small cubic oxide crystals were evenly dispersed through the sample. There was no clear pattern of crystal size with distance from the edge of the sample, and smaller crystals were mixed in with the larger. When quenched, the majority of the surface of this sample was coated in a layer of oxides, but with enough of a window near the sample edges to observe crystals before polishing.

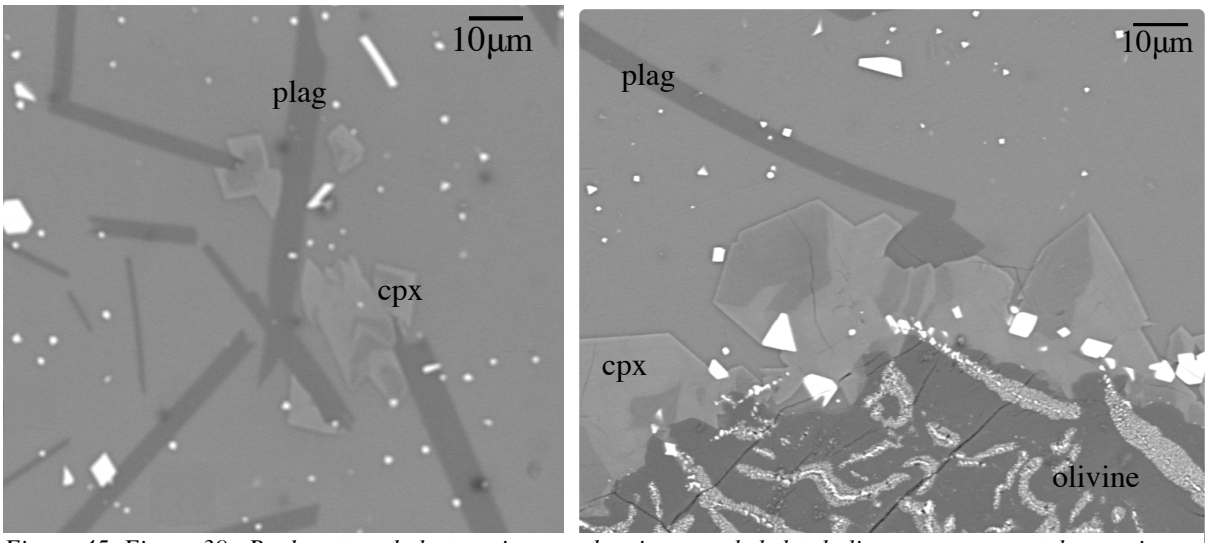

Figure 45. Figure 39. Backscattered electron images showing zoned skeletal clinopyroxene crystals growing on/near tabular plagioclase crystals (left), and clinopyroxene growing off of an olivine crystal (right).

Run 7

Cooling Rate: 0.5°C/min (steady)

Phases observed: Plagioclase (12.2%), Clinopyroxene (1.6%), Oxides (1.3%)

Description: The plagioclase crystals grown in this sample were facetted and tabular, and had a mean length of only 0.01mm, smaller than the other samples. There was no distinct pattern of size change across the sample. The modal and mean aspect ratio of the plagioclase crystals was 6 and 5.8, respectively, with a standard deviation of 3.9. Most plagioclase crystals in this sample appeared to be growing freely, occasionally impinging on each other. In some cases, clinopyroxene crystals had grown around/on the new plagioclase, and on pre-existing plagioclase crystals (Figure 46). The clinopyroxene in this sample had grown with two morphologies. In the central zone of the sample, the clinopyroxene was more regularly shaped, displaying hexagonal and octagonal sections and sector zoning (Figure 46). Towards the edges, however, there were patches of dendritic clinopyroxene that had grown, infilling gaps between plagioclase crystals.

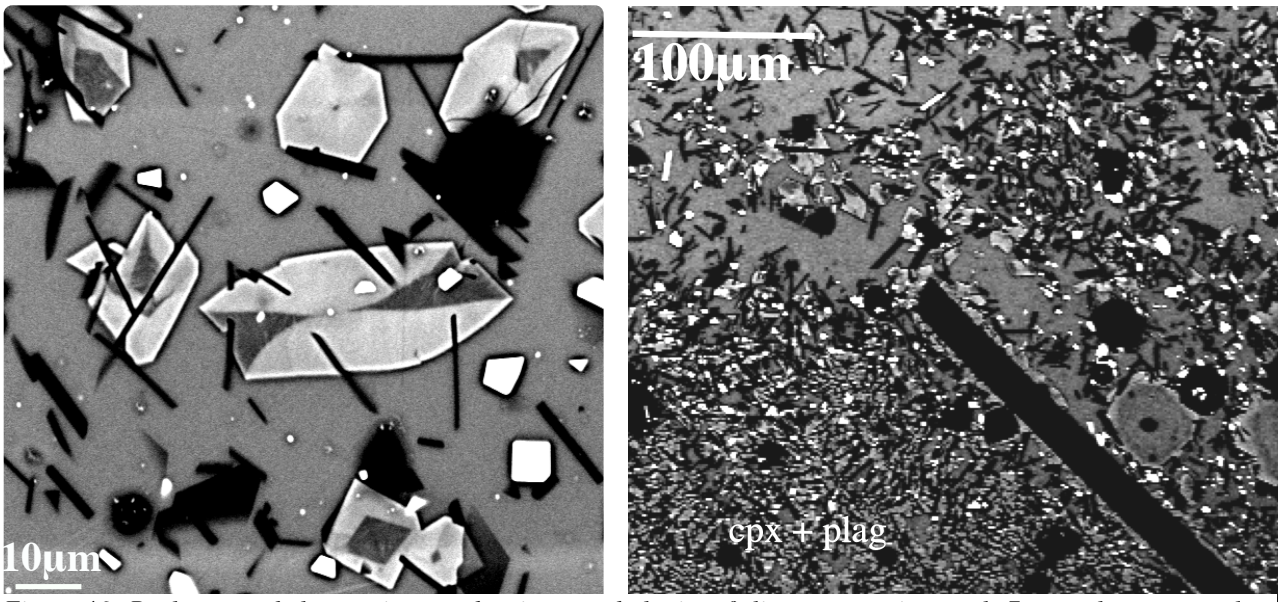

Figure 46. Backscattered electron images showing morphologies of clinopyroxene in sample 7 – regular octagonal sections (left) and dendritic (right). The image on the right also shows cpx growing around the edges of a larger pre-existing plagioclase crystal

5.4 Plagioclase Aspect Ratios

With the exception of the first and third runs, which both experienced a longer time spent above the liquidus temperature, had higher modal aspect ratios, the frequency plots of the other samples indicated modal aspect ratios around 5 – 9. These aspect ratios were measured in 2D and represent the shapes of different slices through the crystals. Frequency plots for all the aspect ratios of measured crystals in all samples are shown in Figure 47, with frequency normalised to 100 to allow comparison. These data are taken from measurements carried out on SEM images since these had the lowest uncertainty, (0.5μm for the SEM images and 1μm for the microscopes) and provided the largest datasets on crystal size. Runs 1 and 3 seem to both be shifted more to the higher end of the aspect ratios than the others; both of these samples had observably more acicular plagioclase crystals. These two experiments had different cooling rates, but both were held at higher temperatures for slightly longer than the other runs. Tables 15 and 16 further detail the aspect ratios of plagioclase crystals in each experiment. The two datasets (SEM and microscope) do not reflect data for the exact same set of crystals.

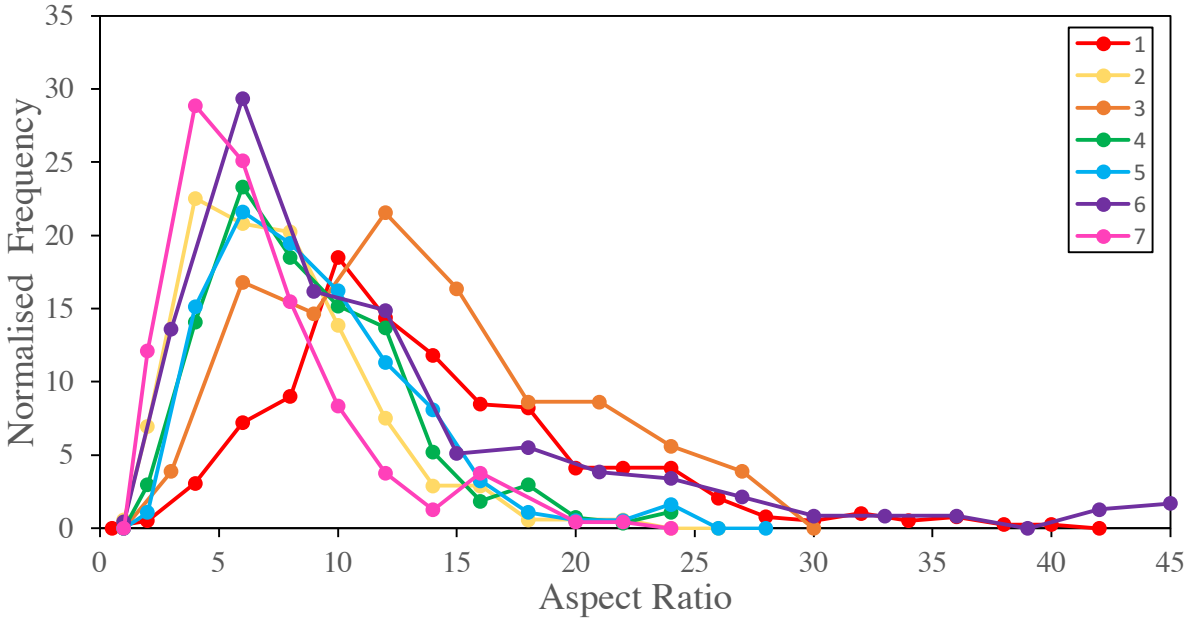

Figure 47. Frequency plots of the aspect ratios for crystal populations in each of the experimental runs, from SEM data. The number pertains to the experimental run number. Uncertainty in the aspect ratio ranges between 2.3 – 5.8.

Run	Cooling Rate (ºC/min)	Cooling Style	Mean Aspect Ratio	Aspect Ratio Std. Dev	Modal Aspect Ratio
1	1.7	Steps	13.4	7.6	9
2	0.63	Steps	6.5	3.7	9
3	1	Steps	12.8	7.6	13
4	1.4	Steps	8.2	5.0	5
5	1	Ramp	8.2	4.7	5
6	0.1	Ramp	10.3	8.8	6
7	0.5	Ramp	5.8	3.9	6

Table 15. Details of aspect ratio mean, mode and standard deviation for each experimental run. This is taken from SEM data

Run	Cooling Rate (ºC/min)	Cooling Style	Mean Aspect Ratio	Std. Dev Aspect Ratio	Modal Aspect Ratio
1	1.7	Steps	9.5	3.6	11
2	0.63	Steps	6.49	3.2	7
3	1	Steps	6.57	2.6	6
4	1.4	Steps	6.63	4.5	5
6	0.1	Ramp	6.01	2.8	4

Table 16. Details of aspect ratio mean, mode and standard deviation for each experimental run. This is taken from microscope data.

When the data from these runs was compared to the equation and dataset given in Holness (2014), which relates crystallisation time to aspect ratio, the points from the experiments in this study generally fell on or near the line, within error (+/- 1) (Figure 49 and 50). This showed that the data are consistent with the extrapolation of the relationship described in Holness (2014), even though the crystallisation time in the experiments here was significantly shorter than the times given in that study.

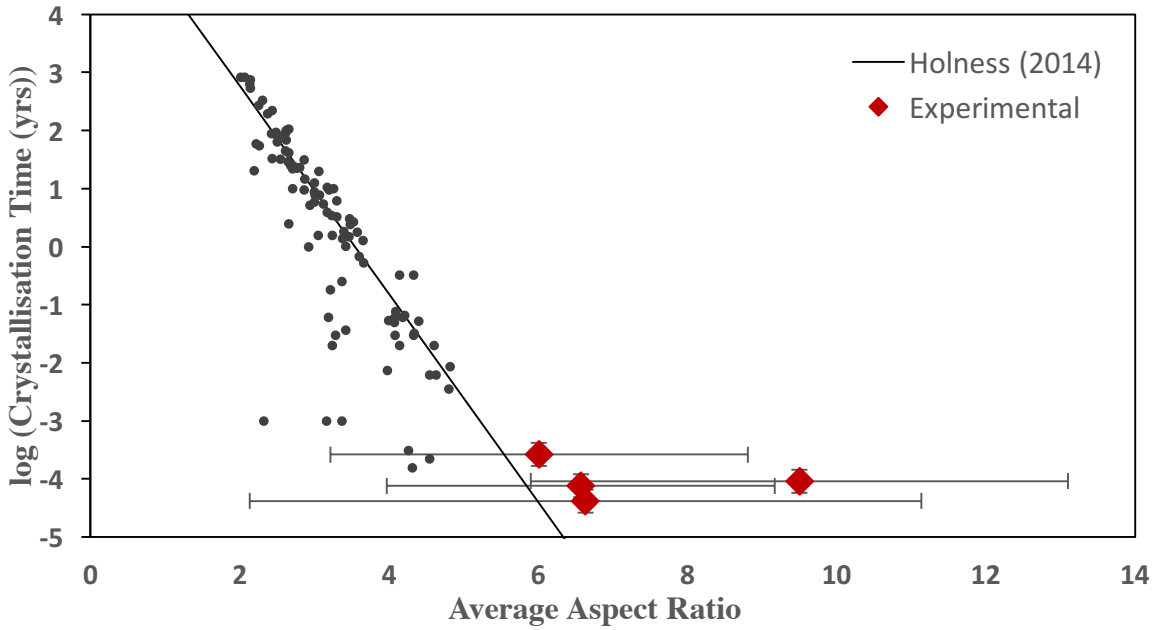

Figure 49. Data from the experiments done in this study, taken from optical microscope measurements, compared to data from Holness (2014) and the equation and line derived in that study. The error bars represent the standard deviation in the aspect ratio data.

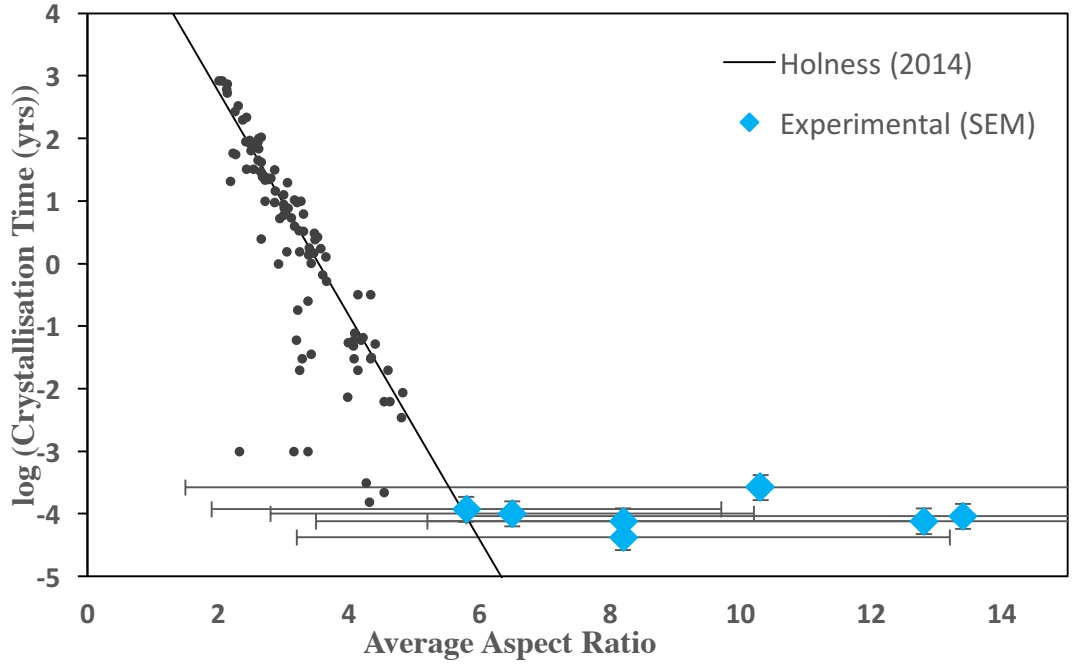

Figure 50. Data from the experiments done in this study, taken from SEM measurements, compared to data from Holness (2014) and the equation and line derived in that study. The error bars represent the standard deviation in the aspect ratio data.

Further to this, the data from the SEM and microscope measurements can be compared together to the Holness (2014) equation. Figure 51 shows the equation line, with the data from these experiments plotted on top. Whilst most datasets do seem to lie relatively close to the line, the SEM measurements yielded higher mean aspect ratios, and so lie further away from the line than their optically measured counterparts.

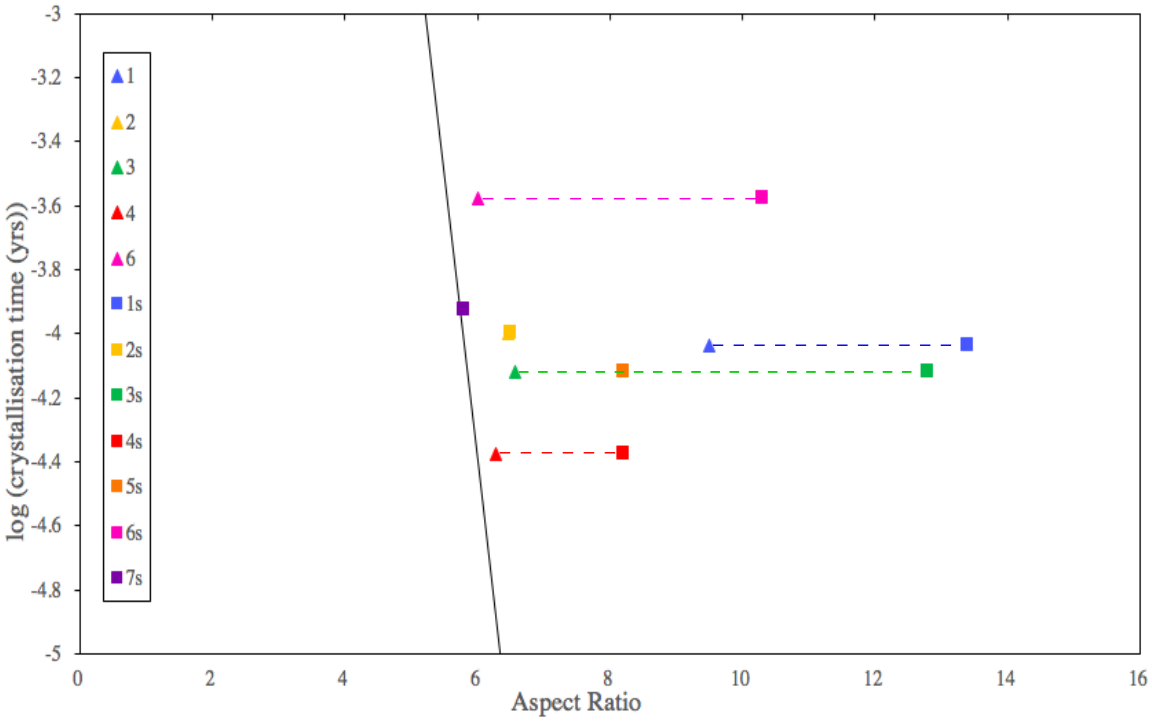

Figure 51. Data from the experiments done in this study compared to the equation and line derived in Holness (2014), for both SEM (squares) and microscope (triangles) measurements. Pairs of datasets for the same run are linked by the dotted lines, highlighting the difference between the datasets. The mean aspect ratio of experiment 2 was the same for both SEM and microscope measurements.

From the length and width data taken over time for runs 6 and 7, aspect ratio change over time was also plotted. In most individual cases, aspect ratio appeared to be increasing, but in others it appeared to be decreasing. Figure 52 shows the average aspect ratio of specific sets of crystals that were observed over time during crystallisation in runs 6 and 7, and how that aspect ratio changed with time. It seemed that for all except the crystals in run 7, the aspect ratio did not significantly change during cooling. Due to the larger uncertainty in the width measurements (and therefore in the aspect ratio calculations), it is possible that aspect ratio actually remained mostly static over time for these crystals. In addition to tracking individual crystals, measurements of a whole population of crystals in an area of the sample throughout experimental runs were taken. These displayed an increasing aspect ratio over time, with a mode that stabilised at 6 (Figure 53).

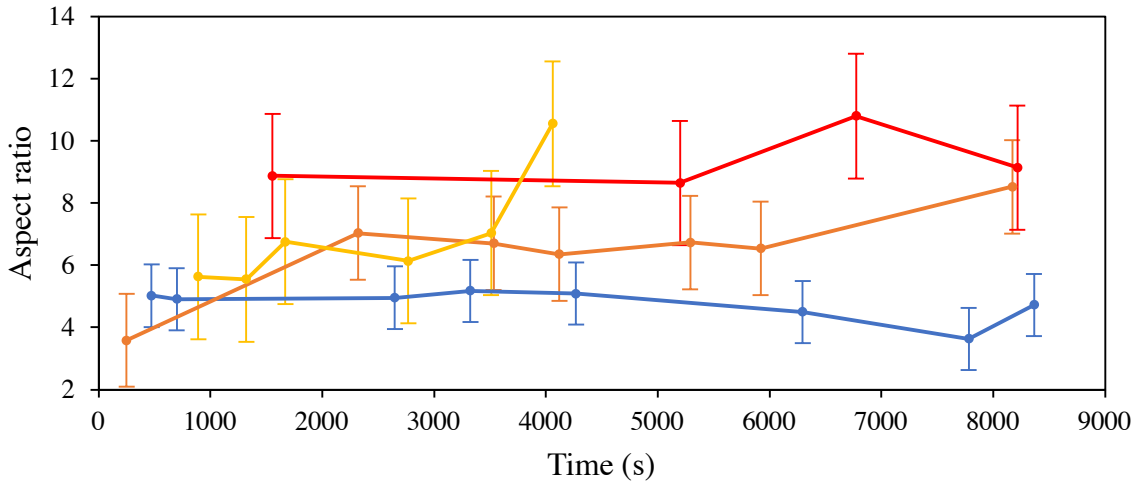

Figure 52. Averaged aspect ratio measurements for specific crystals over time. Each line pertains to a set of 5-10 crystals in one area of the sample and how their aspect ratio changed over time. The yellow line is from the 7th run, whilst the other 3 are from the 6th run. The uncertainty in the aspect ratios varies from 1 - 2 for each set of measurements.

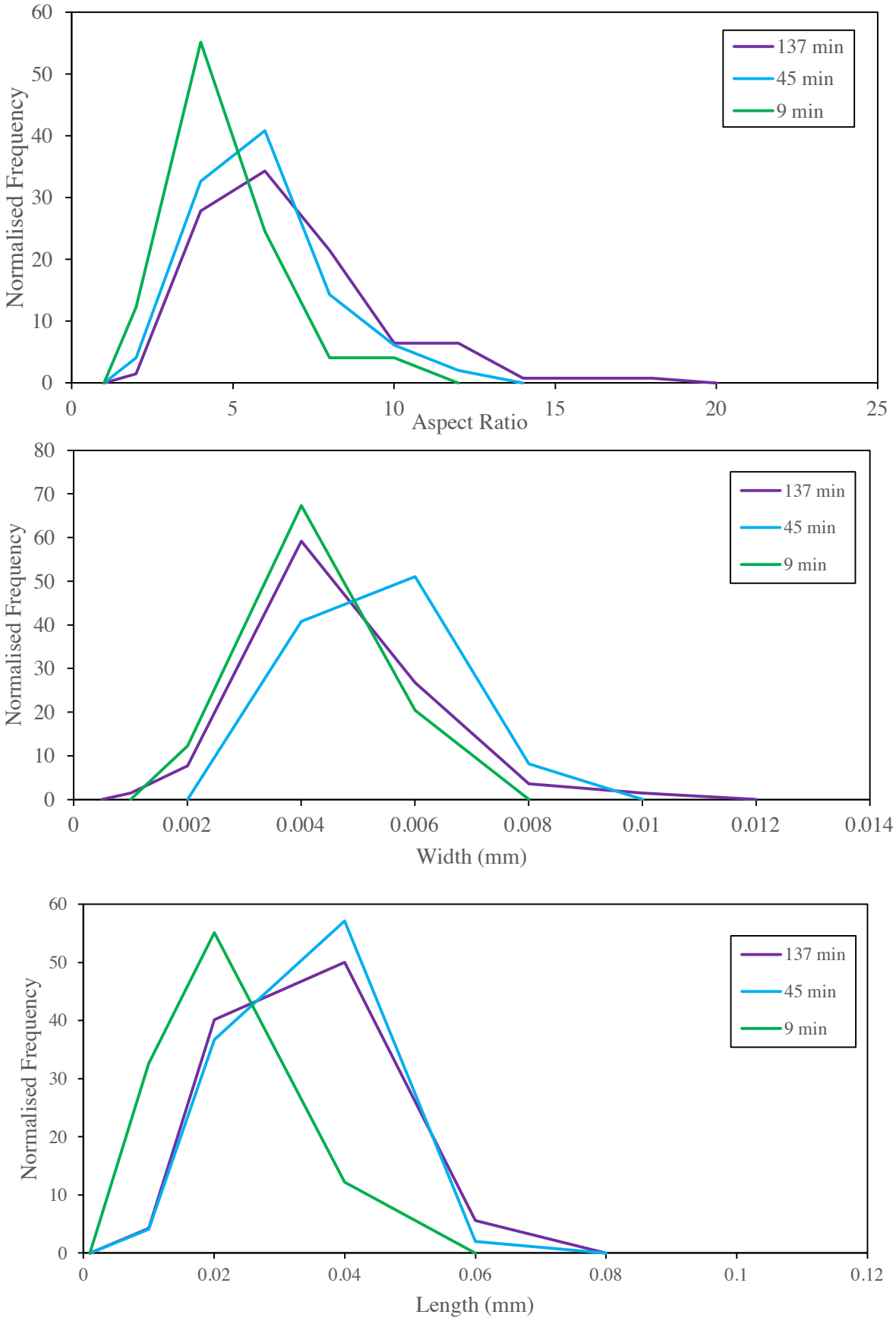

Figure 53. Aspect ratio, width and length change over time in sample 6. Each set represents the crystal aspect ratios 9, 45 and 137 minutes from the start of the cooling ramp. The uncertainty in the measurements of length and width is 0.001mm, and the average uncertainty of the aspect ratios is 1.4.

Figure 53 shows that, over time, the spread of aspect ratios increases and the modal aspect ratio increases. From experimental observations, it can be seen that the tabular morphology was maintained over time for the majority of the crystals in run 6 (Figure 54 below). It is worth noting that the number of crystals measured in the final dataset was larger as larger crystals were easier to make out in images. Each of these datasets has been normalised to 100 to allow for easier comparison of different dataset sizes. Lengths seem to increase over time, whilst widths appear to increase and then decrease – which could be a feature of the change in dataset size, or measurement errors caused by changing light quality as the sample cooled. From the first observed point in time to the last, it can be seen that lengths increase whilst width does not change significantly, which then results in the increasing aspect ratios. A 'students t-test' was carried out on these datasets to examine whether there was a significant difference between the aspect ratios for these datasets. The results from these tests showed that there was a significant difference between each pair of aspect ratio datasets (p value = 0.01).

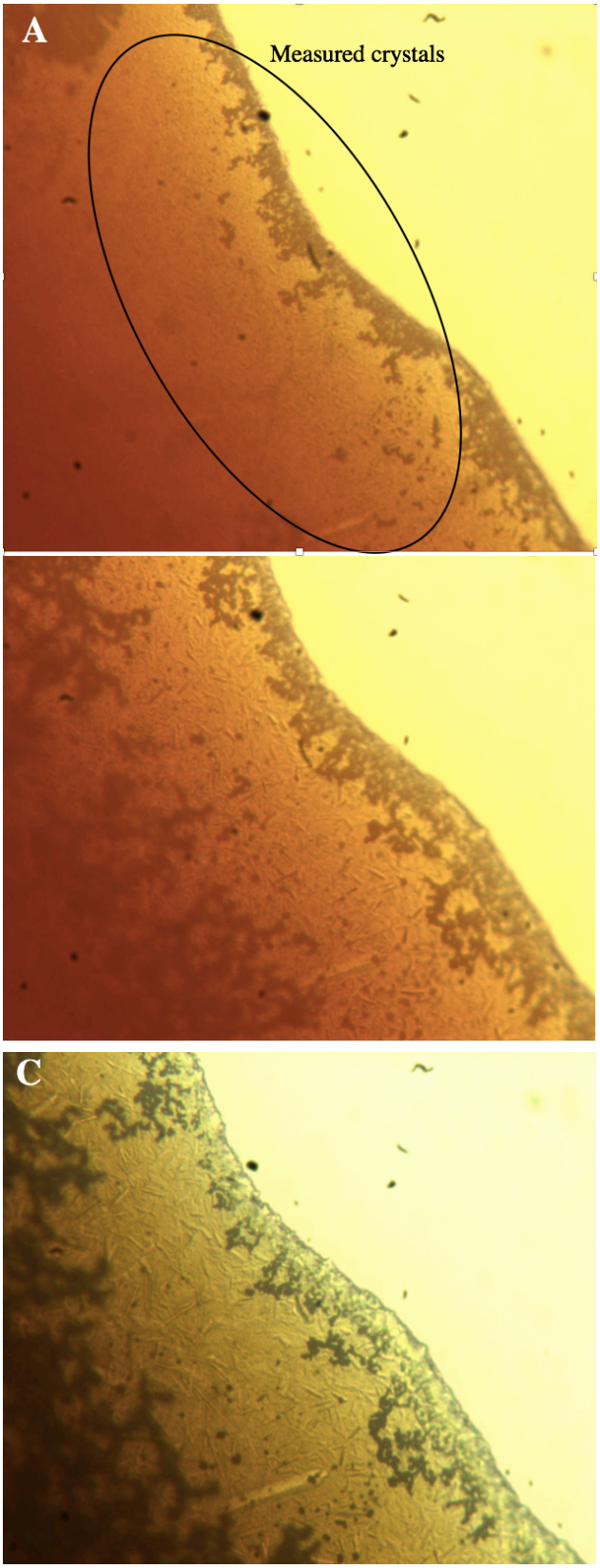

Figure 54. Photomicrographs of the three points during the experiment that were used to measure the crystals in Figure W. A is after 9 minutes of cooling, at 1174ºC, B is after 45 minutes, at 1169ºC, and C is at 137 minutes, at 1155ºC

5.5 3D Shape of Plagioclase

The 3- dimensional shape of the plagioclase crystals can be inferred from the 2D length and width measurements taken. Morgan and Jerram (2006) describe a method, created to support methods described in Higgins (2000), where 2D crystal length and width data can be taken and compared to curves derived from libraries of 2D slices through 3D crystal shapes with prescribed axis ratios, for 703 different crystal habits. These curves were determined by modelling the axis ratios of 10,000 slices through each different crystal shape. The output of the spreadsheet from this work ("CSDSlice") can therefore give an idea of the crystal habit from the 2D data from these experiments. The shapes compared in this spreadsheet however, were limited by a maximum axis ratio of 1:10 for each set of axes, since that is the limit of the original modelling done by Morgan and Jerram (2006). For the SEM data from runs 3 and 6 the crystal habit matched by the spreadsheet did not produce a curve that was at all similar to the 2D data input and had a low R^2 value, probably because the axis ratios exceeded 1:10. Table 17 presents the specific axis ratios given by the CSDslice spreadsheet for each length and width dataset. A new method building on the work of Morgan and Jerram (2006) was developed recently, ShapeCalc (Mangler et al., in review), which uses a greater range of crystal shapes up to 1:20:20. This method was used to better constrain the 3D shape from width and length measurements and gave results with stronger fits to the data (Table 18, and shown in full in Figure 57 at the end of this section). There was some discrepancy in aspect ratio and crystal size between the SEM and Microscope images, possibly due to the fact that most of the microscope measurements were taken from the sample edges, whilst SEM data covered the internal part of the sample, where crystals were unconstrained on all sides. The differences may also exist because the SEM images represent a slice of the crystal, whilst the optical photomicrographs are a projection. Across the samples, plagioclase aspect ratios did not show significant change across the whole population over time, which suggests that the 3D shape

(derived from CSDslice) also did not vary significantly over time, as the modal 2D Width/Length is equivalent to the 3D short/intermediate axis ratio. From the ShapeCalc results, it can be seen that there are 2 types of morphology. One is elongated, where the intermediate axis is around half of the long axis – experiments 2, 4, 5,6 and 7. In the second morphology the intermediate axis is similar to the long axis, giving a squarer, platy shape – experiments 1 and 3, both of which had more elongated crystal forms in 2D sections.

Sample	n (SEM)	SEM, CSDSlice	R^2	n (mic)	Microscope, CSDSlice	R^2
1	393	1:10:10	0.5	154	1:9:10	0.9
2	174	1:6:10	0.8	-	-	-
3	240	1:1:2.9	0.4	128	1:5:10	0.97
4	276	1:9:9	0.9	215	1:4.5:10	0.9
5	186	1:9:9	0.8	-	-	-
6	235	1:1:3.6	0.6	189	1:5:9	0.9
7	239	1:5:10	0.8	-	-	-

Table 17. CSDslice spreadsheet results for best-match axis ratios for the length and width data for each sample. Missing values are due to datasets not being large enough to meet the recommended minimum of ~200 crystals.

Sample	n	SEM, ShapeCalc	R_c^2
1	393	1:17:20	0.935
2	174	1:6.2:19	0.988
3	240	1:20:20	0.939
4	276	1:8:17	0.989
5	186	1:7.8:20	0.974
6	235	1:8.8:14	0.951
7	239	1:5.6:13	0.989

Table 18. ShapeCalc spreadsheet results for best-match axis ratios for the length and width data from SEM imaging for each sample. Rc^2 is the cumulative R^2 value.

The platy shape of the plagioclase crystals could be seen to present itself more clearly in some images, but generally, due to the probability of slicing the crystals perpendicularly to their width, the crystals appeared as thin rectangles in 2D. There was no preferential alignment of crystals. Images taken in both optical microscopes and SEM supported the conclusions of the CSDslice and ShapeCalc spreadsheets, and there were examples of plagioclase displaying a platy and flat leaf-like shape (Figure 23 above, and illustrated further in Figure 55 below).

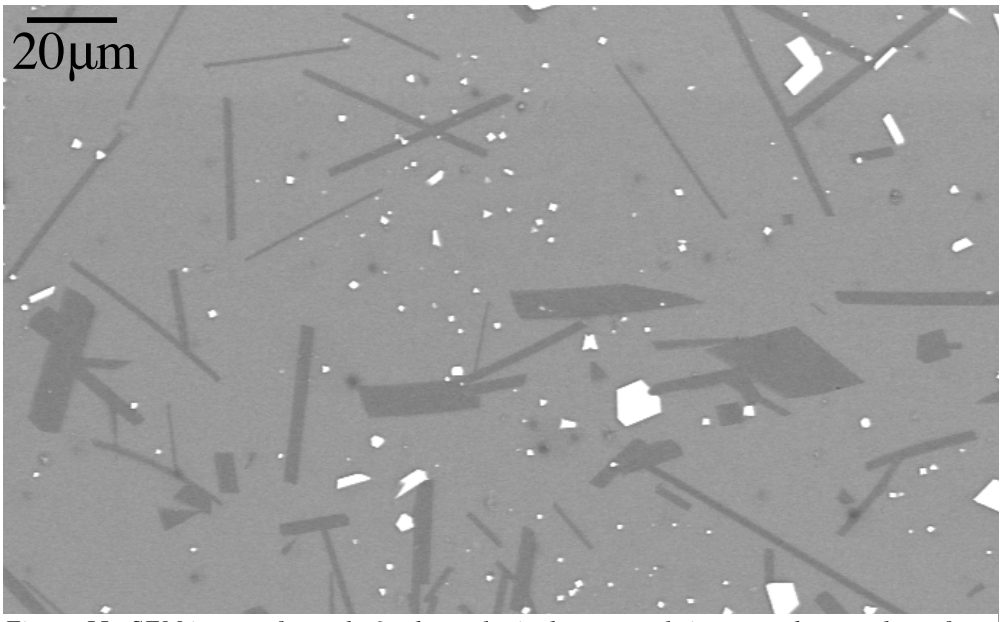

Figure 55. SEM image of sample 6, where plagioclase crystals intersect the sample surface at different angles, resulting in a variety of aspect ratios. The wider shapes exhibit the platy nature of the crystals.

Another way of helping to visualise the 3D crystal shape is to plot the shape data on to a Zingg diagram (Figure 56). This uses the axis ratios of the crystals, as determined from CSDslice or ShapeCalc, to graphically show how crystal morphology varied with each experiment. The plot is divided into sectors which each represent a type of crystal morphology. All plagioclase crystals from these runs fell into either the platy or flat and columnar/bladed categories within this diagram. There was a tendency for slower cooling rates resulting in crystals that were more elongated, rather than platy.

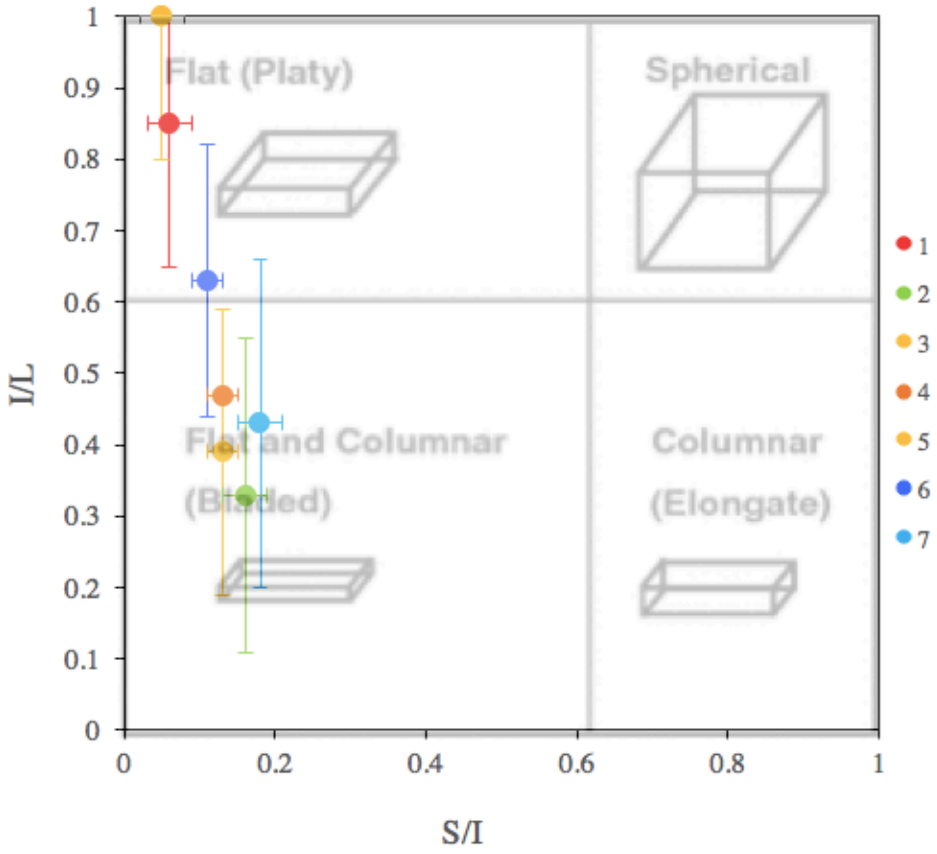

Figure 56. Zingg plot showing how plagioclase crystal morphology differed across each experimental run, from ShapeCalc results. The warmer colours denote higher cooling rates, while the cooler colours represent slower cooling rates. Errors represent 1 S.D, and are output by the ShapeCalc spreadsheet.

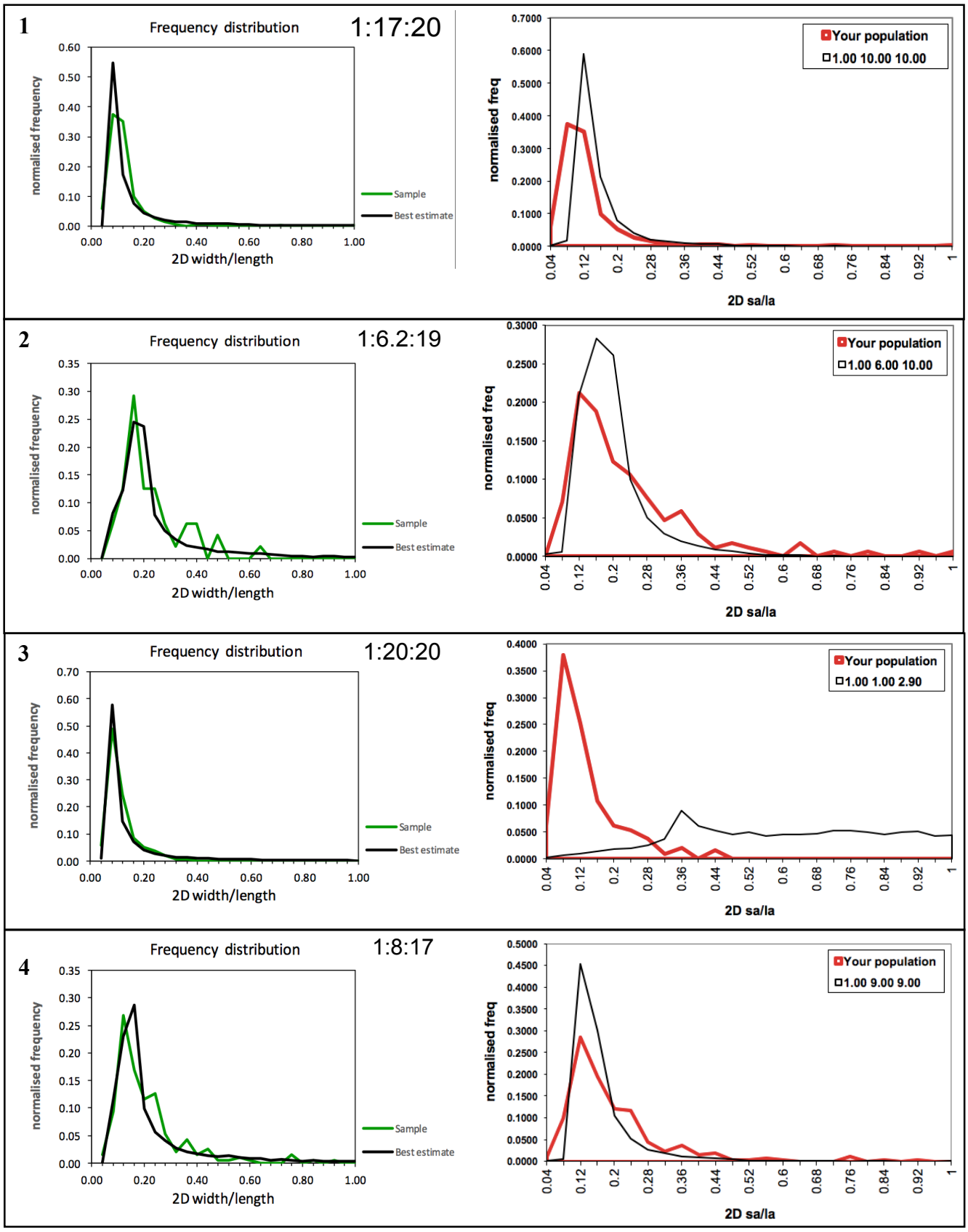
1
Frequency distribution
1:17:20
normalised frequency
2D width/length
Sample
Best estimate
normalised freq
2D sa/la
Your population
1.00 10.00 10.00
2
Frequency distribution
1:6.2:19
normalised frequency
2D width/length
Sample
Best estimate
normalised freq
2D sa/la
Your population
1.00 6.00 10.00
3
Frequency distribution
1:20:20
normalised frequency
2D width/length
Sample
Best estimate
normalised freq
2D sa/la
Your population
1.00 1.00 2.90
4
Frequency distribution
1:8:17
normalised frequency
2D width/length
Sample
Best estimate
normalised freq
2D sa/la
Your population
1.00 9.00 9.00

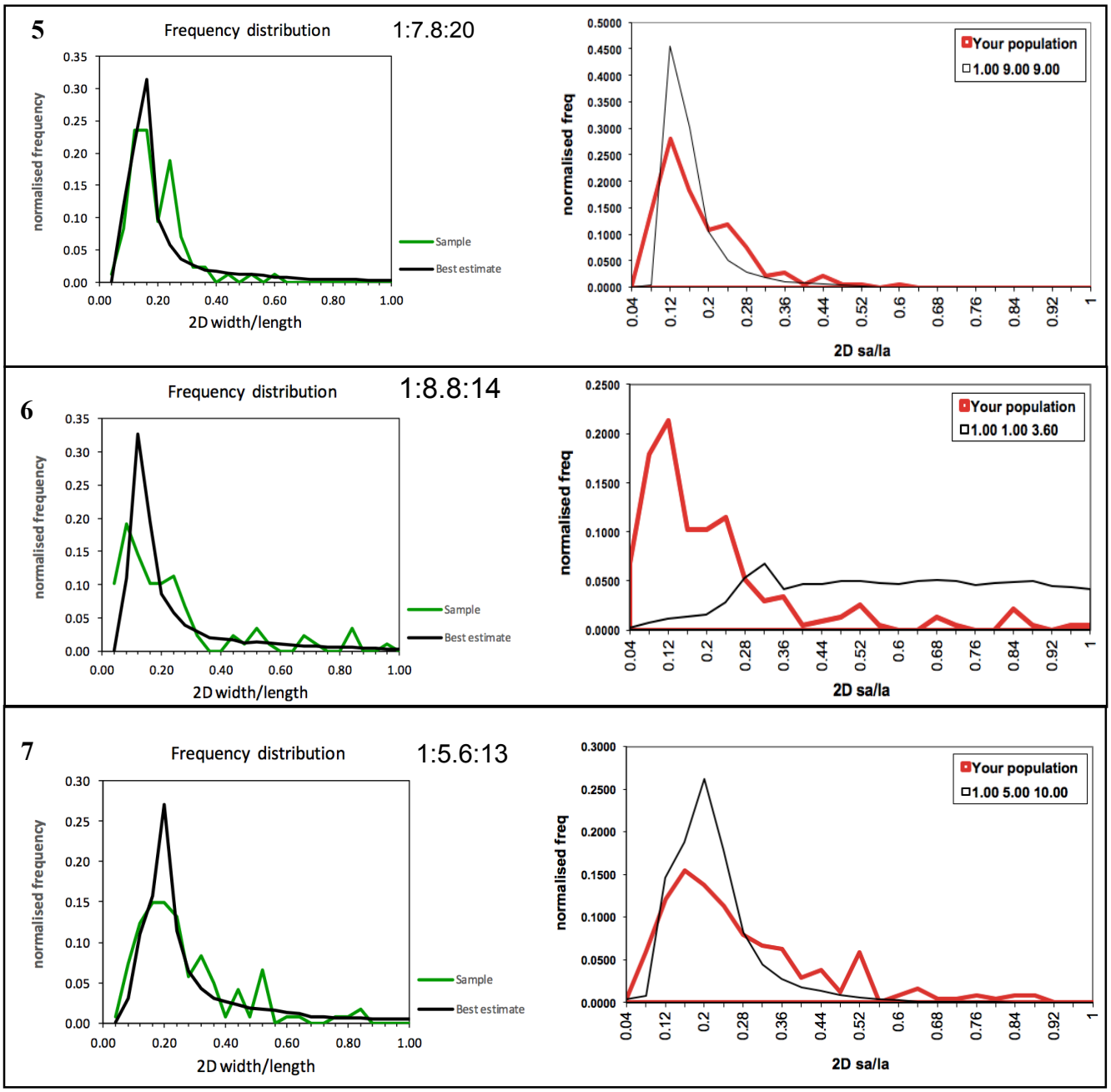

Figure 57. Comparison of the frequency distribution curves from Shapecalc (left) and CSDSlice (right), calculated from length and width data for plagioclase crystals in SEM images of each sample.

5.6 Crystal Number Density

Using CSDCorrections, developed by Higgins (2000), and run on Wine (Kronenberg, 2019), crystal length and width measurements taken within a specified area, along with the 3D shape calculated from ShapeCalc, were used to calculate the crystal number density from each experiment. The results are presented below (Table 19).

Run	Number density (m^{-3})	Cooling rate (ºC/min)	Quench T (ºC)	Initial DT (ºC)
1	9.892E+14	1.7	1150	10
2	8.007E+14	0.63	1150	10
3	1.551E+15	1	1150	10
4	3.311E+14	1.4	1140	20
5	4.662E+14	1	1140	10
6	2.555E+15	0.1	1155	5
7	5.815E+15	0.5	1150	0.5

Table 19. Showing Number density for each run, along with cooling rate and additional temperature information.

When crystal number density is compared with cooling rate, there is a very weak relationship between the two, with an R^2 value of 0.3. This is shown in Figure 58.

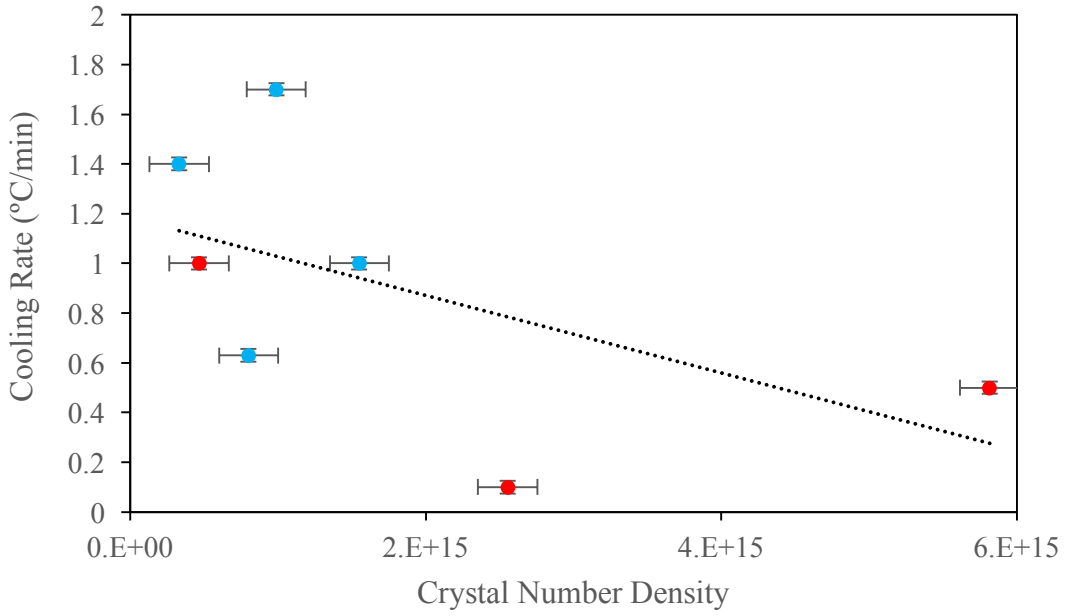

Figure 58. Plot showing the lack of correlation between crystal number density and cooling rate. Error bars represent uncertainty in cooling rate propagated from measurement and timing uncertainties (see chapter 3.5)

5.7 Crystal Growth Rates

The growth rates of plagioclase crystals were a key output from these experiments. It was possible to measure an average plagioclase growth rate from quenched samples, as well as to measure instantaneous and evolving growth rates in some experimental runs. For each experiment, a set of measurements of crystal length and widths was taken to create a crystal size data set for plagioclase crystals. Measurements were primarily taken of the quenched sample. SEM data mostly represented the crystals in the central, thicker areas of the sample, whilst microscope images allowed for the measurement of the crystals at the very edges of the sample, which was an area difficult to polish down to without losing much of the sample due to its thickness (40-100μm). Some comparable areas were measured to ensure that there was no large difference between SEM measurements and microscope image measurements. The crystals growing towards the edge of the sample were often found to be shorter than those growing more centrally. SEM measurements have a smaller error due to having a larger magnification and clearer picture. For these datasets, the data has been organised so that SEM measurements are related to the crystals growing more centrally (more than 0.1mm away from the edge of the sample), whilst the microscope dataset refers to crystals growing within 0.1mm of the edge, often within the 'window' of oxide cover described above.

For each experimental run, 2D length and width data from the quenched samples were used to calculate an average crystal growth rate in the two directions. The time used for each of these growth rates was taken as the time from when cooling began (when temperature was held at or was dropped from 1180ºC, depending on the experiment conditions), as no crystal growth was observed until then. Experimental observations and MELTS modelling suggested that that 1180ºC was the temperature from which plagioclase began to grow. A simple calculation of dividing the total length or width of the crystal by the experimental time' was used to calculate growth rates. The crystal length and width growth rates for each experiment

are reported below in Tables 20 and 21, from data taken using the SEM and data taken from optical microscope images. There was a difference in the uncertainty associated with each of these datasets, where optical microscope growth measurements have a greater uncertainty. These growth rates accounted for all crystals within the imaged region, regardless of any systematic differences in crystal size. Samples 5 and 7 had extensive oxide growth and darkening that made it difficult to optically image the sample in a way that allowed for measurement.

Run	SEM Growth rate (m/s)	Microscope Growth rate (m/s)	Cooling Rate (ºC/min)
1	1.7×10^{-8}	2.1×10^{-8}	1.7
2	8.1×10^{-9}	2.15×10^{-8}	0.63
3	1.1×10^{-8}	3.18×10^{-8}	1
4	2.1×10^{-8}	2.36×10^{-8}	1.4
5	9.6×10^{-9}	-	1
6	2.5×10^{-9}	3.2×10^{-9}	0.1
7	2.8×10^{-9}	-	0.5

Table 20. Calculated average length growth rates from the quenched sample of each experimental run.

Run	SEM Growth rate (m/s)	Microscope Growth rate (m/s)	Cooling Rate (C/min)
1	1.48×10^{-9}	2.36×10^{-9}	1.7
2	1.36×10^{-9}	3.6×10^{-9}	0.63
3	9.17×10^{-10}	5.23×10^{-9}	1
4	3.02×10^{-9}	4.15×10^{-9}	1.4
5	1.4×10^{-9}	-	1
6	3.26×10^{-10}	7.05×10^{-10}	0.1
7	6.29×10^{-10}	-	0.5

Table 21. Calculated average width growth rates from the quenched sample of each experimental run.

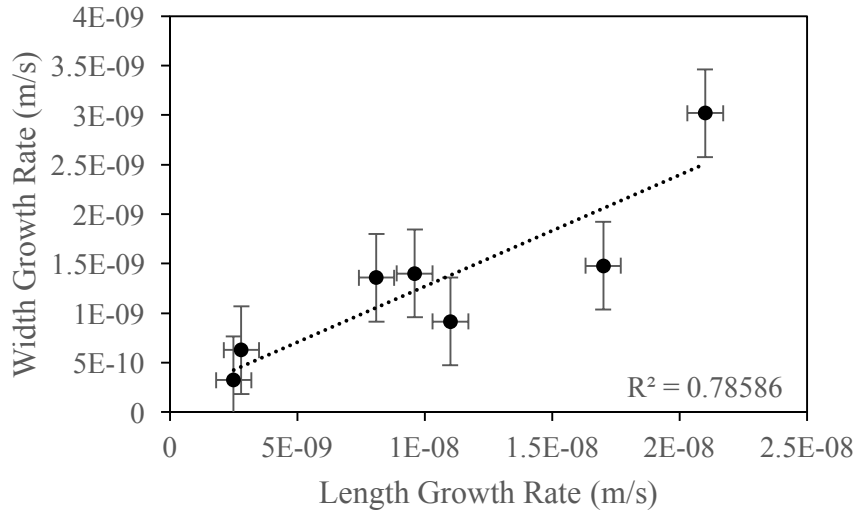

Figure 59. Relationship between average width and length growth rates

Figure 59 above shows the relationship between the average growth rates for lengths and widths for all experiments. Length and width growth rates are therefore likely to be affected by the same controls. Error bars represent the average uncertainty in the measurements for growth rate, calculated by propagating the uncertainties in the measurement of total crystal growth time, and length and width.

Figure 60 below shows the relationship between the average cooling rate of the experimental runs and the average length growth rate (from SEM data) of plagioclase crystals. There was a strong general trend of growth rates increasing with cooling rates, as evidenced by a high R^2 value for the trend line.

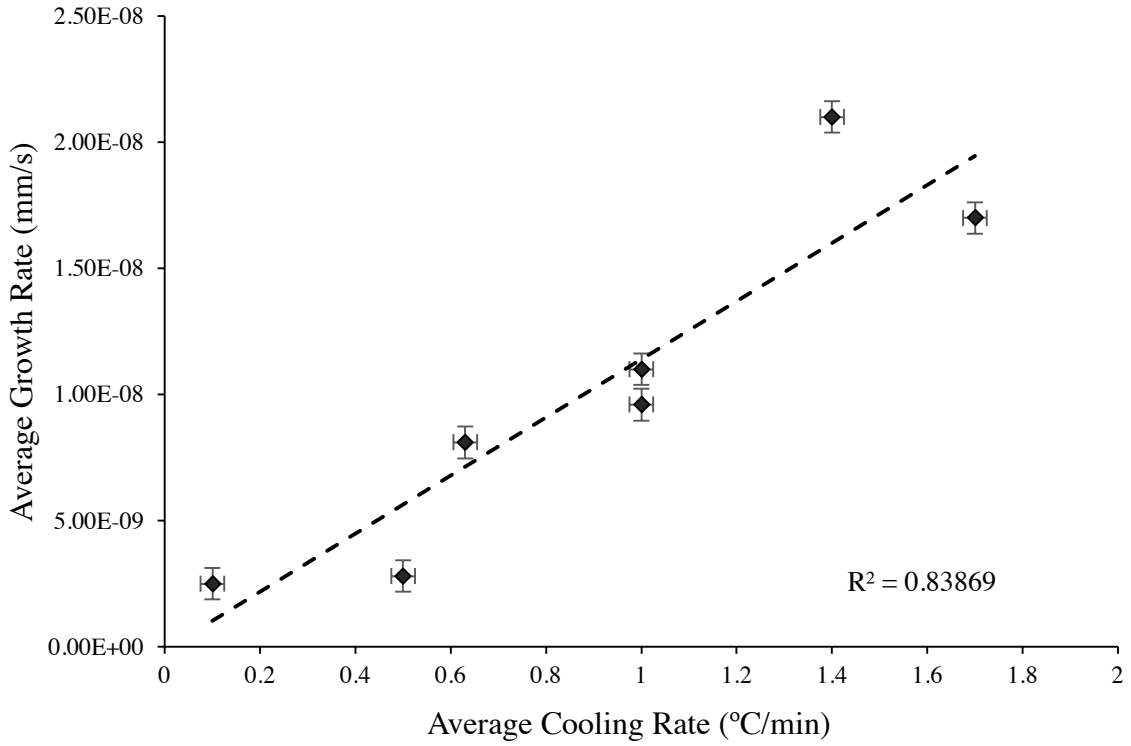

Figure 60. Plot of average cooling rate vs average plagioclase growth rate for all experimental runs. Error bars represent the average uncertainty in growth rates and cooling rates, propagated from the uncertainties in length, time and temperature (see chapter 3.5).

The lengths were also a feature that was found to change with cooling rate. Experiments with higher cooling rates seem to lead to greater average and modal crystal lengths (Figure 61). This is likely to be linked with the increasing growth rates seen for faster cooling rates.

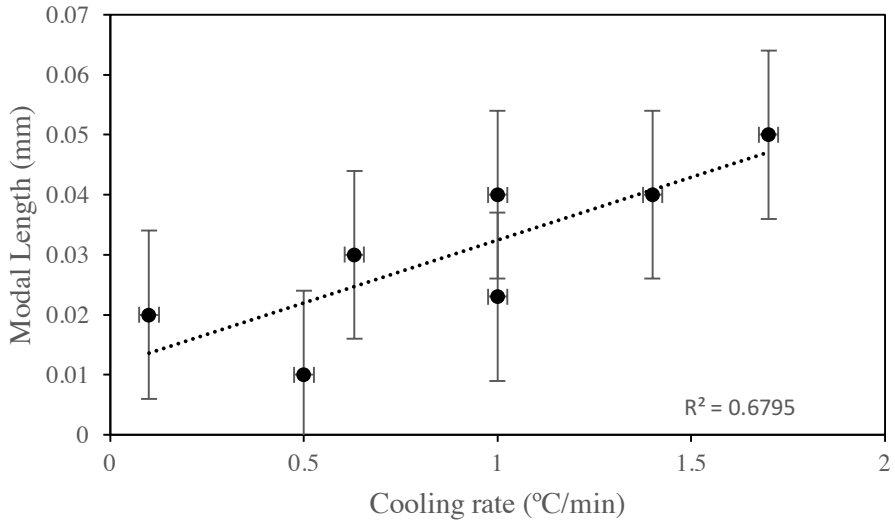

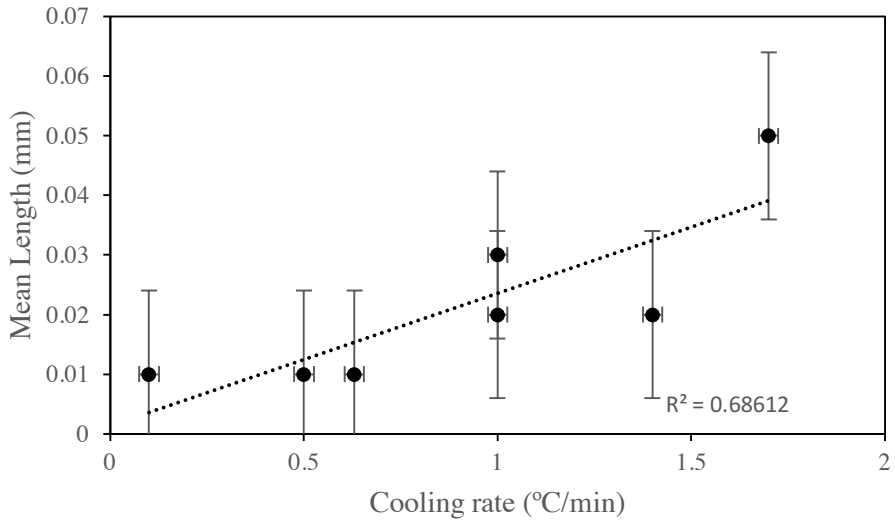

Figure 61. Plots of the modal and mean crystal lengths for each experiment versus the cooling rate for those experiments. There is a clear positive trend between these two measures. The error bars represent 1 standard deviation.

In the 6th and 7th experimental runs, it was possible to track the length and width of the crystals in 3 areas of sample 6 and one area of sample 7 during cooling and growth. 20 crystals from run 6 were tracked, and 6 from run 7. Crystal growth rates were clearly not constant over time, and eventually all crystals reached a point where growth slowed down to a near halt as temperature dropped and total effective undercooling increased. It seemed that growth rate after nucleation started relatively quickly, but then slowed down over time. Width was also tracked over time, though there seemed to be very little change in the width over time for most crystals, with occasional small amounts of growth. Most measured changes in width fell within the error value of the measurements, so it is possible that there was actually no change over time for many of these crystals. This would account for some apparent increase in aspect ratio of specific crystals over time. When compared to the average calculated bulk growth rates from quenched samples, the growth rates calculated have a similar magnitude to those calculated at different points for the tracked crystals.

The following pages of figures show each area from which the tracked crystals were imaged and measured, with the specific crystals labelled, the following plots then show how the lengths, widths and growth rates of these crystals varied over time. The error on the growth rates is likely to be higher than shown at the first measured point due to uncertainty on the exact starting moment of growth. Error bars in the figures represent the approximate 1μm uncertainty on length and width measurements in optical photomicrographs.

6a.

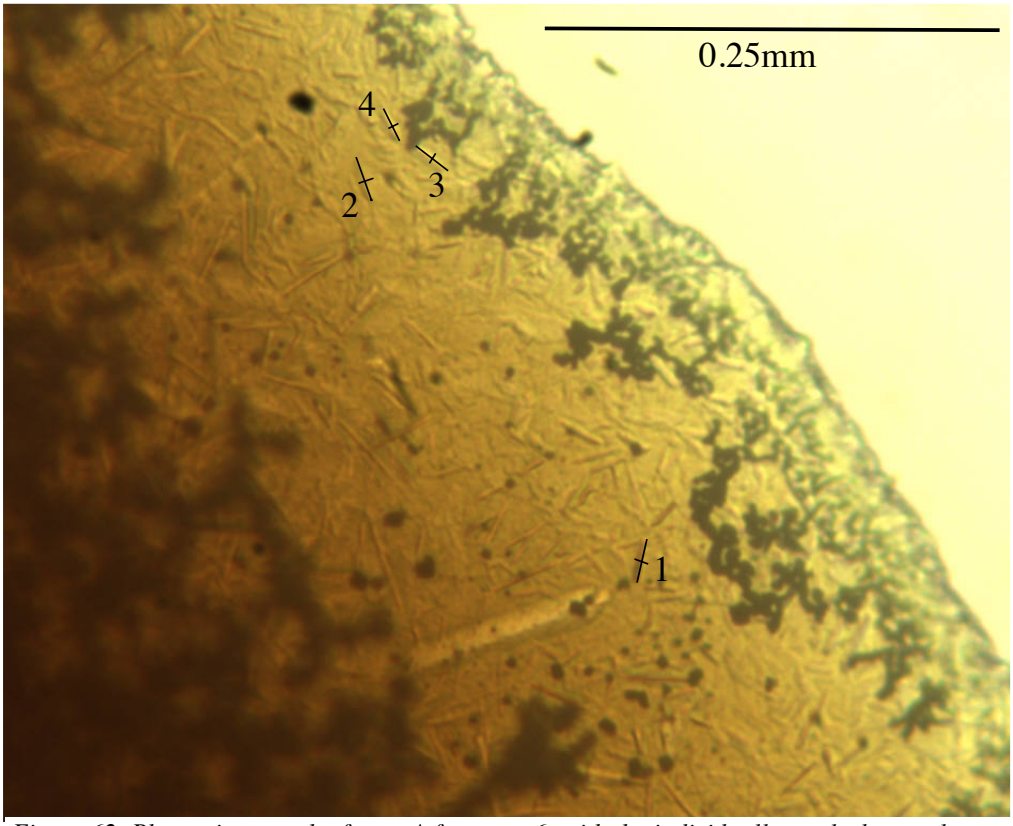

Figure 62. Photomicrograph of area A from run 6, with the individually tracked crystals marked

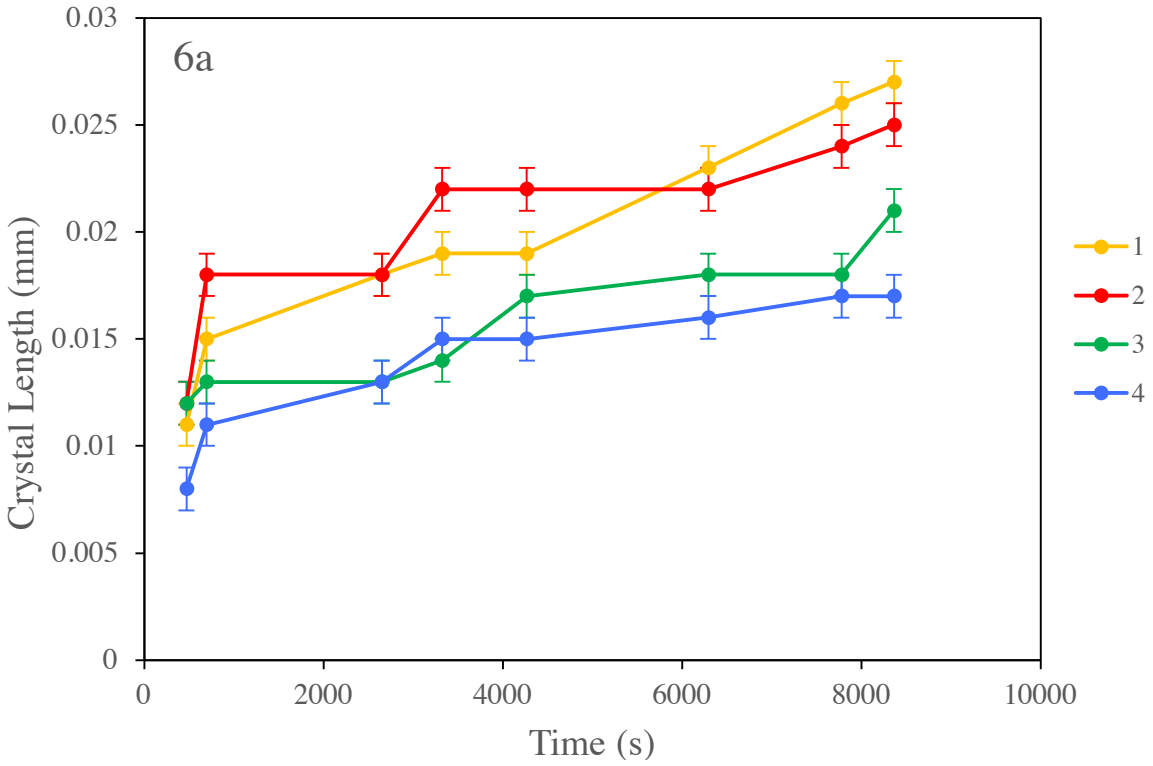

Figure 63. Plot of the changing lengths over time of the individually tracked crystals from run 6, area A. Error bars represent error of 1μm on measurements.

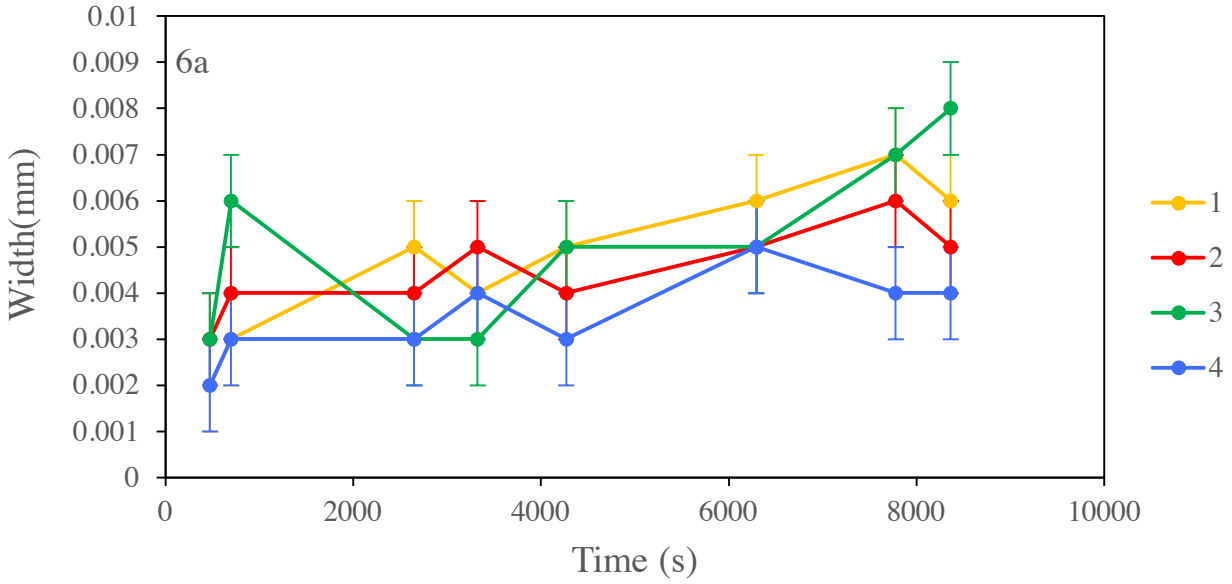

Figure 64. Plot of the changing widths over time of the individually tracked crystals from run 6, area A. Error bars represent error of 1μm on measurements.

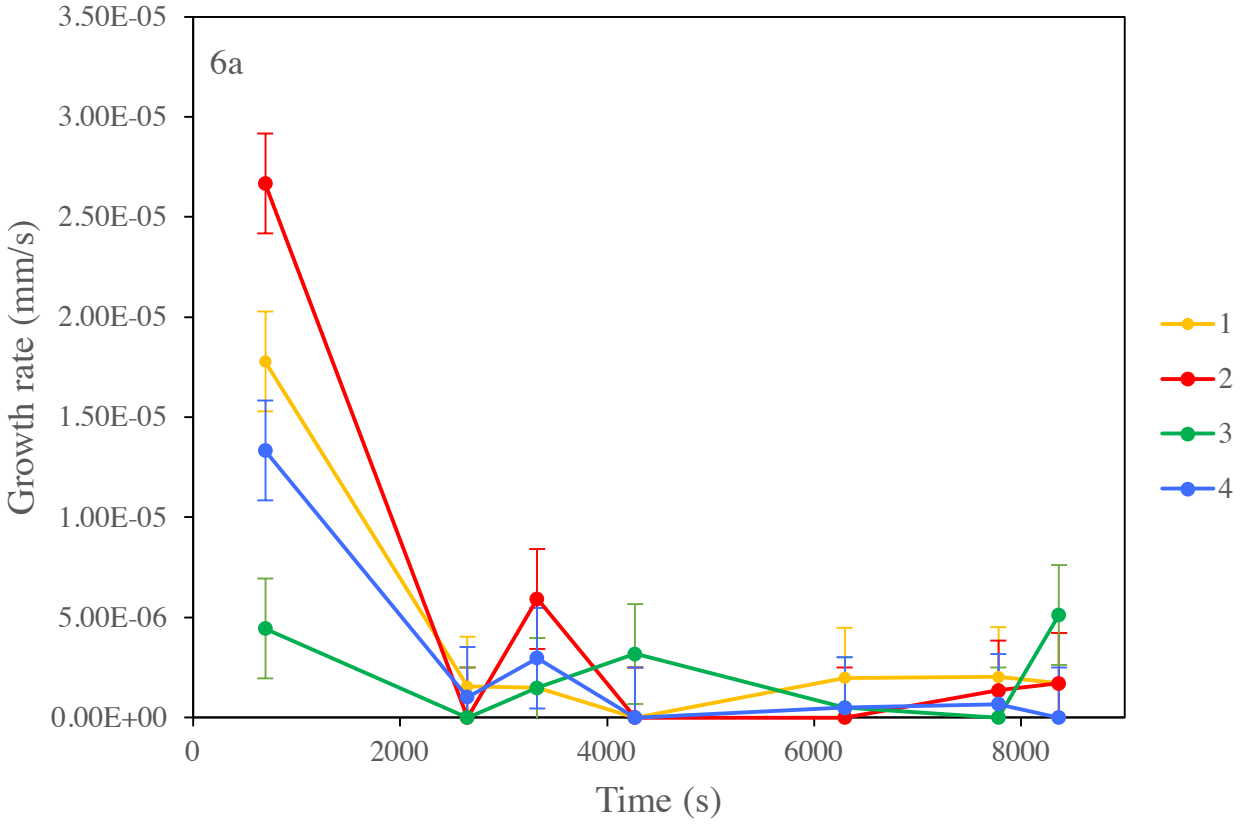

Figure 65. Plot of the changing growth rates over time of the individually tracked crystals from run 6, area A. Error estimated from measurement variability.

6b.

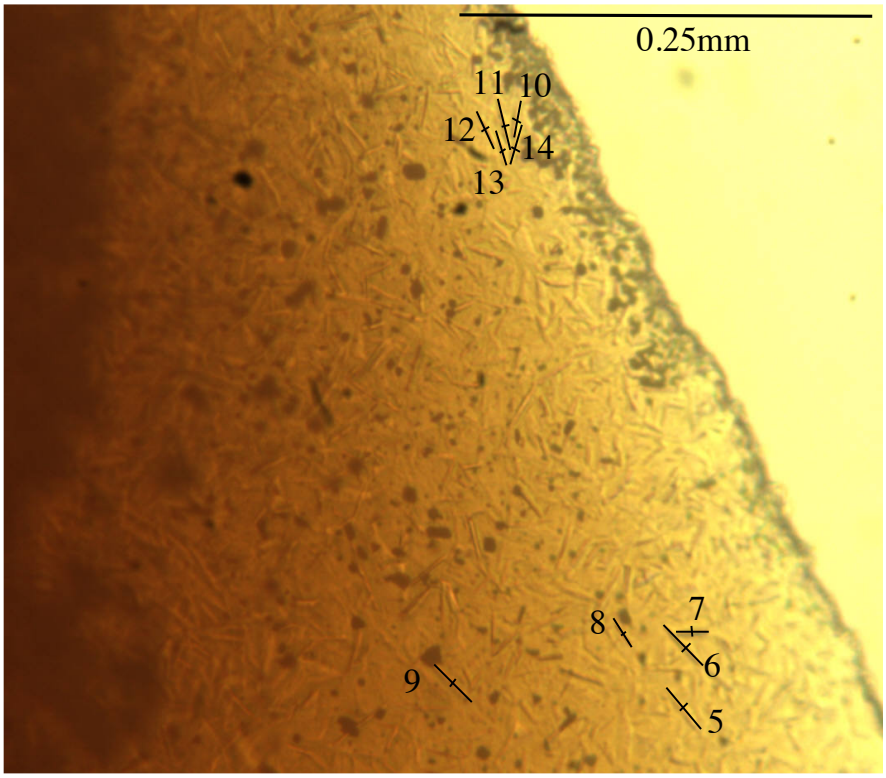

Figure 66. Photomicrograph of area B from run 6, with the individually tracked crystals marked and labelled.

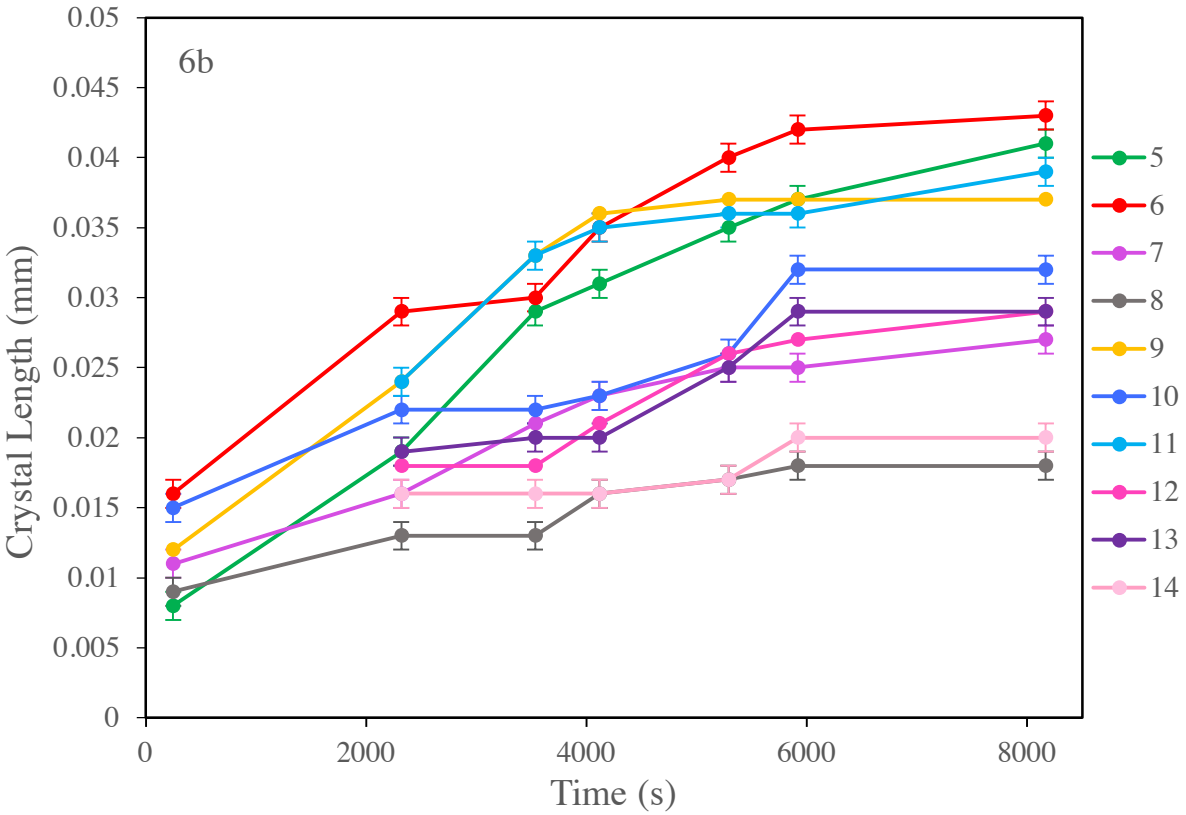

Figure 67. Plot of the changing lengths over time for the individually tracked crystals from run 6, area B. Error bars represent measurement uncertainty of 1μm

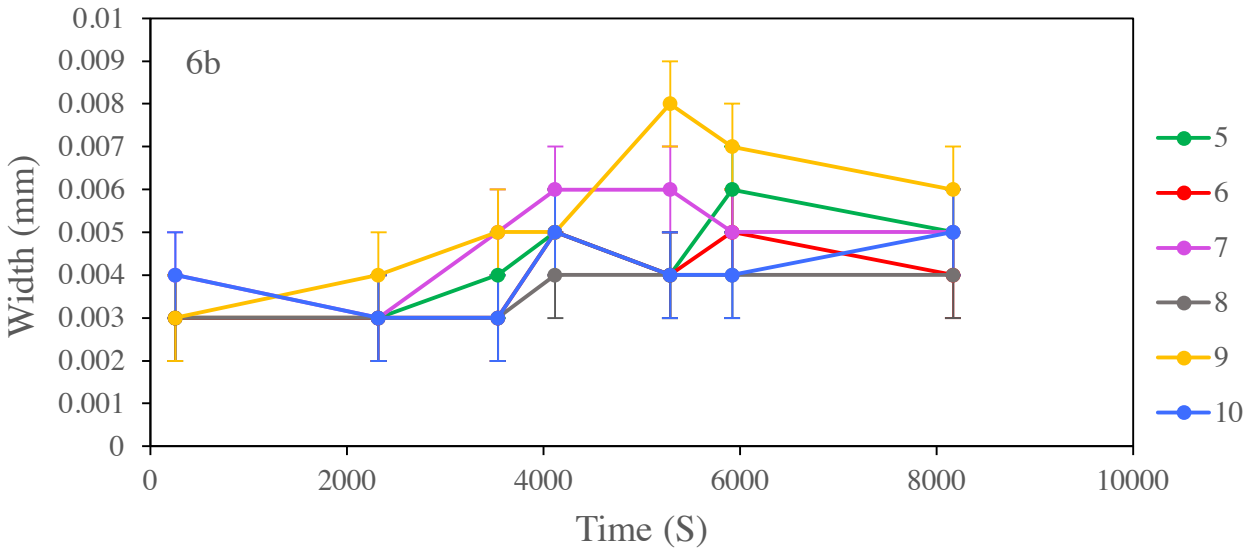

Figure 68. Plot of the changing widths over time for crystals 5-10 tracked from run 6, area B. Error bars represent measurement uncertainty of 1μm

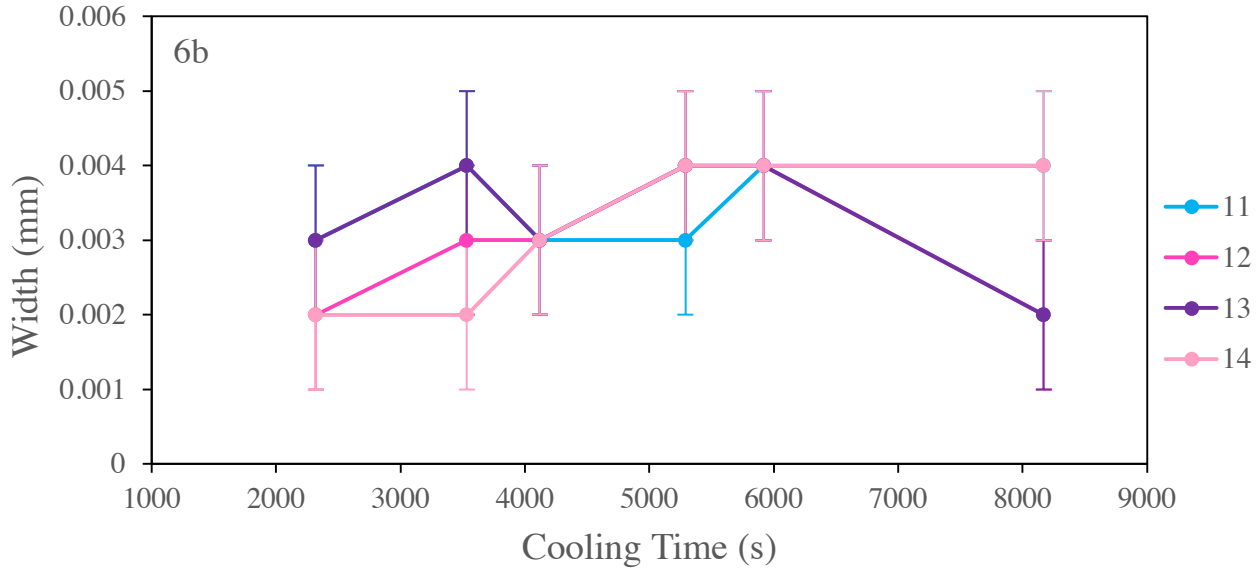

Figure 69. Plot of the changing widths over time for crystals 11-14 tracked from run 6, area B. Error bars represent measurement uncertainty of 1μm

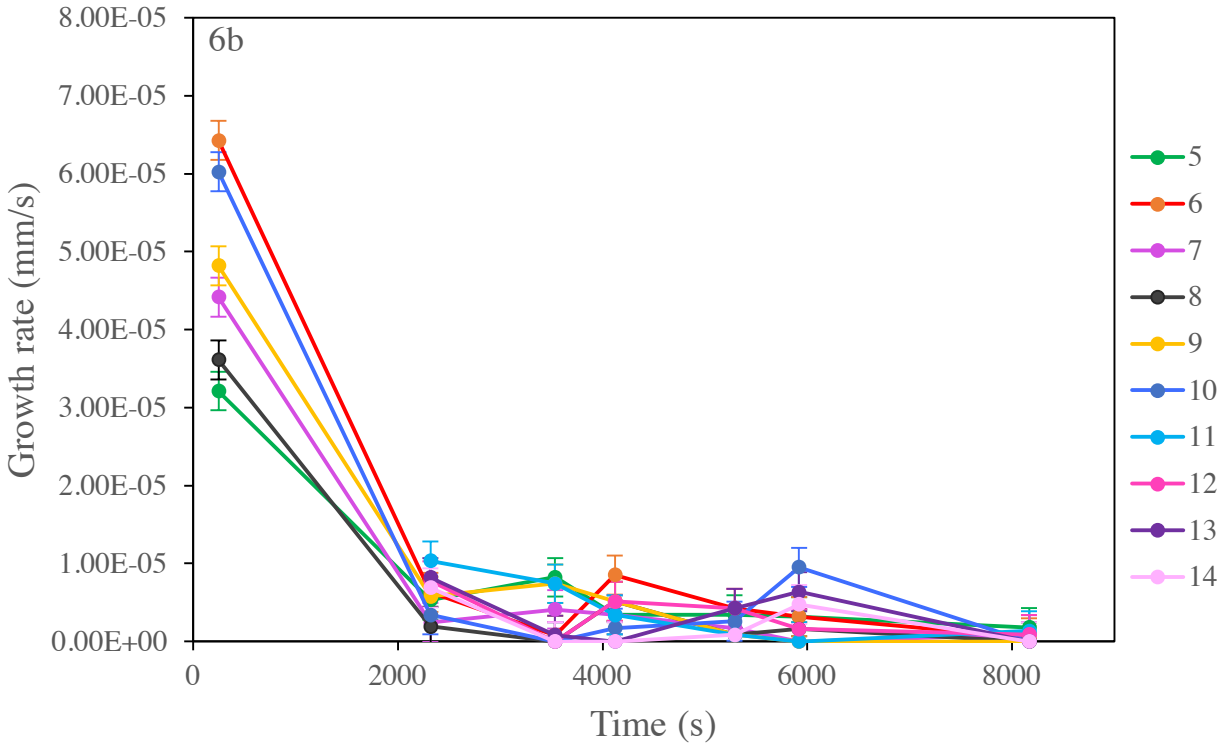

Figure 70. Plot of the changing length growth rate over time for the individually tracked crystals from run 6, area B. Error bars represent measurement variability.

6c.

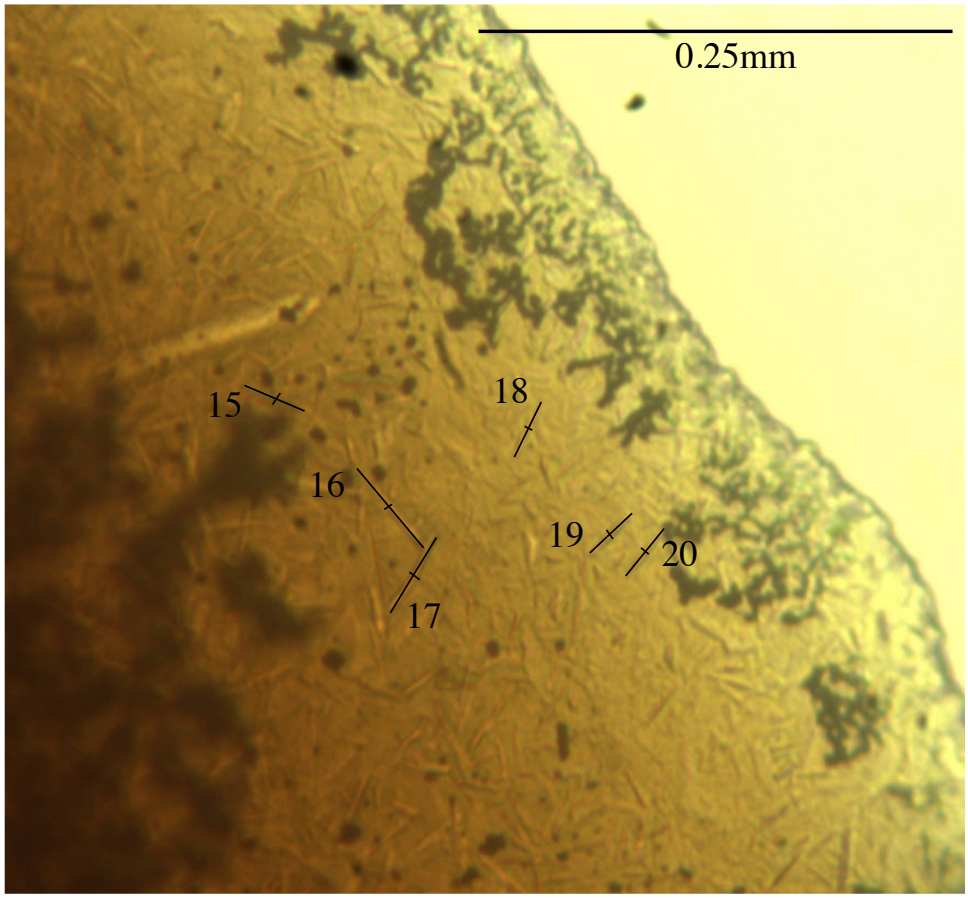

Figure 71. Photomicrograph of area C from run 6, with the individually tracked crystals marked and labelled.

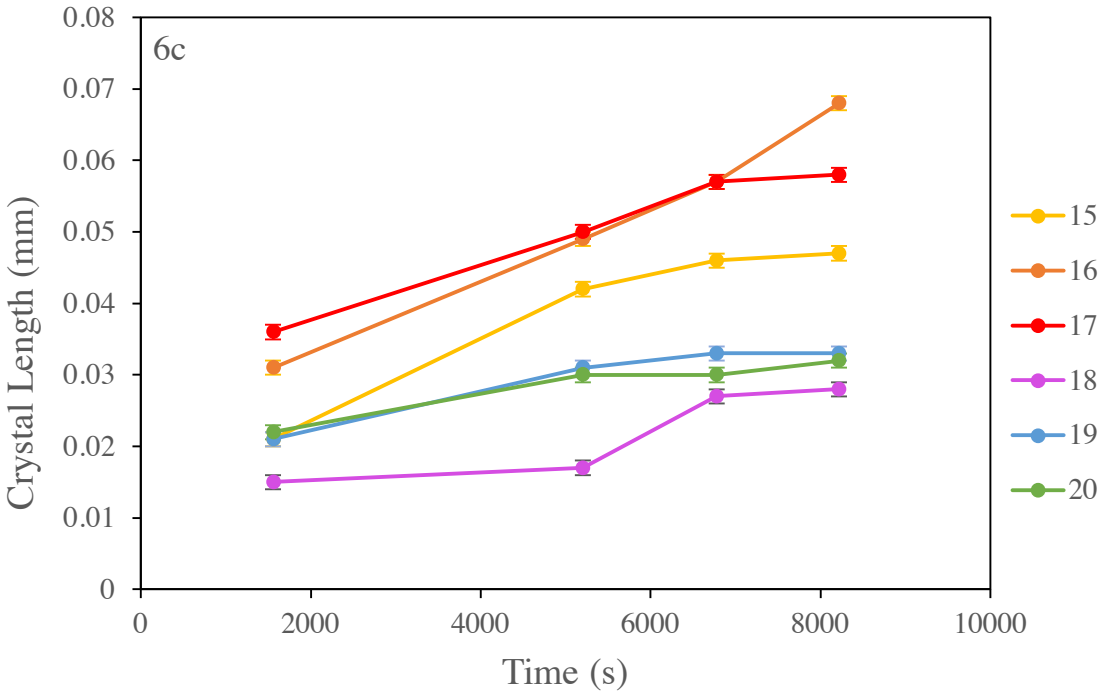

Figure 72. Plot of the changing length over time for the individually tracked crystals from run 6, area C. Error bars represent measurement uncertainty of 1μm

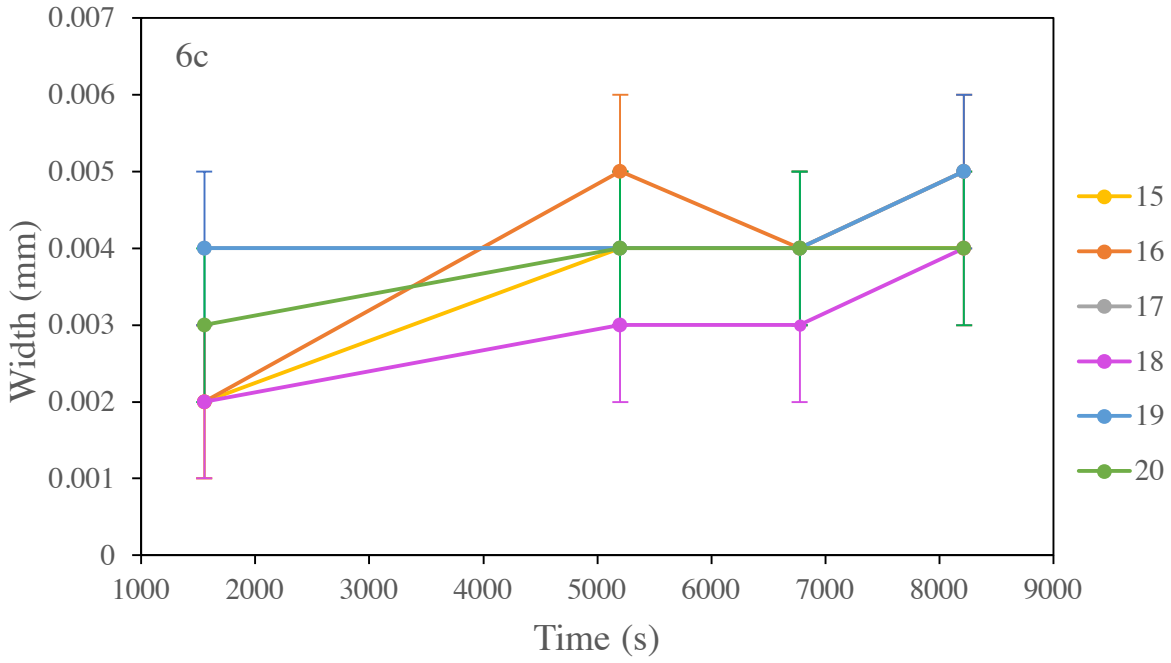

Figure 73. Plot of the changing width over time for the individually tracked crystals from run 6, area C. Error bars represent measurement uncertainty of 1μm

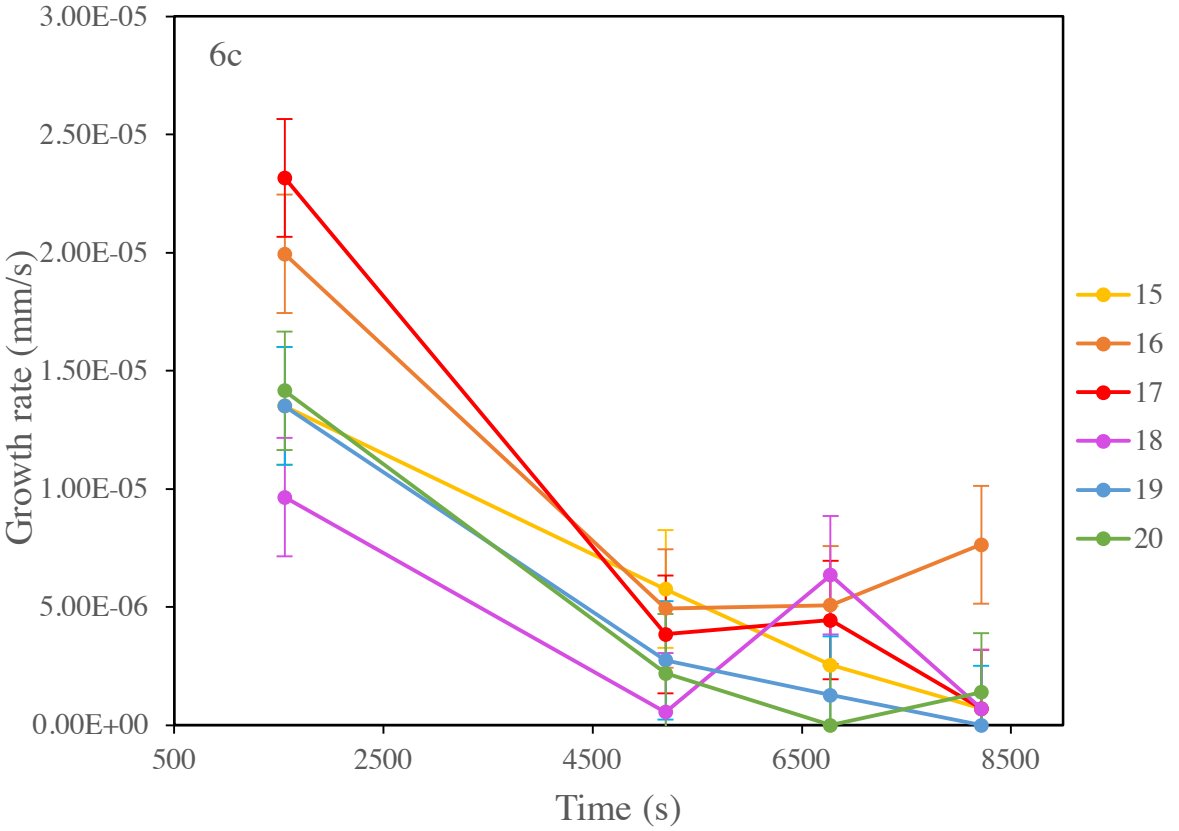

Figure 74. Plot of the changing growth rate over time for the individually tracked crystals from run 6, area C. Error bars represent measurement variability.

7.

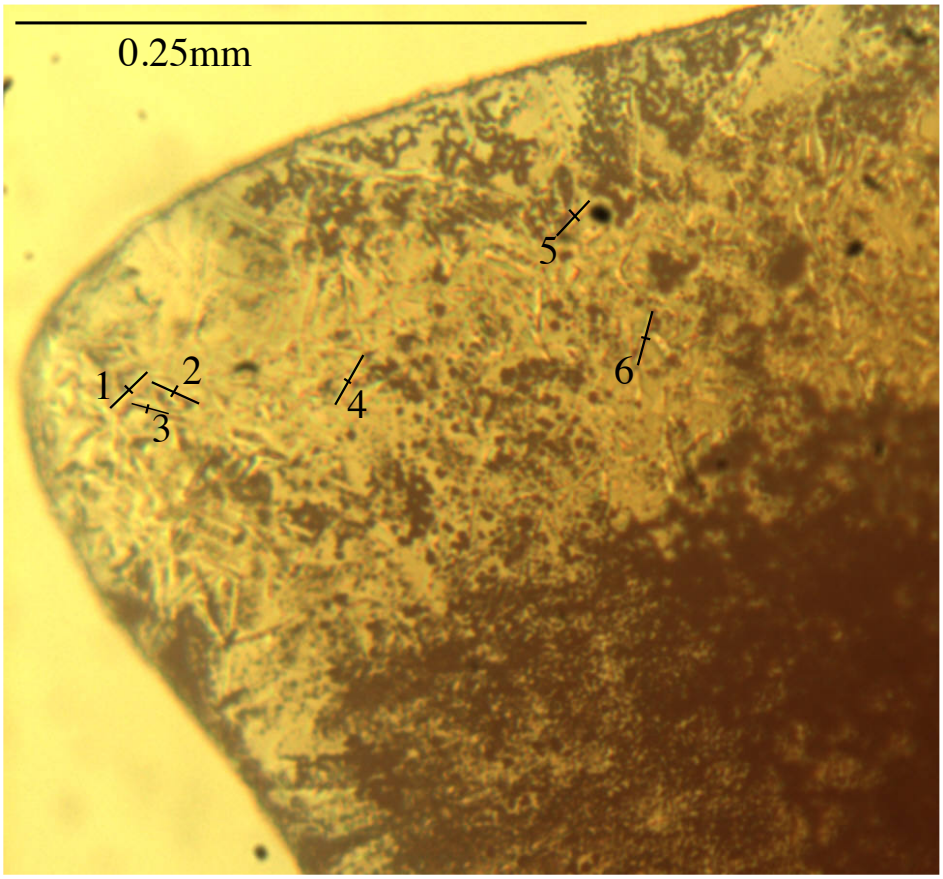

Figure 75. Photomicrograph showing the individually tracked crystals from run 7.

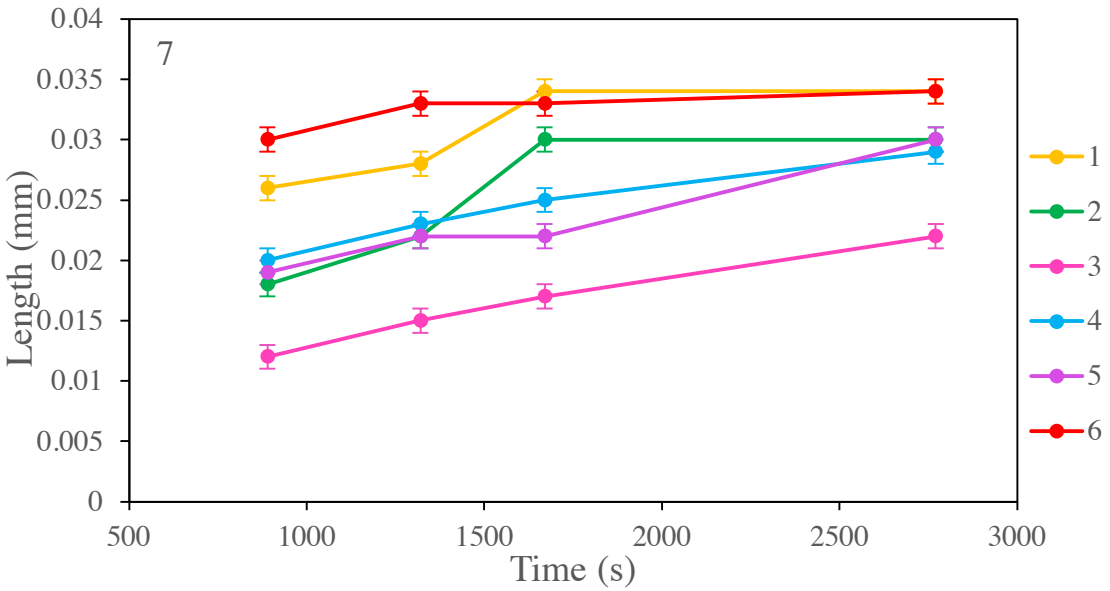

Figure 76. Plot of the changing length over time for the individually tracked crystals from run 7. Error bars represent measurement uncertainty of 1μm

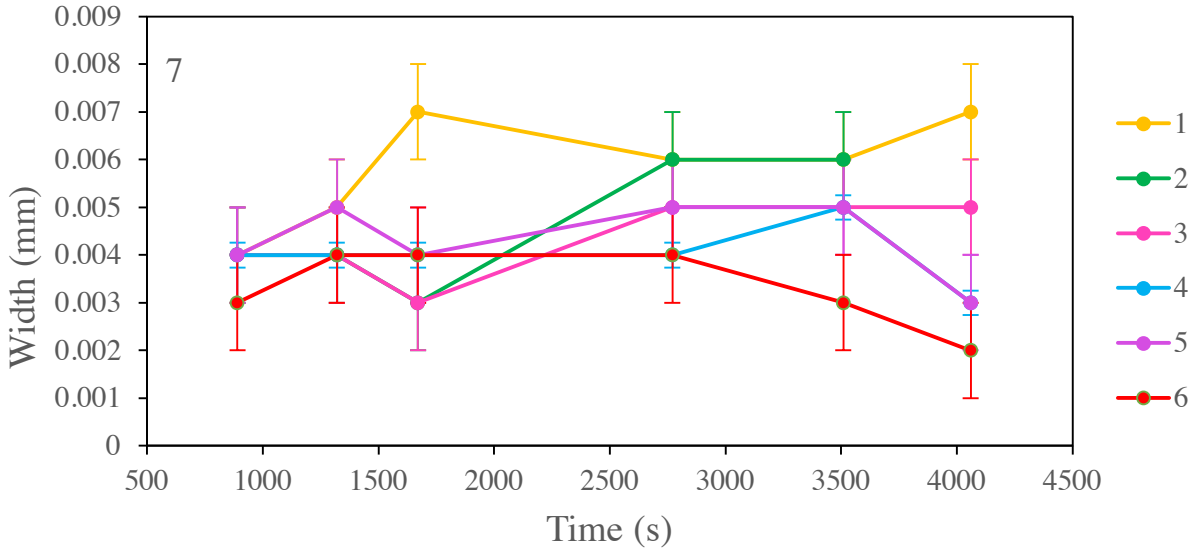

Figure 77. Plot of the changing width over time for the individually tracked crystals from run 7. Error bars represent measurement uncertainty of 1μm

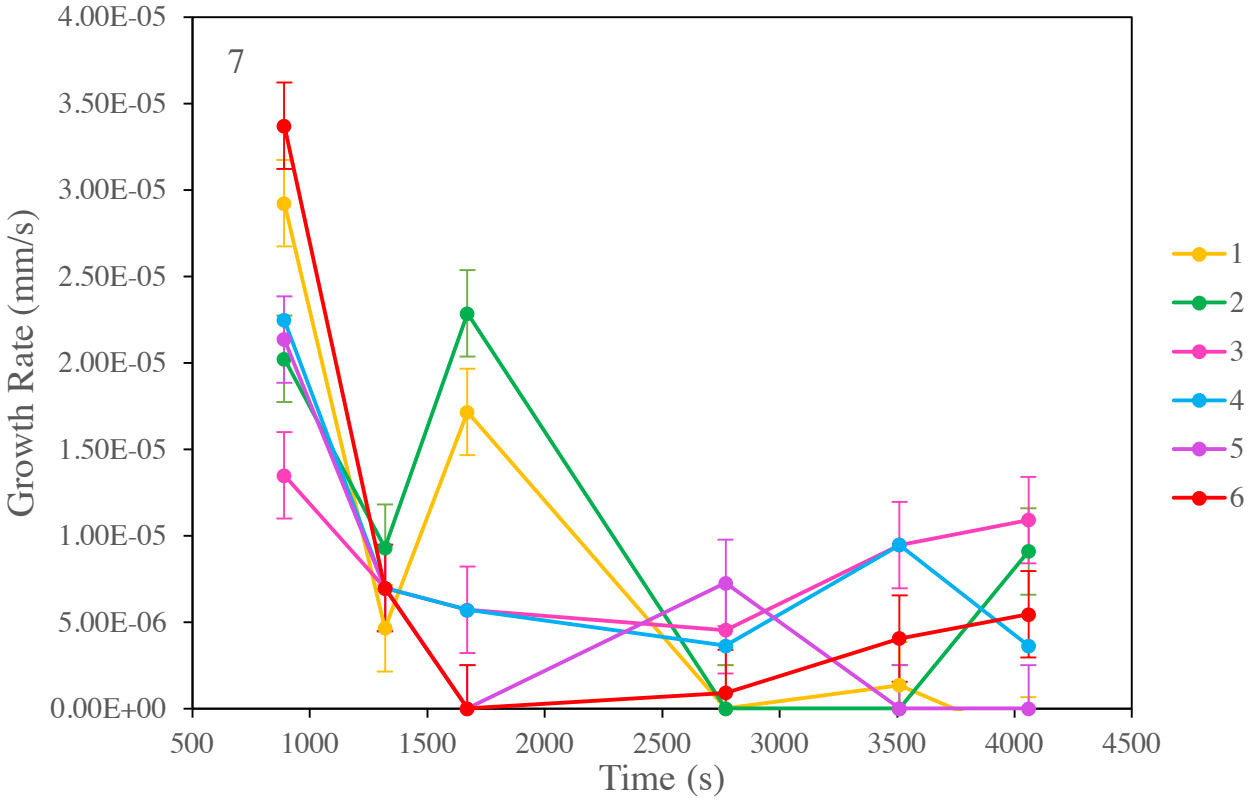

Figure 78. Plot of the changing growth rate over time for the individually tracked crystals from run 7. Error bars represent measurement variability.

5.8 Chemical Analysis

An Energy Dispersive X-ray Spectroscopy (EDS) analysis was carried out on samples 1, 3, 4 and 7, allowing them to be compared to the natural BGP analysis and MELTS modelling. These samples were taken as representative for the whole set. The results of the EDS analysis on the experimental run samples are shown in Tables 22-25.

Plag (n = 12)	**SiO_2**	**Al_2O_3**	**Na_2O**	**CaO**	**Total**	**X_{An}**
Average	52.1	28.2	4.5	15.2	100	64.8
Range	50.6 - 53.9	26.7-29.5	3.8 - 5.2	14.6 - 15.7	-	60.9 - 69.7

Table 22

Oxides (n = 6)	**SiO_2**	**Al_2O_3**	**MgO**	**TiO_2**	**Fe_2O_3**	**Cr_2O_3**	**Total**
Average	1.3	6.9	12.3	2.7	76.4	0.3	99.9
Range	0 - 2	6.3 - 7.6	10.8 - 13.1	2.5 - 2.9	72.5 - 78.6	0 - 1.0	-

Table 23

Cpx (n = 8)	**SiO_2**	**Al_2O_3**	**MgO**	**TiO_2**	**Fe_2O_3**	**Total**
Average	44.8	6.4	15.6	2.0	10.2	79
Range	43.5 - 49.2	4.4 - 7.2	19.9 - 13.1	0 - 2.2	8.0 - 11.3	-

Table 24

Glass (n=8)	**SiO_2**	**Al_2O_3**	**Na_2O**	**CaO**	**MgO**	**TiO_2**	**Fe_2O_3**	**Total**
Average	51.3	14.5	2.6	12.7	6.3	4.6	9.8	101.8
Range	50.5 - 52.2	12.5 - 25.5	2.3 - 3.5	12.0 - 15.1	1.2 - 7.1	3.0 -3.2	10.0 - 11.3	-

Table 25. EDS analysis results for Plagioclase, Oxide and Clinopyroxene crystals, and the glass from samples 1, 3, 4 and 7.

The anorthite content of plagioclase varied a little across different crystals, but there was no apparent systematic variation across different quench temperatures or experimental conditions. The X_{An} values given in these analyses fit into the range of compositions in the natural BGP samples (An_{49-65}, see Chapter 4). The plagioclase composition is also similar to that predicted by MELTS for crystals forming at 1140ºC (An_{61-72}, see Chapter 3.1.3).

The results of these experiments have been thoroughly examined here, with a focus on crystal size, growth rate, and aspect ratio and the relationship of those factors with the cooling histories and growth conditions of the samples. The next chapter will examine and discuss what these relationships and behaviours can teach us about crystal growths, and how new knowledge gained through this study can help to better understand the cooling and growth histories of igneous and plutonic rocks.

6. Discussion

In nature, lavas may have substantially different crystal characteristics from one another at different distances from cooling surfaces, a feature that is evidenced and observed in the BGP (Chapter 4). Similarly, in experimental work, changes in temperature and cooling rate result in associated changes in the observed crystal characteristics such as size and aspect ratio. Therefore, it is clear that both cooling rate and the absolute temperatures involved in the growth of crystals are key controls of crystal characteristics. This multifacetted investigation of crystallisation from a natural melt has led to a range of observations, resulting in a relatively complete characterisation of crystal growth. In this chapter, these observations on crystal growth and characteristics will be reviewed, interpreted and discussed in a wider context within pre-existing work and knowledge.

6.1 General Crystal and Sample Characteristics

Before examining the details of the novel observations and interpretations made in this study, we will first examine how the samples produced from these experiments may be compared to the pre-experiment modelling, and to previous work on crystallisation. The characteristics of the whole sample after quenching can be directly compared to the predictions made in the MELTS modelling that was used to plan the experiments.

Plagioclase crystallinity in the experimental samples was one such factor predicted by MELTS. A comparison of the MELTS predicted crystallinity with the actual measured quenched sample crystallinities is presented in Table 26 below (these figures are reported in chapter 5.3 and 3.1). For experiments 3 and 6 these figures are reasonably close, but for many of these experiments there is a significant difference between the predicted and actual quantity of plagioclase in the samples. This may be because the MELTS software does not take into account the kinetics of

crystallisation and the complex nature of the changing temperature over time. Thermogravimetric analysis would enable us to predict equilibrium crystallinity with more accuracy, which could be a valuable future contribution e.g. Applegarth et al., 2013b; Biren et al., 2020.

Run	Predicted Plagioclase Crystallinity at Quench T	Quenched Sample Plagioclase Crystallinity	Predicted Total Crystallinity at Quench T	Quenched Sample Total Crystallinity
1	9 - 10%	14.0%	24 - 38%	15.9%
2	9 - 10%	7.0%	24 - 38%	7.0%
3	9 - 10%	6.7%	24 - 38%	8.2%
4	12 - 14%	6.6%	32 - 44%	7.6%
5	12 - 14%	13.9%	32 - 44%	17.5%
6	8 - 12%	7.3%	29 - 41%	8.4%
7	9 - 10%	12.2%	24 - 38%	15.1%

Table 26. Comparison of the predicted and measured plagioclase crystallinity in the samples

There is a strong relationship between plagioclase crystallinity and total sample crystallinity, where the samples with the lower plagioclase crystallinity also had a lower overall crystallinity. Plagioclase is the most common phase within the sample across all runs. Additionally, samples in experiments with longer crystallisation times reached a higher total crystallinity. Sample 1 was a longer experiment overall, even though there were only 48 minutes spent with the sample held at temperatures below the plagioclase liquidus. In all the samples, the plagioclase crystals seem to have nucleated homogenously from the melt, evidenced by the fact that many crystals grew with no visible contact to another crystal or point of heterogeneity (Figure 28, chapter 5.2).

It is likely that being held above the liquidus temperature for longer times in experiments 1 and 3 affected the nucleation and growth of crystals. Previous experimental work carried out on plagioclase growth has included a period of time spent above the liquidus temperature in order to ensure redox equilibrium, and to give the melt time to homogenise (Pupier, 2008; Muncill and Lasaga, 1987 and 1988; Applegarth et al., 2013a, 2013b). This was not the case in terms

of the methodology in the majority of the experiments carried out in this study, and cooling was initiated after a maximum time of 3 minutes at 1180°C, with the exceptions of runs 1 and 3. Being held at these higher temperatures may have better homogenised the melt, changing the chemical properties of the melt by reducing the effect of any lasting perturbances left from previous growth in this natural sample. Additionally, it was found that for olivine, holding a sample above its liquidus temperature can result in a delay in nucleation followed by increasingly rapid growth (First et al., 2020). The first experimental run, which was held above liquidus temperatures for several minutes before cooling contained plagioclase crystals which had a more skeletal form than other runs, and a higher proportion of swallowtail crystals – particularly in the central portion of the sample. These results are consistent with a delayed nucleation and more rapid growth than expected for that cooling rate.

During the shorter experiments, it is possible that the samples did not reach equilibrium, and therefore kinetically represent quenching at higher temperatures, of around 1170-1160ºC, rather than 1150-1140ºC. This temperature is taken from MELTS predictions for the temperature at which the lower crystallinities seen in experimental samples were predicted to be reached (see Figure 79). This may have been caused by a nucleation lag.

There did not seem to be a significant change vertically through the samples, when viewed with a changing focal depth. There is unlikely to be a vertical temperature gradient within these tiny samples that is comparable to that of a BGP lava flow.

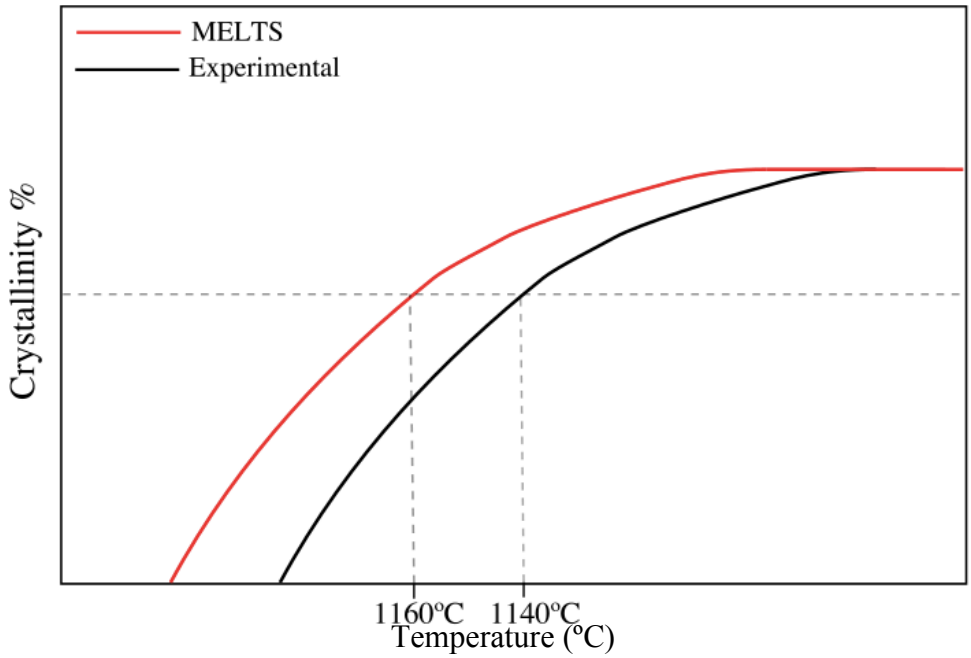

Figure 79. Schematic illustration showing time-crystallinity paths from MELTS (i.e. equilibrium) and the experimental samples. The % crystallinity reached at the experimental quench temperature here is equivalent to the crystallinity that would have been reached at a higher temperature at equilibrium.

In terms of crystal morphology, there is a pattern of growth of more skeletal morphologies, particularly visible in the clinopyroxene and oxide crystals, growing during experimental runs with faster cooling rates.

The growth of skeletal clinopyroxene crystals from plagioclase crystals in runs 1 and 6, and interstitially between plagioclase crystals in runs 5 and 7, are indicators that the clinopyroxene is likely to have heterogeneously nucleated on top of the newly grown plagioclase crystals, as well as on some of the larger pre-existing plagioclase and olivine crystals in the sample. It is possible then, to assume that clinopyroxene nucleated after plagioclase in all cases where it was observed. The order of nucleation is then oxides → plagioclase → clinopyroxene. Comparatively, the order of crystallisation in BGP suggested by Oze and Winter (2005) is chromite → olivine → plagioclase and augite, i.e. with plagioclase and augite as the final phases to crystallise out of the melt so this is in reasonably good agreement with the natural data, but the identical phases are not present. This is due to some of these crystals having been

inherited from previous cooling during stagnation, and due to different cooling rates and conditions experienced by BGP. Experiments carried out in Applegarth (2013a) saw a similar pattern to the experiments in this thesis, with plagioclase crystallising before pyroxenes.

Three of the experiments did not result in the growth of any new clinopyroxene crystals. The chemistry of the glass in these samples was similar to that of the other quenched samples, and the quench temperatures were the same as samples that had grown clinopyroxene. No new olivine or augite crystals grew from these samples. Both these phases were present in the BGP sample, but only olivine was present in crystal form in the starting material used for the experiments. Olivine is probably a relict of previous cooling and crystal growth experienced by the BGP. If the sequence of crystallisation of the different phases within the experimental samples is compared to the MELTS modelling presented earlier, it can be surmised that the conditions of these experiments were oxidising. We saw iron oxide crystals grow first, likely to be spinel, followed by plagioclase and clinopyroxene. Based on a comparison of the grown phases and the MELTS modelling, the oxygen fugacity was likely to have been above the FMQ buffer. These oxidising conditions suggest that the Nitrogen atmosphere was not effective enough in preventing oxidation in the sample.

It is unlikely that crystallisation was affected by the small amount of degassing and bubbling that occurred at the start of each experiment. As bubbling stopped in under 2 minutes in all experiments, the bubbles were all small in size, and all bubbles were lost from the melt very quickly, it is unlikely the presence of bubbles had any significant effect on crystallisation. There are few published measurements of the H_2O content of BGP, but it is likely that these samples had a water content of around 0.2 wt% (Applegarth et al., 2013a). In terms of crystal morphology, it has been shown that crystal shapes vary with undercooling in the same way regardless of whether the undercooling is caused by degassing or by temperature decrease (Shea and Hammer, 2013).

6.2 The Effect of Cooling Rate on Plagioclase Morphology and Growth

There is a clear association of cooling rate and the shapes and textures of plagioclase crystals grown in these experiments, as well as a clear trend of plagioclase growth rates with cooling rate. Cooling rate is known to be an important factor in the crystallisation of basaltic lavas (e.g. Cashman, 1993; Holness, 2014), as it controls the amount of crystallisation, so these effects are explored in detail below.

6.2.1 Plagioclase Crystal Shapes

Most of the plagioclase grown during these experiments exhibits a tabular morphology with facetted edges. The modal lengths of both the 2D imaging-based and 3D CSDslice/ ShapeCalc (Morgan and Jerram, 2006; Mangler, Personal Communications) results indicate that the 3D morphology of these crystals is a platy, tabular shape. The overall 3D shape of plagioclase crystals remained tabular for all conditions but shifted from a more platy shape towards a columnar/bladed morphology with decreasing cooling rate, as seen in Figure 57 (Chapter 5.5). In general, only experiments with average cooling rates faster than 1ºC/min exhibited growth of a significant proportion of plagioclase with swallowtail and hopper morphologies. This is in line with previous studies of plagioclase morphology and how it changes with undercooling and cooling rate, such as Lofgren (1974), and Kirkpatrick et al. (1979), who showed that the morphology evolved from tabular to acicular and skeletal to spherulitic with increasing undercooling. The faster cooling rates must have exceeded the speed at which the evolving chemistry reduces the undercooling, as the liquidus temperature decreases as the melt is depleted (see Chapter 2.2.1; Loomis, 1981), thereby resulting in a late growth of these more irregular morphologies of plagioclase.

The generally tabular morphologies of these crystals indicate growth in the interface controlled regime, with minor evidence for some diffusion-limited growth in experiments with faster cooling rates (resulting in swallowtail and hopper crystals). Delayed nucleation resulting in faster growth rates in the first experimental run also indicates growth slipping into a diffusion-limited regime (see chapter 5.3). Within an interface controlled growth regime there are several possible growth processes by which atoms and groups of atoms may attach themselves to the crystal surface such as continuous growth, screw dislocation or surface nucleation (Kirkpatrick 1975, 1981), but these are not distinguishable with the data available in this study.

6.2.2 Plagioclase 2D Aspect Ratios

Studying the 2D aspect ratio of crystals is an important indicator of their 3D shape, since the modal 2D aspect ratio of crystals is equivalent to the ratio of their short and intermediate axes (Higgins, 1994). Additionally, crystals that have higher aspect ratios interact more readily with other crystals during flow, resulting in shear thickening, changing the lava rheology, which is an important factor controlling eruptive behaviour (Chevrel et al., 2013). From the experiments carried out in this study, it was possible to image and measure the 2D aspect ratio of hundreds of plagioclase crystals in each sample. The low undercoolings of these experiments were maintained by using slow cooling rates, allowing the undercooling to stay low since the evolving melt composition reduces the liquidus temperature as crystals grow from the melt (see chapter 2.2.1). This meant that the transport of chemical species in the melt phase was able to occur fast enough so that it did not limit the growth of crystals, meaning that the growth rate limiting factor was the rate of attachment of chemical species to the crystal interface. The majority of crystals therefore grew within the interface controlled regime, which is characterised by the facetted tabular plagioclase morphologies seen in the majority of newly grown plagioclase (Lofgren, 1974; Holness, 2014).

The profile of the aspect ratio frequency plots was similar for all experiments, with the exception of runs 1 and 3, which may have been affected by being held above the liquidus for longer pre-cooling (Figure 47, Chapter 5.4). In nature, there is a clear difference between crystals grown at significantly different cooling rates, for example, how plagioclase phenocrysts (grown with very slow cooling rates) are often more equant than the plagioclase in the groundmass of extrusive igneous rocks (grown with a much faster cooling rate) (Holness, 2014; Higgins 1996). Within the BGP, Oze and Winter (2005) calculate cooling rates that vary from 267 – 0.52 ºC/min, dependent on depth; this variation is reflected in the crystal sizes and morphologies seen at different depths into the lava flow – highly glassy with few new growths in the top cm, that then grades into highly crystalline lava (see Figure 22). Even slower cooling rates would have been experienced by the relict plagioclase and olivine phenocrysts found in this lava. It may be that, in this case, keeping growth within an interface controlled regime at low undercooling reduced the probability of any significant difference in aspect ratio with the changing cooling rate. However, when the aspect ratios are plotted against their cooling times, and the data from this work are compared with a larger dataset of naturally grown plagioclase crystals from Holness (2014), we see that the cluster of data from this study is consistent with the broader negative correlation between mean 2D aspect ratio and cooling/crystallisation time (Figure 50, chapter 5.4). This expands on the range of cooling timescales used in the Holness (2014) dataset, showing that the relationship proposed by Holness - where crystallisation time can be calculated as a function of aspect ratio - may extend to much shorter cooling times than those investigated in the original work. These observations also suggest that if experiments had been performed with a wider range of cooling rates, it is likely that there would have been a stronger correlation seen between cooling rate and aspect ratio, as well as crystallinity.

The fact that the data from these experiments fits well into a pattern shown from natural datasets is an indicator that the experimental data are directly comparable to naturally grown

crystals and lava. Furthermore, it was observed that a larger proportion of longer, skeletal crystals grew in the experiments (e.g. Run 1) that had a longer overall cooling time, which sits well with natural observations.

The way that 2D mean crystal aspect ratio changed during the experimental cooling time was tracked via images taken during the heating stage experiments. For each individually tracked crystal, there was little-to-no apparent change in its 2D aspect ratio over the time it was tracked. However, when a larger population of crystals growing in one specific region of the sample was tracked over time, both the mean and the modal 2D aspect ratio appeared to increase over time, over the course of 128 minutes (see Figure 53, Chapter 5.4). From visual observations made during these experiments, it was seen that the crystals grew primarily in the length direction, and once they impinged there was very little growth of their width. This is similar to the experimental observations made by Applegarth et al. (2013a) who observe that plagioclase crystals grew fastest in their long-axis direction, and that crystal growth rates were apparently slowed by impingement. Aspect ratio would generally be expected to decrease over time (Pupier et al., 2008; Applegarth et al., 2013a), since once growth in the faster direction (length) slows or stops, growth continues in the slower direction (width), thereby decreasing the crystal aspect ratio (Figure 80). Crystal growth slows to a stop as one end of the crystal approaches another crystal surface. This effect was seen in run 6, where two of the tracked crystals were impinged on either end, effectively halting any visible progress in the growth of the crystal length. It is expected that at this point, the crystal would continue to grow in the directions of its free surfaces – in this case that would have caused visible growth of the crystal width in 2D. Figure 79, below, illustrates the expected effect. In the case of the tracked crystals seen in run 6, as well as those grown in other experiments, the growth of the crystals' width was so slow and small that no significant growth was recorded, within uncertainty. It is likely that, given enough time, and with a maintained low undercooling, the crystals would have started to fill

out in width. It is also possible that the sample had reached its equilibrium crystallinity before the quench temperature, resulting in little to no further measurable plagioclase growth as undercooling had effectively become zero.

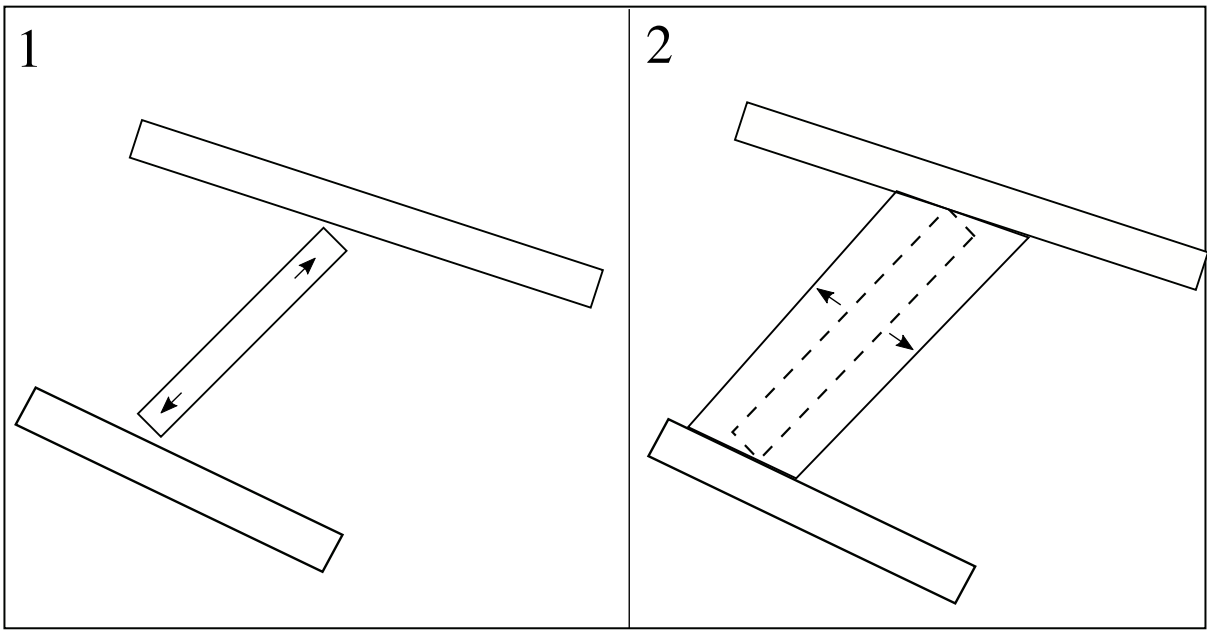

Figure 80. 1. Illustration of a growing crystal that collides with 2 neighbours, effectively preventing its continued growth in the length direction. 2. The crystal then begins to expand in its width-direction.

This could have been due to the relatively short crystallisation time allowed for these crystals to grow, whilst the growth rate of the crystal width was around 10 times slower than the growth rate of their length. This slow rate may have been too slow in the given time to grow substantially enough to be measured. Another possibility is that growth could have been limited by space and available components in the sample. If pore space between several impinging crystals was limited, this could also reduce the growth in the width direction after the crystal length stopped propagating (Holness et al., 2012). The change in aspect ratio of the tracked individual crystals did not seem to be affected by the cooling rate or temperature at which the crystals grew. There is also the element of measurement uncertainty to consider, where the width measurements had a significantly higher relative uncertainty due to their small size, possibly making it seem as if the widths were not changing.

6.2.3 Comparison to Plagioclase in Natural BGP

	Mean AR	Modal AR	Plagioclase%	Morphology
BGP	9.6	9	4%	Generally tabular, with a population of swallow-tailed crystals
Experimental	6-9.5	5-13	2-14%	Mostly acicular-tabular, some swallowtail and hopper crystals.

Table 27. Comparison of plagioclase features between natural BGP and experimental measurements.

Both the plagioclase in BGP and in the experiments carried out in this study had facetted, tabular shapes as their most common morphologies. The modal aspect ratio of the plagioclase in BGP, however, was slightly higher than the modal aspect ratios of the experimentally grown plagioclase in most runs (Table 27). The experimentally grown plagioclase appeared closer to a euhedral/square shape, even in crystals with swallowtail like morphologies, and exhibited some hopper morphologies, which were not observed in BGP. The tabular morphologies of plagioclase seen in BGP have been interpreted as those of plagioclase crystals that grew in slower cooling lava that was stagnant for a period before extrusion, whilst the swallowtail morphology crystals grew in the faster cooling rate conditions post-eruption (Self et al., 1998; Swanson 1973; Oze and Winter, 2005). Some of the more irregular shaped plagioclases in the BGP were significantly more skeletal than those grown in these experiments, indicating growth at an even lower undercooling (Figure 81). The BGP image shown below is taken from a couple of centimetres depth into the BGP, still towards the upper margin of the lava flow.

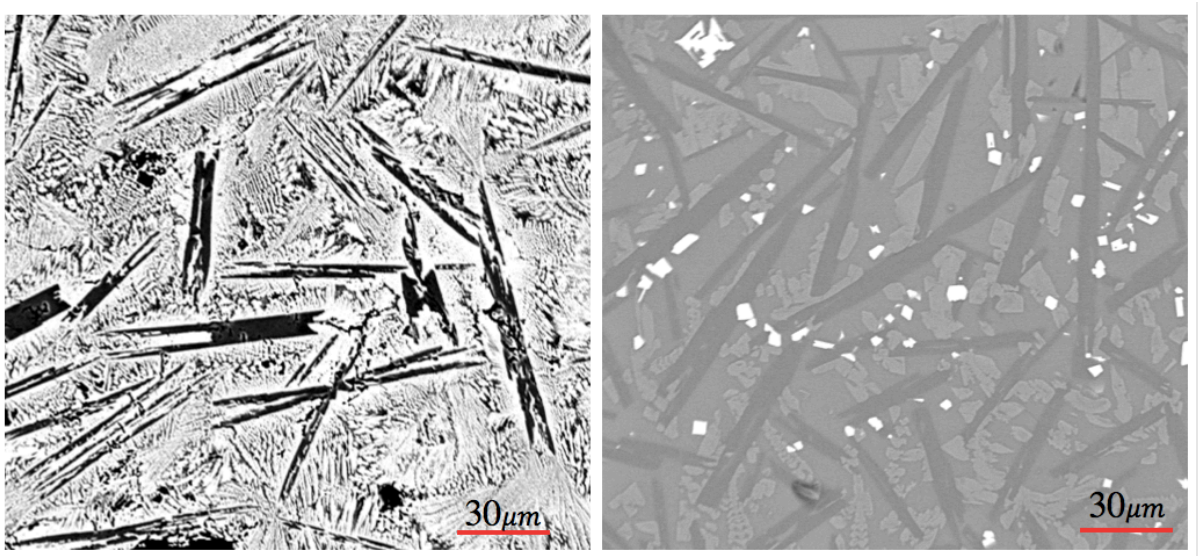

Figure 81. Comparison of swallowtailed plagioclase crystals ~2cm deep into the BGP sample (left) and run 1 (right)

The corner growths observed on the BGP plagioclase and olivine crystals (Figure 17C, Chapter 4.3) are also likely to be indicators of a change in cooling rate. This is consistent with the lack of corner growths on experimentally grown plagioclase, since there were no sudden large changes in cooling rate or temperature during the experiments. Lofgren (1974) and Shea and Hammer (2013) have shown that plagioclase morphology is dependent on the total effective undercooling at the time of growth, so it is likely that the more skeletal and disequilibrium shapes seen in the experimental samples were grown at the lower temperature stages of the experimental runs (not directly observed). The measured cooling rate of BGP toes, where cooling rate is measured at 2ºC/sec (Hon et al., 1993), is significantly faster than the experimental cooling rate, which helps explain the increasingly dendritic swallowtail crystals seen in the BGP that are not present in the experimental samples.

There is a difference between the nucleation style for plagioclase in BGP and in these experiments. The BGP plagioclase generally nucleates heterogeneously (Oze and Winter, 2005), with textures indicating growth of plagioclase from the seeds of existing plagioclase and other crystal phases, such as olivine. The plagioclase in the experimental samples appeared

to have nucleated homogenously, growing straight from the melt. A higher undercooling is needed for homogenous nucleation than heterogeneous (Gibb, 1974; Pupier et al., 2008).

The plagioclase in BGP had some crystals that were significantly less anorthitic than those grown experimentally, but on average both the BGP and experimentally grown plagioclase crystals had a similar anorthite content. Both are consistent with the MELTS predictions, which have plagioclase grown at 1140ºC growing with the composition An_{60-63}, while BGP plagioclase has an average composition of An_{60} and the experimental plagioclase had an average composition of An_{65}.

6.3 Plagioclase Growth Rates

6.3.1 Mean Plagioclase Growth Rates

The mean plagioclase length growth rates calculated from the bulk quenched samples in these experiments were in the range 10^{-8} – 10^{-11} m/s. These experimental bulk average growth rates are similar to the results reported from experiments held in similar conditions, such as Pupier (2008) and Schiavi et al. (2010), who reported growth rates of the order 10^{-9}-10^{-11}m/s measured from cooling experiments carried out on basaltic material very low cooling rates (0 – 0.05 ºC/min). They are also similar to the growth rates measured by Applegarth (2013a; $5x10^{-8}$ – $1.7x10^{-7}$m/s), who use the same starting material and similar apparatus. These growth rates are an order of magnitude smaller than those calculated for the Makaopuhi Lava Lake, Hawaii (1-$11x10^{-12}$m/s; Kirkpatrick, 1977), but are of the same order of magnitude as those calculated from CSD data for the upper 3.5cm of BGP ($2x10^{-7}$ – $9 x10^{-10}$); Oze and Winter (2005) which was cooled at 11 – 2°C/min (Chapter 3.1.4, Oze and Winter (2005)). It is surmised that the

experimental growth rates are realistic compared to the growth rates previously observed for basaltic lava flows.

Growth rates have been shown previously to have a strong relationship with cooling rate (e.g. Cashman, 1993). In the data from these experiments, there was a very clear trend of growth rate increasing with increasing cooling rate (Figure 60, Chapter 5.6). This is in line with observations made by Cashman (1993), which were based on natural data. The results from SEM data had a stronger correlation between cooling rate and growth rate than those taken from optical microscope data (R^2 values of 0.8 for SEM and 0.5 for microscope measurements (Chapter 5.6)). Almost all the experiments were held at very similar temperature ranges (1180 – 1140ºC), and with the same starting material. This indicates that cooling rate may be a more important factor controlling average crystal growth rate than just the absolute temperatures. We have seen from the thermal models described in chapter 3 that cooling rate of lava is dependent on several factors, including atmospheric cooling, and factors that are intrinsic to the lava itself such as rate of conduction. It can be deduced that the crystallisation and growth rates of plagioclase within basalts is heavily dependent on the temperature conditions in which it is erupted; and not only the temperature but also the rate of cooling experienced.

6.3.2 Observed Real-Time Crystal Growth

The most common way for the growth rate of crystals to be calculated is to divide a crystal size parameter by a known, measured or calculated crystallisation time. This approach assumes that the growth rate of a crystal growing from melt is constant from nucleation to the end of cooling. Previous work, such as that of Applegarth et al., (2013a) has shown that this is not likely to be the case with most plagioclase crystals. To get a better understanding of how these growth rates may change over time, the experiments in this study involved recording the growth of

individual crystals in a cooling melt. The advantage that we have from these experiments is that we know exactly the length of time which the sample spent below the liquidus, and we have observations on the growth of crystals. This helps to ensure a better estimate of the average growth rate of a crystal. However, it is possible to further refine these growth rates and observations using data gathered from individually tracked crystals grown in these experiments.

One of the key observations made from the results of these experiments was that crystal growth rates for length were not constant over time for individual growing crystals in a melt. All the individually tracked crystals exhibited the same general pattern, a faster initial growth rate was seen just after the point where the crystals were large enough to be observed and measured, which then decayed over time until slowing to zero (Figures 52-78, Chapter 5.6). The crystals did not all stop growing at the same point in time, or at the same temperature. There are several possible causes of crystal growth rate decrease and pausing. From direct visual observations of the growth, it was clear that crystals began to collide and impinge on one another – the time at which they impinge on another crystal at one or both ends coincided directly with the slowing or stopping of growth of that crystal length. Crystals which were in contact with another crystal at both ends stopped growing completely, while some crystals which were only impinging on another crystal at one end continued to grow slowly. The observation of a slowing growth rate being apparently caused by impingement was also described by Applegarth et al. (2013a) in their direct observations of crystal growth.

In the growth direction, the width of crystals changed very little over time once an initial crystal morphology had been established. Overall visible crystal growth may slow down due to a physical limit or lack of space, or an increase in melt viscosity as the temperature decreased and melt composition evolved. An increase in melt viscosity would also slow down transport

of components to the crystal, and possibly push crystal growth into the diffusion limited regime, which we see evidence for in the swallow-tail and skeletal crystal forms.

The patterns within these results are consistent with previously made direct experimental observations, such as those of Applegarth et al. (2013a), who performed similar heating stage experiments, using Kilauean basalt samples.

6.3.3 Temporal changes in crystal Aspect Ratio

Aspect ratio of crystals is expected to decrease over time since as growth in the length direction slows or stops, crystal growth in the width direction becomes the most important and the crystal widens (see Figure 80). Aspect ratios calculated from the tracked crystals showed little-to-no change, within the uncertainty, over the time the crystals were growing. When accounting for the possible error of the measurements that were used to calculate aspect ratio change over time for these crystals, most of the aspect ratios seemed not to have changed at all (Figure 52, Chapter 5.4). The continuing growth of crystal lengths and lack of width growth would eventually lead to higher aspect ratios and more acicular morphologies. It may be that growth in the width direction was so slow during this time (around 10 times slower than the length growth rates) that it was not possible to detect a significant change in width.

It is possible that, had the crystals been left to continue growing without quenching, that the widths would have had time to increase more substantially. Applegarth et al. (2013a) finds that growth in the length of the crystal was initially the most rapid, but eventually slows and growth of the crystal width starts to become more significant – this was not observed in these experiments. There are several possible reasons for this lack of change in the aspect ratio – for example, there may not have been enough time given for the slower growth rate in the width direction to produce any measurable growth, or it is possible that equilibrium was reached,

effectively giving an undercooling of zero, and therefore no driving force for further growth was being provided.

6.4 Gaining a Better Understanding of Crystal Growth

Being able to directly observe the crystals in these experiments has allowed us to gain a better understanding of the shapes and textures formed as they grow, when crystals start and stop growing, and how they interact with each other and behave during their growth within the melt. In realistic situations, such as during a natural lava flow, we are not able to directly observe crystal growth in such a way. It has previously been assumed that the total cooling time is equivalent to the total crystallisation time in basalts (Cashman, 1993). This may not always be the case; therefore, it is worthwhile to use the observations from these experiments, as well as other modelling techniques in order to better understand lava flows from the erupted products. To further explore the kinetics of this system, two different models on crystallisation were used in conjunction with each other and their usefulness evaluated in modelling nucleation rates and crystallisation time. The first model used is described in Mollard et al. (2020). This model was developed in order to compare experimental results to classical nucleation theory. It assumes that the activation energy of atomic jumps across the nucleus – surface interface is equivalent to the shear relaxation time of the melt (Stokes-Einstein approximation), which allow the activation energy required for atom attachment to be expressed in terms of melt viscosity. It also assumes that the heat capacities of the crystals and the melt are comparable. This model for the rate of a steady-state, homogenous nucleation is expressed in equation 8.

$$I = \left[\frac{N_C K_B T}{3\pi {a_o}^3 \eta}\right] \exp\left[-\frac{16\pi\sigma^3 {T_L}^2 {V_m}^2}{3\Delta H^2 {\Delta T_{eff}}^2 K_B T}\right] \quad (8)$$

Where N_c is the volumetric concentration of reactive atoms (computed as Avogadro's Number/ volume) (m^{-3}), K_B is the Boltzmann constant, T is the absolute temperature (K), a_o is the atomic jump distance (m), η is the viscosity (Pa.S), σ is the free energy associated with the crystal—

melt interface (Jm^{-2}), which is assumed to be isotropic, T_L is the liquidus temperature (K), V_m is the molar volume (m^3mol^{-1}), ΔT is the undercooling (K), and ΔH is the enthalpy of formation (J/mol).

This equation was used to find a modelled value for *I*, the nucleation rate. First, the values used in the paper in which this model was presented were used to ensure that the method produced equivalent values to those published (Mollard et al., 2020). After this, the model was implemented using values that were appropriate for the properties of BGP. Viscosity was calculated using the model provided in Giordano et al. (2008), using the composition in Table 9 and assuming zero H_2O content. A series of similar values for enthalpies of formation for An_{65} (the average composition of the experimentally grown plagioclase) are given in Ludington (1979), and a rounded value was chosen for these calculations. The molar volume was calculated using methods described in White, 2020 and available geochemical data. The values used in equation 8 that are not immediately available are shown in Table 28.

Property	**Value**
ΔH (J/mol)	110,000
V_m (m^3/mol)	103.6
a_0 (m)	$1.4x10^{-10}$
$\boldsymbol{\eta}$ (Pa.S)	79.43
T_L (K)	1453

Table 28. Values used in calculations with equation 8.

The nucleation rate, *I*, is the population density of crystals formed per second. Therefore, if we assume that the nucleation in these experiments is near-instantaneous (crystals nucleate within the first seconds of cooling), which is supported by visual observations during the experimental runs, then we can assume that the value of *I* is equivalent to the value of the observed the crystal population density (Nv) (Table 19, Chapter 5.5), if all nuclei formed within 1 second. From

this, a comparison can be made between the calculated and measured numbers. The value for σ has historically been difficult to constrain (Mollard et al., 2020), and a tiny relative change (+/- 0.001 Jm^{-2}) in the value can significantly alter the calculated value of *I* (see Figure 82). A value of σ was back-calculated using the measured Nv values for different undercoolings, and this value was chosen for an approximate σ (0.0142 Jm^{-2}), for an undercooling of 10°C that was relevant to these experiments. This value is also consistent with the σ values shown in Mollard et al. (2020; their figure 2).

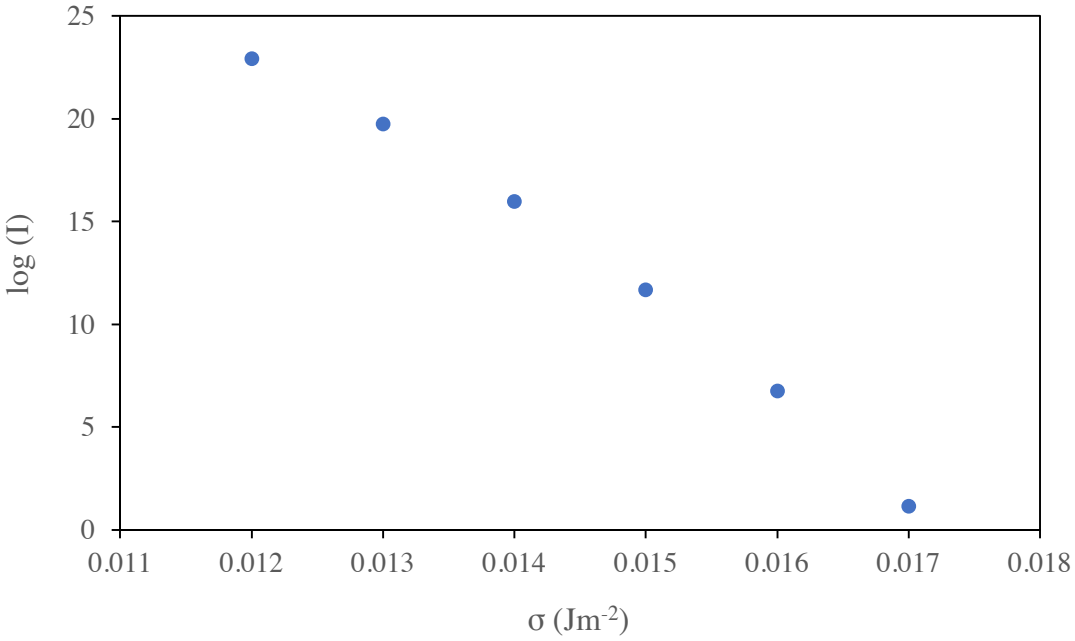

Figure 82. log (I) vs σ values

A value of $I = 1.47 \times 10^{15}$ $cm^{-3}s^{-1}$ was calculated from equation 8 using σ = 0.0142 Jm^{-2}, at 10°C of undercooling. This is within the range of the measured experimental values of Nv, which were converted to a 3D measurement from 2D data using CSDCorrections (Higgins, 2000), of $3.3 \times 10^{14} – 5.8 \times 10^{15}$ cm^{-3} (see Table 19, chapter 5.5). Limitations on this method include that it is based on spherical particles and becomes increasingly complex to implement in any situation where nucleation rate is not constant or instantaneous. In igneous rocks, instantaneous nucleation produces crystals of roughly the same size (assuming growth rate is the same or

similar across the population), whilst constant nucleation results in a large range of crystal sizes as crystals begin growing at different times. When direct observations of crystals are possible, we can see these changes in real time. The experiments here had tabular particles that became more elongate over time and experimental observations of growing crystal populations suggest that nucleation is likely to have happened near-instantaneously.

Modelled or measured values of nucleation rate can then be used with the Avrami model (1939, 1941) (equation 9 – equivalent to equation 1). This equation models the changing crystal fraction over time for a given constant or instantaneous growth rate. It also assumes random, homogenous crystal growth, which is close to how the plagioclase in these experiments nucleated. In this model, there are a certain possible number of nucleus embryos which are exhausted over time as crystals grow. There are two limiting forms of the equation – one where the exponent, m=4, and another where m =3. m=4 applies to a situation in which there are a large number of nuclei and nucleation is constant over time. m=3 applies where all the possible nucleation points are exhausted early, and nucleation happens very quickly, or instantaneously (Zanotto, 1996). It is possible that there are situations in which an intermediate number can be used, or possibly a number outside of these limits (Zanotto and Galhardi, 1988). In this case an m of 3 was chosen, for a calculation that assumes an instantaneous nucleation (Cashman, 1993).

$$\emptyset = 1 - \exp\left(k_v I Y^3 t^m\right) \quad (9)$$

Where $\emptyset$ is the crystal fraction, k_v is a volumetric shape constant (in this case $4\frac{\pi}{3}$ for spherical grains, Zanotto, 1996), Y is the growth rate, t is time and *m* is an exponent.

Figure 82, below, shows how crystal fraction varies with time using the modelled and measured *I* and Y (using the average observed growth rate from tracked crystal growth) and Equation 9 above, with m=4. The modelled ∅ asymptotes to 1, so the calculated value for an "end" time is taken from when the model reaches a value close to 0.99.

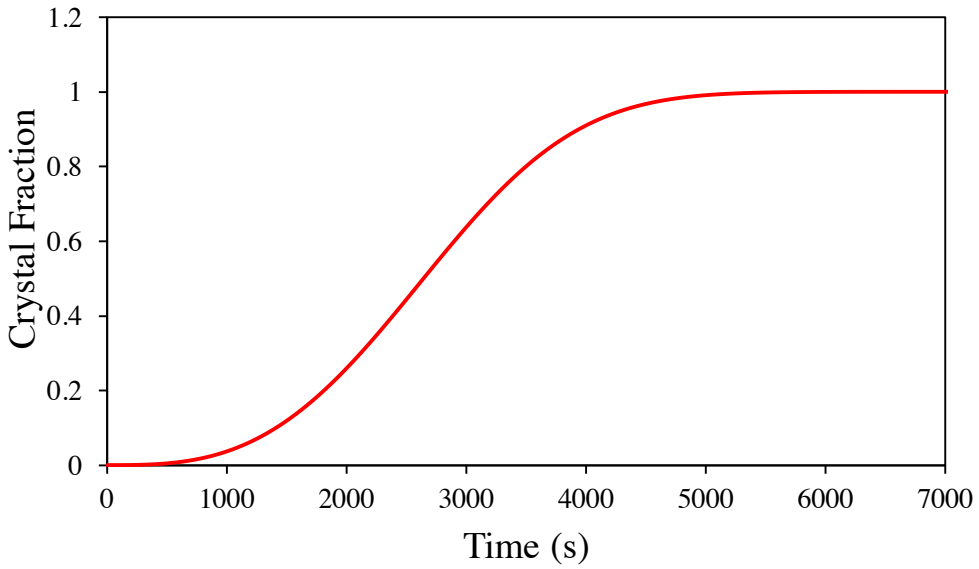

Figure 83. Avrami model using the measured I and Y values from the sixth experimental run. (I =2.6x1015m3/s, Y=1.5x107cm/s)

This model suggests that crystallisation approaches a maximum after ~5000 seconds, whilst the time used to calculate the bulk mean growth rates in these experiments was 8640s. There is a clear difference in these two timings, with the time used as the crystallisation time being longer than the modelled time for crystal fraction reaching a maximum. This difference (where the modelled timing is shorter than that used for calculations) is consistent across all the experimental runs when the measured values for each run was input into the model. Although, the modelled times always remain at a similar magnitude to the measured crystallisation time. Measurements of the tracked crystals over the 8640s indicate that whilst growth had slowed, crystals did continue to grow in the sample.

As the growth rate, time and Nv were measured independently, from experimental data, we can use this model to calculate a better estimate for the nucleation rate. An instantaneous or

near-instantaneous nucleation rate (m=3) that would result in timing that is similar to the experimentally observed crystal growth time was calculated as $I = 1.8x10^{15}$ $m^{-3}s^{-1}$, which is close to half of the measured Nv. Figure 84 below shows the original and 'corrected' Avrami functions for the 6th experimental run.

To find this nucleation rate using equation 8, it would require an input σ value of 0.0141788 Jm^{-2}. To get an accurate/specific match of σ and *I*, the σ value had to be calculated to a large number of decimal places, which highlights how difficult to constrain the value is.

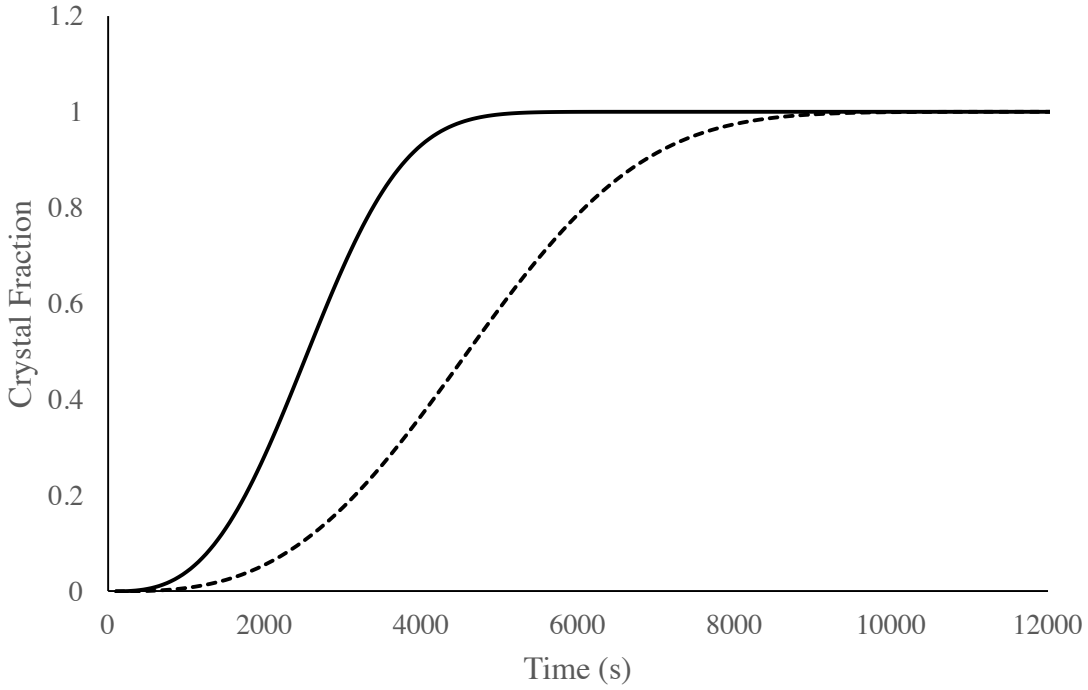

Figure 84. Avrami function calculated using the measured Y and Nv (I=2.6x10⁻⁵) for run 6 (solid line), and the same conditions but with a I recalculated and 'corrected' for the measured timescale of the experiment (I=1.8x10⁻⁵) (dashed line).

To gain a better understanding of the usefulness of the model, we can also investigate how changing some of the parameters affects the output of the Avrami function. Changing the input growth rate into the Avrami function can have a large effect on the timescale of crystallisation predicted by the model. Figure 85 below shows the Avrami function curve for different growth rates, which double in each instance, with m=3. As expected, the slower growth rates yield the slowest crystallisation times.

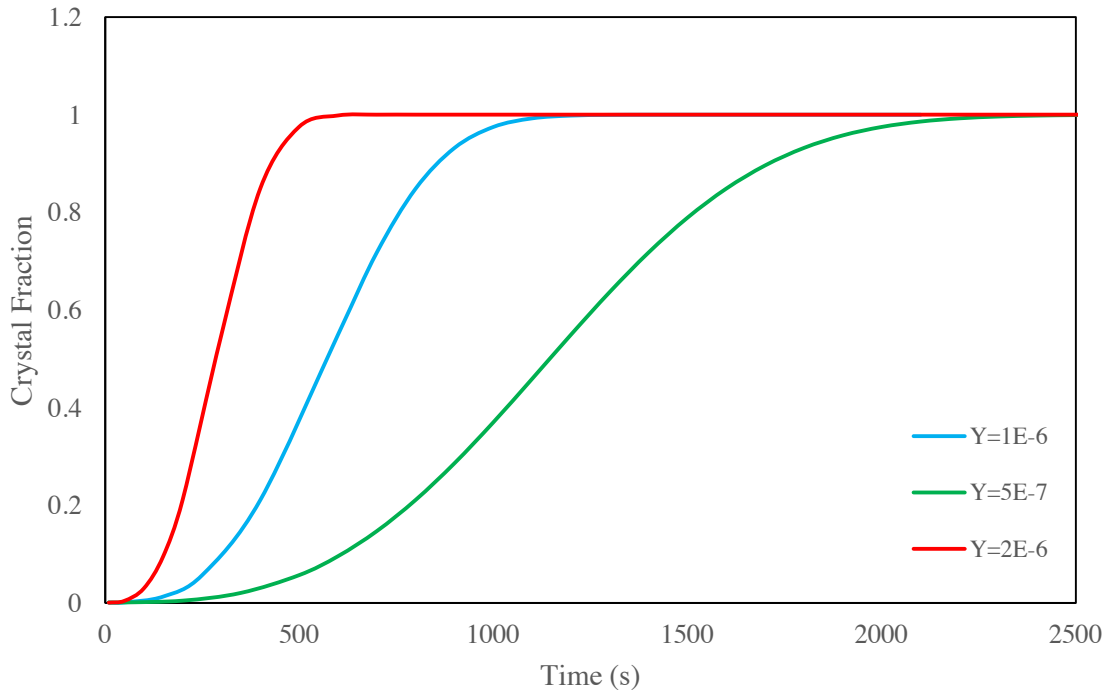

Figure 85. Avrami function calculated for different growth rates, with the same nucleation rate (I=2.6x1015m3/s)

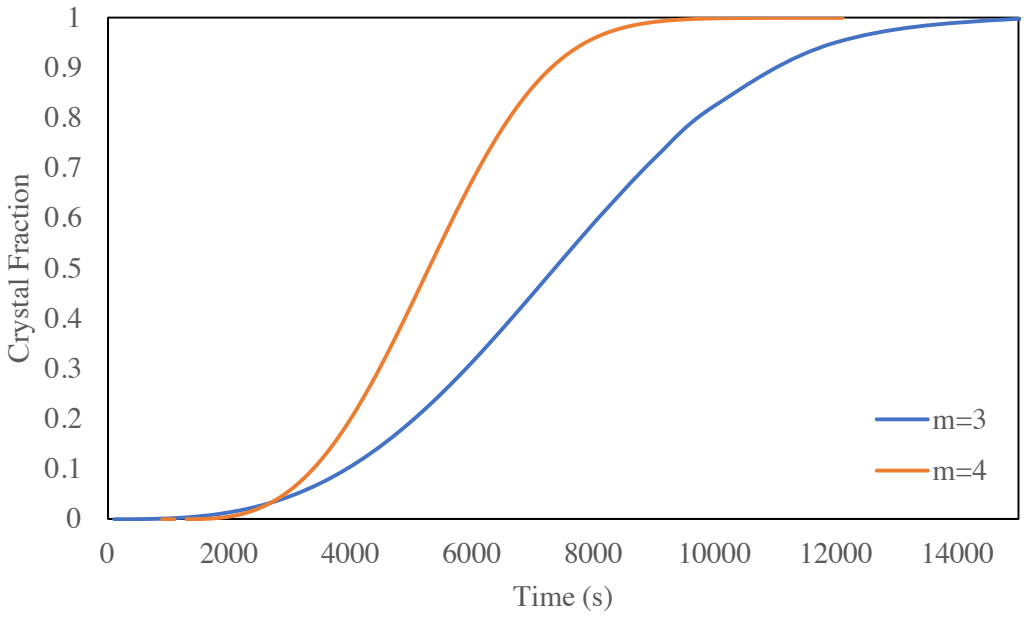

Figure 86. Avrami function calculated for the two different limiting forms, m=3 or 4, with all other inputs kept the same (I=1.6x10⁶m³/s, Y=2.2x10⁻⁶cm/s).

Figure 86 shows the difference between m=3 and m = 4 for the same nucleation rate and growth rate parameters. Having a constant nucleation rate shortens the time taken to reach a maximum crystallinity, which is logical since a continuous increase in the number of crystals increases

the crystallinity as well as just the growth of existing crystals. It is likely that within these experiments, the real situation of crystal growth transitions over time from m=3 to m=4.

The causes of differences between measured and modelled crystallisation timescales could lie in the assumptions in and limitations of this model. The Avrami model assumes that the crystals are a spherical shape, which is expressed in the volumetric shape factor. Furthermore, it is assumed that crystal growth rate is constant, which the results from this thesis show that it is not. We have also worked on the basis of an instantaneous nucleation, which fits reasonably well with visual observations made in the experiments but is unlikely to be truly instantaneous (complete within 1 second). The model also does not take into consideration that there may be a crystallisation limit caused by crystal packing, in which case a limit would be reached before the predicted value. The model also takes into consideration growth of only 1 phase, whilst realistically different mineral phases are likely to have different growth rates. Further work on refining this method would be helpful in order to constrain crystal growth in a more accurate way.

It is likely that in most cases growth in the experimental runs had slowed to a near stop before the point that the samples were quenched. This was observed in a lack of significant visible growth in samples after dropping below 1150°C, which led to the chosen quench temperature of 1150 - 1140°C for the experiments. Had the samples been held at a low undercooling even longer than the experimental times, it is likely that there would have been very minimal growth, but the calculated growth rates would have been much slower if the total cooling time was taken as crystallisation time. The Avrami model used in this way helps to check the

crystallisation time used in these calculations. It is therefore essential to the continued study of crystal growth rates to have better constraint on the true 'crystallisation time' of crystals.

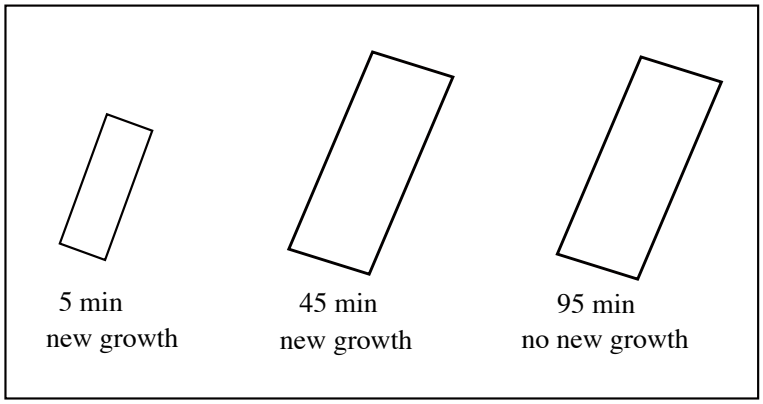

Figure 87. Schematic sketch showing how if crystals are left to cool slowly after the end of the 'true crystal growth time', there would be little to no further growth, but the measured or calculated cooling time would continue to increase, and therefore would yield an inaccurate growth rate if used instead of the crystal growth time.

6.5. Project Strengths and Limitations

This project allowed me to make direct observations of crystals growing from a natural lava as they grew, with microscope lens magnifications that were sufficient to allow reasonably precise measurements to be made. Large datasets were able to be obtained of hundreds of crystal measurements taken from each sample, and a variety of different data analysis methods were carried out in order to fully characterise both the natural BGP starting material as well as the experimental samples both before, during and after experimental runs. A multi-facetted approach allowed me to explore several different aspects of crystal growth and the preliminary modelling work allowed comparisons to be made between the modelled and experimental results. From comparisons with models, previous experimental work, and results from previous work on natural basalt lavas, we see that the results from these experiments seem to align well with the existing data, and therefore are applicable to real volcanic environments.

On the other hand, some data gathering and analysis was limited by the oxide formation which unfortunately was a product of working with an Fe-rich material. Camera resolution and magnification of the images at times prevented crystals from being measured, since the crystal shape boundaries were sometimes difficult to delineate. Furthermore, this study only investigated relatively short timescales, and only one material was used in the experiments.

Overall, the results from this study have allowed us to thoroughly review how crystal growth rates and morphologies are affected by cooling rate and timescales. We have also been able to compare different tools for predicting crystal 3D shapes from 2D data, which will have future implications on CSD studies. Making direct, real-time observations of plagioclase growth has also allowed us to get a better understanding of the timings of crystal growth within lava, as well as the growth behaviour and interactions of crystals during cooling. The findings of this study have several implications on future investigations of crystal growth rates and morphologies. These are discussed in detail in the following chapter.

7. Implications

The results of this thesis have a direct impact on our understanding of lava flows and the future interpretation of eruptive products. Understanding how crystals grow in a lava flow can help model and predict the behaviour of lava flows during volcanic eruptions, which in turn can contribute to better hazard management.

As lava flows and cools, its rheology changes over time as the temperature decreases and an increasingly larger proportion of the melt crystallises; the way that the crystals grow within this melt then has a further control on how the lava rheology is changed. Crystallisation affects the rheology of lava in several ways: the growth of crystals can cause it to get thicker and jam together as they grow, the timing of which is in part controlled by the crystal aspect ratio and cooling rate (Liu et al., 2017 – who predict a packing density of 0.55 for cuboids with an aspect ratio of 6). Cooling rate is a control on the degree of undercooling experienced by the crystal, and thus on the crystal growth rate. Higher undercooling and faster cooling rates lead to more skeletal, higher aspect ratio crystals growing at faster rates, which then exacerbate the effects of crystal interactions. This is particularly significant in the case of lava flows which have developed a crust, such as the tubes in which BGP often flows through, as the insulating effect of crusts allows these lavas to have increased mobility, and the impact of crystal content and shape on the rheology of these lavas becomes important in determining the morphology and emplacement of the lavas. Furthermore, crystal growth causes the chemistry of the molten lava to evolve over time as crystals grow from the melt and deplete it, changing its viscosity (Chevrel et al., 2013). Understanding how temperatures and cooling rates affect crystal growth rates and morphologies is important since it allows us to work backwards from cooled igneous rocks, gaining a better understanding of their cooling histories from the crystals in the rock. The results from these experiments are most relevant to basaltic lava flows in and beyond

Hawai'i, but can be extrapolated for general growth of plagioclase in any magmatic or volcanic environment.

The relationship between 2D crystal aspect ratio (which is equivalent to the short/ intermediate ratio of 3D crystal axes) with cooling time/ cooling rate has previously been explored in detail by Holness (2014). Nevertheless, the current study has allowed a further exploration of the relationship, particularly in a setting with a much faster cooling rate and shorter crystallisation time, though still with primarily interface-controlled growth. The relationship proposed by Holness (2014) indicates that "crystallisation time" can be found as a function of the plagioclase aspect ratio, where crystallisation time refers to the timescale of crystal growth. The crystallisation time used in Holness (2014) was derived from a 1D thermal diffusion model, which assumes purely conductive heat transfer and an intrusion temperature with a cooling interval of 1200-1000ºC. It is also assumed that the cooling time of a magmatic intrusion is equivalent to the crystallisation time. In this thesis, this relationship has been experimentally tested and it has been shown that this relationship may extend to these shorter timescales as appropriate to fast cooling lava flows and other extrusive products. With this relationship, measurements of crystal aspect ratios taken from cooled eruptive products can be used to work backwards and calculate a good estimate of crystallisation time in a more direct and simple way than previously. This could lead to a more efficient interpretation of volcanic eruption processes.

Further to this, this work has also made contributions to the understanding of interpreting the 3D shapes of crystals from their 2D sections or projections. Previously commonly used spreadsheets such as CSDSlice (Morgan and Jerram, 2006) can sometimes provide results that do not accurately represent the actual 3D crystal shape, whereas ShapeCalc (Mangler et al. in review) provides a better fit to the shape data (Figure 58, Chapter 5.5). The CSDslice results are limited by a maximum ratio of 1:10 whilst ShapeCalc can accommodate much larger axis ratios. To further test these differences, CSD plots were produced via CSDCorrections for runs 1 and 4, which both had significantly better fits for the ShapeCalc output compared to the CSDSlice outputs used to determine their 3D shape. ShapeCalc gave a ratio of 1:17:20 for run 1, whilst CSDSlice gave 1:10:10. For run 4, ShapCalc gives 1:8:17 whilst CSDSlice gives 1:9:9

(see Figure 59, Chapter 5.5). There is a clear difference in the 3D shapes produced by these two sets of outputs.

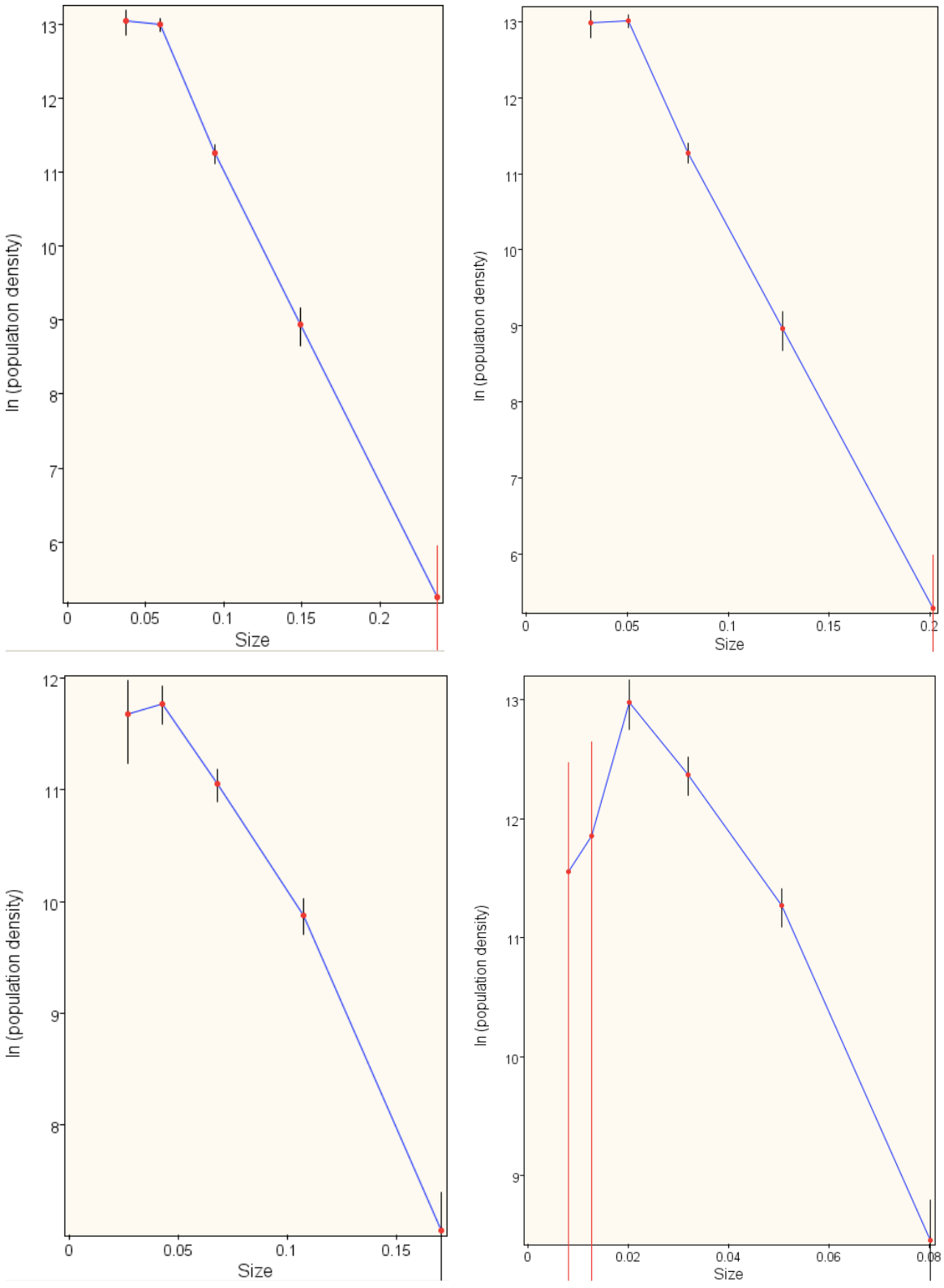

Figure 88, Two sets of CSD plots for samples 1 (upper) and 4 (lower), with the input shape changed for comparison. The left-hand plots show the CSD produced using the ShapeCalc axis ratio, and the right-hand side shows the same for the CSDSlice output.

Using equation 10, which is presented in Pupier et al., (2008), in conjunction with Cashman (1993) and Zieg and Marsh (2002), the CSDs were used to separately calculate an average growth rate, using the known timescale of the experiment, and a timescale using the measured bulk average growth rate (see chapter 5.6) for comparison to the values from the results of this study.

$$G = \frac{1}{m\Delta t} \quad (10)$$

Where G is the growth rate in m/s, m is the gradient of the plot, and t is the time in s.

Run	Calculating G (m/s)			Calculating t (s)		
	ShapeCalc	CSDSlice	Experimental	ShapeCalc	CSDSlice	Experimental
1	$1.6x10^{-8}$	$1.0x10^{-8}$	$1.7x10^{-8}$	2276	1477	2400
4	$2.5x10^{-8}$	$1.2x10^{-8}$	$2.1X10^{-8}$	1634	752	1320

Table 29. Calculating G and t from CSD plots of runs 1 and 4, with a comparison of results given when using the 3D shapes provided by ShapeCalc (Mangler, Personal communications) and CSDSlice (Morgan and Jerram, 2006).

Two similar approaches were taken for comparison – first, an average growth rate, G was calculated using equation 10 and the timescales measured during the experiments, then compared with the experimentally measured bulk mean growth rate. Then, the timescale, t, was calculated using equation 10 and the experimental bulk mean growth rates, and is compared with the timescale used in the experiments. For both the calculated G and t, using the 3D shape output from ShapeCalc gives results that are significantly closer to the experimental growth rates and timescale. Using CSDSlice alone could give results that are out by a factor of 2, which is a significant difference to the actual growth rates or timescales and can have an effect on further calculations using those results. The difference here is likely caused by the limited crystal axis ratio output of CSDSlice, compared to ShapeCalc. This is a further indicator of how important it is to get a good constraint on the 3D shape of crystals before making calculations such as these in CSD studies.

It can be seen that improvements can be made for future studies involving the 3D shapes of crystals. A clearer, more accurate understanding of plagioclase crystals and their organisation in 3D can help to better understand how crystals pack and flow within magma and lava during cooling.

The experiments carried out in this study have shown that growth rates of crystals are not constant over time, and generally decay as they grow as a result of impingement and possibly also a drop in effective undercooling as the melt evolves and the liquidus temperature drops, as equilibrium is approached (see chapter 2.2.1). This could affect how calculations are made in the future regarding crystallisation and cooling time. Current approaches to finding crystal growth also often use the full cooling time of the body of melt as the equivalent to the crystal growth time (e.g. Holness, 2014; Muncill and Lasaga, 1987). From direct observations of crystal growth, we have seen that crystals do not grow at a constant rate for the entirety of a cooling time, and can stop growing while still at high temperature, highlighting a need for better constraint on actual crystal cooling times as opposed to the cooling time of a body of melt or flow. A continuation of the work done here on the Avrami (1939, 1940, 1941) and Mollard et al., (2020) models for nucleation and crystal growth can help to better constrain this value for use in future interpretation of igneous rocks. It is also important to get constraints on growth patterns for the use of crystal zonation as a chronological tool. Importantly, the σ value, which is difficult to measure directly, is a necessary component of these models to better constrain in future work.

Furthermore, CSD studies often assume a constant crystal growth rate during the time that the melt was cooled (e.g. Marsh, 1998). We have seen that when the cooling time is close to the actual crystal growth time - as it is assumed to be for the experimental data presented here, since we were able to observe growth - mean and modal crystal growth rates are generally of

the same magnitude as an individual crystal growth rate during its main growth phase (after nucleation, before slowing/impingement), However, when the real 'growth time' of a crystal is not known, an assumption that crystal growth is constant during the cooling period could result in inaccurate growth rate and other calculations. An overestimate of the crystallisation time can lead to an underestimate of the growth rates, for example if Δt in equation 10 is larger than the realistic timescale, then the growth rate calculated from the CSD will be smaller than the actual average crystal growth rate. If this growth time is significantly overestimated it can lead to an incorrect understanding of how crystals grow within lava, which will affect how igneous rocks may be interpreted.

The experiments presented in this thesis have shown that it is possible to successfully use a high temperature heating stage to directly observe crystal growth from melt, from a natural basalt lava, at temperature conditions that are relevant to a cooling lava flow. The conditions of these experiments, using natural materials at natural cooling rates make these results highly relevant for natural studies of crystal growth in lava. This has implications on future studies of igneous petrology, where these 1 atm. experiments can be used to further investigate crystal growth. Further work on this could investigate the effects of much slower cooling rates on crystal textures and the relationship between observed and modelled crystal growth at longer timescales. Experiments at much faster cooling rates, reflective of cooling rates experienced closer to the top surface of a lava flow, could also be done to further investigate crystal growth. Additionally, a solution to the oxide growth obscuring of samples could be found by using materials with little or no Fe content, and results from this material can be compared to those obtained using natural materials.

The work in this thesis has focussed on measurements of crystals made in 2D. In reality, crystals growth is volumetric. It has been shown that the volumetric growth of a sphere is radial,

and this concept can be applied to growing tabular crystals (although each crystal face has a different growth rate), such as the plagioclase grown in these experiments. This radial growth often decreases as the crystals grow – similar to the effects seen in the individually tracked crystals in my experiments. Future work on crystal growth should consider this when examining crystal growth within lava flows or magma, as it is important to understand volumetric change and how to interpret crystal volume changes from 2D data.

8. Conclusion

The set of results taken from these experiments has shown that it is possible to successfully use a high temperature heating stage to directly observe crystal growth from a naturally formed basalt glass sample, at temperatures that are relevant to a cooling lava flow. Through comparison to both natural and experimental data on plagioclase morphology and growth rates in different conditions, we have validated the experimental results since growth rates and aspect ratios are within expected ranges for these conditions. The results also match reasonably well with the pre-experimental modelling carried out at the start of the project. These results are therefore directly applicable to natural situations and materials, indicating that the findings of this research are a valuable addition to the study and interpretation of igneous rocks and crystal growth.

The findings discussed in this thesis have led to three key conclusions:

Firstly, the morphological variations and growth rates of plagioclase crystals have been measured and reviewed with regard to the different cooling rates and temperatures experienced by the melt. There is a clear relationship between cooling rate and both the morphology and the growth rates of crystals, where a faster cooling rate leads to more skeletal – dendritic and irregular crystal shapes and the growth rate increases. These results fit well with previous work, and were generally as expected from earlier studies (e.g. Lofgren, 1974; Cashman, 1993). Furthermore, this work has led to a better understanding of how these differences vary within very low undercoolings, which in turn has helped to better interpret the patterns seen in the experimental results (Chapter 6.2).

Secondly, the direct observations made of crystal growth over time have allowed us to see that crystal growth is not constant over time, and decays to a stop for most crystals before the experimental cooling time is over. This has shown that crystallisation times and growth rates assumed in and calculated from CSD studies may need revision. The implications of this are that there is much to be done to better constrain growth rates at low undercoolings and the crystallisation times used to ascertain them in studies of crystals in igneous rocks. Further work could include a better refinement of modelling methods such as the Avrami method (Avrami 1939, 1941; Cashman, 1993), and the method described in Mollard et al. (2020). For this, a better understanding and constraint for the value of σ for growing plagioclase crystals is required, since this is an important unknown in these models that can have a large effect on the outputs.

We have also seen that 2D aspect ratio in these experiments increased over time as growth was primarily in the length direction throughout the experiments, which may be due to the melt having reached equilibrium, or due to the short time constraints on these experiments.

Finally, the variation in aspect ratios with temperature conditions and time has been measured and we have found that, within these results, there is no significant relationship between aspect ratio and cooling rate. However, these results have highlighted the complexity of the factors that affect crystal 2D aspect ratio, and by relation, its 3D morphology (Chapter 6.2.2). The relationship between aspect ratio and crystallisation time proposed in Holness (2014) was experimentally tested and it was found that the aspect ratio and temporal data from these experiments fit reasonably closely to the function proposed, within error. However, this relationship was weaker for larger crystals grown in the central parts of the sample, and the experimental dataset did not display a similar function when isolated. The function was also derived based on crystallisation times calculated from a 1-dimensional cooling model, which

may not be accurate. This relationship could be used to give a good initial idea of the crystallisation time based on crystal aspect ratio, but it unlikely to be an accurate or precise calculation without supplementary modelling or measurements.

The work presented in this thesis has explored and examined several of the many complex factors and features of crystal growth from basalt. Observing crystals directly as they grow has allowed observations of phenomena that have previously been only guessed at through interpretations of solidified rocks; and has highlighted how direct observations can indicate where previous studies of crystal growth have been lacking in the information needed to make accurate calculations. With some further refinement, a wealth of knowledge can be gained from future experiments in which crystals are directly observed to grow from a natural material, since no model or interpretation is as accurate or revealing as direct observation.

Bibliography

a. Applegarth, L.J., Tuffen, H., James, M.R., Cashman, K. and Pinkerton, H., 2013, December. Degassing-induced crystallization in basalts: direct experimental observations. In *AGU Fall Meeting Abstracts* (Vol. 2012, pp. V11C-2780).

b. Applegarth, L.J., Tuffen, H., James, M.R. and Pinkerton, H., 2013. Degassing-driven crystallisation in basalts. *Earth-Science Reviews*, *116*, pp.1-16.

Avrami, M., 1939. Kinetics of phase change. I General theory. *The Journal of chemical physics*, *7*(12), pp.1103-1112.

Avrami, M., 1940. Kinetics of phase change. II transformation-time relations for random distribution of nuclei. *The Journal of chemical physics*, *8*(2), pp.212-224.

Avrami, M., 1941. Granulation, phase change, and microstructure kinetics of phase change. III. *The Journal of chemical physics*, *9*(2), pp.177-184.

Baronnet, A., 1984. Growth kinetics of the silicates. A review of basic concepts. *Fort. Mineral.*, *62*, pp.187-232.

Biren, J., Harris, A., Tuffen, H., Chevrel, M.O., Gurioli, L., Vlastélic, I., Schiavi, F., Benbakkar, M., Fonquernie, C. and Calabro, L., 2020. Chemical, Textural and Thermal Analyses of Local Interactions Between Lava Flow and a Tree–Case Study From Pāhoa, Hawai'i. *Frontiers in Earth Science*, *8*, p.233.

Blundy, J. and Cashman, K., 2008. Petrologic reconstruction of magmatic system variables and processes. *Reviews in Mineralogy and Geochemistry*, *69*(1), pp.179-239.

Brandeis, G. and Jaupart, C., 1987. The kinetics of nucleation and crystal growth and scaling laws for magmatic crystallization. *Contributions to Mineralogy and Petrology*, *96*(1), pp.24-34.

Brugger, C.R. and Hammer, J.E., 2010. Crystal size distribution analysis of plagioclase in experimentally decompressed hydrous rhyodacite magma. *Earth and Planetary Science Letters*, *300*(3-4), pp.246-254.

Calvert, P.D. and Uhlmann, D.R., 1972. Surface nucleation growth theory for the large and small crystal cases and the significance of transient nucleation. *Journal of crystal growth*, *12*(4), pp.291-296.

Cashman, K. and Blundy, J., 2000. Degassing and crystallization of ascending andesite and dacite. *Philosophical Transactions of the Royal Society of London. Series A: Mathematical, Physical and Engineering Sciences*, *358*(1770), pp.1487-1513.

Cashman, K. and Blundy, J., 2013. Petrological cannibalism: the chemical and textural consequences of incremental magma body growth. *Contributions to Mineralogy and Petrology*, *166*(3), pp.703-729.

Cashman, K.V. and Marsh, B.D., 1988. Crystal size distribution (CSD) in rocks and the kinetics and dynamics of crystallization II: Makaopuhi lava lake. *Contributions to Mineralogy and Petrology*, *99*(3), pp.292-305.

Cashman, K.V., 1993. Relationship between plagioclase crystallization and cooling rate in basaltic melts. *Contributions to Mineralogy and Petrology*, *113*(1), pp.126-142.

Chevrel, M.O., Platz, T., Hauber, E., Baratoux, D., Lavallée, Y. and Dingwell, D.B., 2013. Lava flow rheology: a comparison of morphological and petrological methods. *Earth and Planetary Science Letters*, *384*, pp.109-120.

Cormier, V.F., Bergman, M.I. and Olson, P.L., 2022. Inner core dynamics. *Journal: Earth's Core*, pp.215-246.

First, E.C., Leonhardi, T.C. and Hammer, J.E., 2020. Effects of superheating magnitude on olivine growth. *Contributions to Mineralogy and Petrology*, *175*(2), pp.1-14.

Gaidies, F., 2017. Nucleation in geological materials. *EMU Notes in Mineralogy*, *16*, pp.347-371.

Ghiorso M.S., Gualda, G.A.R., (2015) An H2O-CO2 mixed fluid saturation model compatible with rhyolite-MELTS. Contributions to Mineralogy and Petrology, 2015

Gibb, F.G., 1974. Supercooling and the crystallization of plagioclase from a basaltic magma. *Mineralogical Magazine*, *39*(306), pp.641-653.

Giordano, D., Russell, J.K. and Dingwell, D.B., 2008. Viscosity of magmatic liquids: a model. *Earth and Planetary Science Letters*, *271*(1-4), pp.123-134.

Gottsmann, J., Harris, A.J. and Dingwell, D.B., 2004. Thermal history of Hawaiian pāhoehoe lava crusts at the glass transition: implications for flow rheology and emplacement. *Earth and Planetary Science Letters*, *228*(3-4), pp.343-353.

Gualda G.A.R., Ghiorso M.S., Lemons R.V., Carley T.L. (2012) Rhyolite-MELTS: A modified calibration of MELTS optimised for silica-rich, fluid-bearing magmatic systems. Journal of Petrology, 53, 875-890

Hammer, J.E., Cashman, K.V., Hoblitt, R.P. and Newman, S., 1999. Degassing and microlite crystallization during pre-climactic events of the 1991 eruption of Mt. Pinatubo, Philippines. *Bulletin of Volcanology*, *60*(5), pp.355-380.

Hanley, E.J., Dewitt, D.P. and Roy, R.F., 1978. The thermal diffusivity of eight well-characterized rocks for the temperature range 300–1000 K. *Engineering Geology*, *12*, pp.31-47.

Higgins, M.D., 1994. Numerical modeling of crystal shapes in thin sections: estimation of crystal habit and true size. *American Mineralogist*, *79*(1-2), pp.113-119.

Higgins, M.D., 1996. Magma dynamics beneath Kameni volcano, Thera, Greece, as revealed by crystal size and shape measurements. *Journal of Volcanology and Geothermal Research*, *70*(1-2), pp.37-48.

Higgins, M.D., 2000. Measurement of crystal size distributions. *American Mineralogist*, *85*(9), pp.1105-1116.

Hill, R. and Roeder, P., 1974. The crystallization of spinel from basaltic liquid as a function of oxygen fugacity. *The Journal of Geology*, *82*(6), pp.709-729.

Hillig, W.B. and Turnbull, D., 1956. Theory of crystal growth in undercooled pure liquids. *The Journal of Chemical Physics*, *24*(4), pp.914-914.

Holness, M.B., 2014. The effect of crystallization time on plagioclase grain shape in dolerites. *Contributions to Mineralogy and Petrology*, *168*(5), p.1076.

Holness, M.B., Humphreys, M.C., Sides, R., Helz, R.T. and Tegner, C., 2012. Toward an understanding of disequilibrium dihedral angles in mafic rocks. *Journal of Geophysical Research: Solid Earth*, *117*(B6).

Hon, K., Kauahikaua, J.P. and Mackay, K., 1993. *Inflation and cooling data from pahoehoe sheet flows on Kilauea Volcano*. US Department of the Interior, US Geological Survey.

Hon, K.E.N., Kauahikaua, J.I.M., Denlinger, R. and Mackay, K., 1994. Emplacement and inflation of pahoehoe sheet flows: Observations and measurements of active lava flows on Kilauea Volcano, Hawaii. *Geological Society of America Bulletin*, *106*(3), pp.351-370.

Keith, H.D. and Padden Jr, F.J., 1963. A phenomenological theory of spherulitic crystallization. *Journal of Applied Physics*, *34*(8), pp.2409-2421.

Keszthelyi, L. and Denlinger, R., 1996. The initial cooling of pahoehoe flow lobes. *Bulletin of Volcanology*, *58*(1), pp.5-18.

Keszthelyi, L., 1995. Measurements of the cooling at the base of pahoehoe flows. *Geophysical Research Letters*, *22*(16), pp.2195-2198.

Kilburn, C.R.J., 1993, March. Lava crusts and flow dynamics. In *Lunar and Planetary Science Conference* (Vol. 24).

Kirkpatrick, R.J., 1975. Crystal growth from the melt: a review. *American Mineralogist: Journal of Earth and Planetary Materials*, *60*(9-10), pp.798-814.

Kirkpatrick, R.J., 1977. Nucleation and growth of plagioclase, Makaopuhi and Alae lava lakes, Kilauea Volcano, Hawaii. *Geological Society of America Bulletin*, *88*(1), pp.78-84.

Kirkpatrick, R.J., Klein, L., Uhlmann, D.R. and Hays, J.F., 1979. Rates and processes of crystal growth in the system anorthite-albite. *Journal of Geophysical Research: Solid Earth*, *84*(B7), pp.3671-3676.

Kirkpatrick, R.J., 2018. Kinetics of crystallization of igneous rocks. In *Kinetics of geochemical processes* (pp. 321-398). De Gruyter.

Kohn, S.C., 2000. The dissolution mechanisms of water in silicate melts; a synthesis of recent data. *Mineralogical Magazine*, *64*(3), pp.389-408.

Langmuir, C.H., 1989. Geochemical consequences of in situ crystallization. *Nature*, *340*(6230), pp.199-205.

Liu, L., Li, Z., Jiao, Y. and Li, S., 2017. Maximally dense random packings of cubes and cuboids via a novel inverse packing method. *Soft Matter*, *13*(4), pp.748-757.

Lofgren, G., 1974. An experimental study of plagioclase crystal morphology; isothermal crystallization. *American journal of Science*, *274*(3), pp.243-273.

Loomis, T.P., 1981. An investigation of disequilibrium growth processes of plagioclase in the system anorthite-albite-water by methods of numerical simulation. *Contributions to Mineralogy and Petrology*, *76*(2), pp.196-205.

Loomis, T.P., 1982. Numerical simulations of crystallization processes of plagioclase in complex melts: the origin of major and oscillatory zoning in plagioclase. *Contributions to Mineralogy and Petrology*, *81*(3), pp.219-229.

Ludington, S., 1979. Thermodynamics of melting of anorthite deduced from phase equilibrium studies. *American Mineralogist*, *64*(1-2), pp.77-85.

Lyman, A.W., Kerr, R.C. and Griffiths, R.W., 2005. Effects of internal rheology and surface cooling on the emplacement of lava flows. *Journal of Geophysical Research: Solid Earth*, *110*(B8).

Mader, H.M., Llewellin, E.W. and Mueller, S.P., 2013. The rheology of two-phase magmas: A review and analysis. *Journal of Volcanology and Geothermal Research*, *257*, pp.135-158.

Maillard, M., Motte, L., Ngo, A.T. and Pileni, M.P., 2000. Rings and hexagons made of nanocrystals: A Marangoni effect. *The Journal of Physical Chemistry B*, *104*(50), pp.11871-11877.

Mangler, M.F., Humphreys, M.C.S., Wadsworth, F.B., Iveson, A.A. & Higgins, M.D. Variation of plagioclase shape with size in intermediate magmas: a window into incipient plagioclase crystallisation. Contributions to Mineralogy & Petrology (in review)

Marsh, B.D., 1981. On the crystallinity, probability of occurrence, and rheology of lava and magma. *Contributions to Mineralogy and Petrology*, *78*(1), pp.85-98.

Marsh, B.D., 1988. Crystal size distribution (CSD) in rocks and the kinetics and dynamics of crystallization. *Contributions to Mineralogy and Petrology*, *99*(3), pp.277-291.

Marsh, B.D., 1998. On the interpretation of crystal size distributions in magmatic systems. *Journal of Petrology*, *39*(4), pp.553-599.

Martin, V.M., Holness, M.B. and Pyle, D.M., 2006. Textural analysis of magmatic enclaves from the Kameni Islands, Santorini, Greece. *Journal of Volcanology and Geothermal Research*, *154*(1-2), pp.89-102.

Masotta, M., Pontesilli, A., Mollo, S., Armienti, P., Ubide, T., Nazzari, M. and Scarlato, P., 2020. The role of undercooling during clinopyroxene growth in trachybasaltic

magmas: Insights on magma decompression and cooling at Mt. Etna volcano. *Geochimica et Cosmochimica Acta*, *268*, pp.258-276.

Masotta, M., Pontesilli, A., Mollo, S., Armienti, P., Ubide, T., Nazzari, M. and Scarlato, P., 2020. The role of undercooling during clinopyroxene growth in trachybasaltic magmas: Insights on magma decompression and cooling at Mt. Etna volcano. *Geochimica et Cosmochimica Acta*, *268*, pp.258-276.

Mollard, E., Martel, C. and Bourdier, J.L., 2012. Decompression-induced crystallization in hydrated silica-rich melts: empirical models of experimental plagioclase nucleation and growth kinetics. *Journal of Petrology*, *53*(8), pp.1743-1766.

Mollard, E., Martel, C., Le Trong, E. and Rogerie, G., 2020. Theoretical models of decompression-induced plagioclase nucleation and growth in hydrated silica-rich melts. *Frontiers in Earth Science*, *8*, p.203.

Morgan, D.J. and Jerram, D.A., 2006. On estimating crystal shape for crystal size distribution analysis. *Journal of Volcanology and Geothermal Research*, *154*(1-2), pp.1-7.

Mucek, A.E., Garcia, M.O. and Swanson, D., 2012, December. Geochemistry of Glasses and Eruption Conditions from KEANAKAKOI Tephra at Kilauea Volcano, HAWAII. In *AGU Fall Meeting Abstracts* (Vol. 2012, pp. V13D-2883).

Mueller, S., Llewellin, E.W. and Mader, H.M., 2011. The effect of particle shape on suspension viscosity and implications for magmatic flows. *Geophysical Research Letters*, *38*(13).

Muncill, G.E. and Lasaga, A.C., 1987. Crystal-growth kinetics of plagioclase in igneous systems; one-atmosphere experiments and application of a simplified growth model. *American Mineralogist*, *72*(3-4), pp.299-311.

Muncill, G.E. and Lasaga, A.C., 1988. Crystal-growth kinetics of plagioclase in igneous systems; isothermal H 2 O-saturated experiments and extension of a growth model to complex silicate melts. *American Mineralogist*, *73*(9-10), pp.982-992.

Oze, C. and Winter, J.D., 2005. The occurrence, vesiculation, and solidification of dense blue glassy pahoehoe. *Journal of Volcanology and Geothermal Research*, *142*(3-4), pp.285-301.

Peterson, D.W. and Tilling, R.I., 1980. Transition of basaltic lava from pahoehoe to aa, Kilauea Volcano, Hawaii: field observations and key factors. *Journal of Volcanology and Geothermal Research*, *7*(3-4), pp.271-293.

Pinkerton, H. and Stevenson, R.J., 1992. Methods of determining the rheological properties of magmas at sub-liquidus temperatures. *Journal of Volcanology and Geothermal Research*, *53*(1-4), pp.47-66.

Pontesilli, A., Masotta, M., Nazzari, M., Mollo, S., Armienti, P., Scarlato, P. and Brenna, M., 2019. Crystallization kinetics of clinopyroxene and titanomagnetite growing from a trachybasaltic melt: New insights from isothermal time-series experiments. *Chemical Geology*, *510*, pp.113-129.

Pupier, E., Duchene, S. and Toplis, M.J., 2008. Experimental quantification of plagioclase crystal size distribution during cooling of a basaltic liquid. *Contributions to Mineralogy and Petrology*, *155*(5), pp.555-570.

Randolph A.D and Larson MA.,.1971. Theory of particulate processes. *Academic Press*, New York, pp. 251

Salisbury, M.J., Bohrson, W.A., Clynne, M.A., Ramos, F.C. and Hoskin, P., 2008. Multiple plagioclase crystal populations identified by crystal size distribution and in situ chemical data: Implications for timescales of magma chamber processes associated with the 1915 eruption of Lassen Peak, CA. *Journal of Petrology*, *49*(10), pp.1755-1780.

Schiavi, F., Walte, N. and Keppler, H., 2009. First in situ observation of crystallization processes in a basaltic-andesitic melt with the moissanite cell. *Geology*, *37*(11), pp.963-966.

Schiavi, F., Walte, N., Konschak, A. and Keppler, H., 2010. A moissanite cell apparatus for optical in situ observation of crystallizing melts at high temperature. *American Mineralogist*, *95*(7), pp.1069-1079.

Schneider, C. A., Rasband, W. S., & Eliceiri, K. W. (2012). NIH Image to ImageJ: 25 years of image analysis. *Nature Methods*, *9*(7), 671–675. doi:10.1038/nmeth.2089

Self, S., Keszthelyi, L.P. and Thordarson, T., 1998. The importance of pahoehoe: Annual Review of Earth and Planetary Science, no. 26.

Shea, T. and Hammer, J.E., 2013. Kinetics of cooling-and decompression-induced crystallization in hydrous mafic-intermediate magmas. *Journal of Volcanology and Geothermal research*, *260*, pp.127-145.

Sunagawa, I., 2007. *Crystals: growth, morphology, & perfection*. Cambridge University Press.

Swanson, D.A., 1973. Pahoehoe flows from the 1969–1971 Mauna Ulu eruption, Kilauea volcano, Hawaii. *Geological Society of America Bulletin*, *84*(2), pp.615-626.

Turnbull, D. and Cohen, M.H., 1960. Crystallization kinetics and glass formation. *Modern aspects of the vitreous state*, *1*, pp.38-62.

Uhlmann, D.R., O

norato, P.I.K. and Scherer, G.W., 1979. A simplified model for glass formation. In *Lunar and Planetary Science Conference Proceedings* (Vol. 10, pp. 375-381).

Watanabe, K. and Kitamura, M., 1992. Growth mechanisms of plagioclase in a basaltic melt. *Mineralogical Journal*, *16*(4), pp.201-214.

White, W.M., 2020. *Geochemistry*. John Wiley & Sons.

Wilmoth, R.A. and Walker, G.P., 1993. P-type and S-type pahoehoe: a study of vesicle distribution patterns in Hawaiian lava flows. *Journal of Volcanology and Geothermal Research*, *55*(1-2), pp.129-142.

Zanotto, E.D. and Galhardi, A., 1988. Experimental test of the general theory of transformation kinetics: Homogeneous nucleation in a Na2O· 2CaO· 3SiO2 glass. *Journal of non-crystalline solids*, *104*(1), pp.73-80.

Zanotto, E.D. and Leite, M.L.G., 1996. The nucleation mechanism of lithium dissilicate glass revisited. *Journal of non-crystalline solids*, *202*(1-2), pp.145-152.

Zanotto, E.D., 1996. The applicability of the general theory of phase transformations to glass crystallization. *Thermochimica acta*, *280*, pp.73-82.

Zieg, M.J. and Marsh, B.D., 2002. Crystal size distributions and scaling laws in the quantification of igneous textures. *Journal of Petrology*, *43*(1), pp.85-101.